



Calhoun: The NPS Institutional Archive

Theses and Dissertations

Thesis Collection

1987

Characterization of the corrosion behavior of high damping alloys in seawater.

Escue, William David.

<http://hdl.handle.net/10945/22663>



Calhoun is a project of the Dudley Knox Library at NPS, furthering the precepts and goals of open government and government transparency. All information contained herein has been approved for release by the NPS Public Affairs Officer.

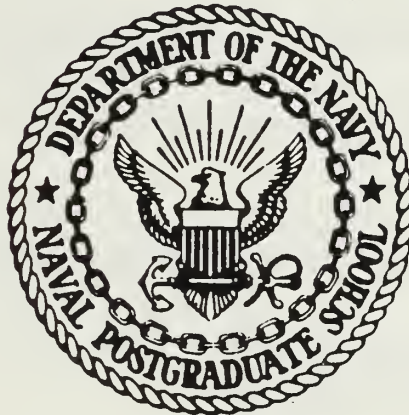
Dudley Knox Library / Naval Postgraduate School
411 Dyer Road / 1 University Circle
Monterey, California USA 93943

<http://www.nps.edu/library>

DUDLEY KNOX LIBRARY
SANDY ELEMENTARY SCHOOL
MONTLEIGH, CALIFORNIA 95013-5002

NAVAL POSTGRADUATE SCHOOL

Monterey, California



THESIS

CHARACTERIZATION OF THE CORROSION BEHAVIOR
OF HIGH DAMPING ALLOYS IN SEAWATER

by

William David Escue

June 1987

Thesis Advisor:

J. Perkins

Approved for public release; distribution is unlimited

T234172

UNCLASSIFIED

SECURITY CLASSIFICATION OF THIS PAGE

REPORT DOCUMENTATION PAGE

REPORT SECURITY CLASSIFICATION UNCLASSIFIED		1b RESTRICTIVE MARKINGS	
SECURITY CLASSIFICATION AUTHORITY		3 DISTRIBUTION/AVAILABILITY OF REPORT Approved for public release; distribution is unlimited	
DECLASSIFICATION / DOWNGRADING SCHEDULE			
PERFORMING ORGANIZATION REPORT NUMBER(S)		5 MONITORING ORGANIZATION REPORT NUMBER(S)	
NAME OF PERFORMING ORGANIZATION	6b OFFICE SYMBOL (If applicable)	7a NAME OF MONITORING ORGANIZATION	
Naval Postgraduate School	Code 69	Naval Postgraduate School	
ADDRESS (City, State, and ZIP Code)		7b ADDRESS (City, State, and ZIP Code)	
Monterey, California 93943-5000		Monterey, California 93943-5000	
NAME OF FUNDING / SPONSORING ORGANIZATION	8b OFFICE SYMBOL (If applicable)	9 PROCUREMENT INSTRUMENT IDENTIFICATION NUMBER	
ADDRESS (City, State, and ZIP Code)		10 SOURCE OF FUNDING NUMBERS	
		PROGRAM ELEMENT NO	PROJECT NO
		TASK NO	WORK UNIT ACCESSION NO

TITLE (Include Security Classification)
CHARACTERIZATION OF THE CORROSION BEHAVIOR OF HIGH DAMPING ALLOYS IN SEAWATER

PERSONAL AUTHOR(S)
Escue, William D.

1 TYPE OF REPORT Master's Thesis	13b TIME COVERED FROM _____ TO _____	14 DATE OF REPORT (Year, Month, Day) 1987, June	15 PAGE COUNT 127
-------------------------------------	---	--	----------------------

SUPPLEMENTARY NOTATION

COSATI CODES			18 SUBJECT TERMS (Continue on reverse if necessary and identify by block number) Corrosion; Damping; Sea Water
FIELD	GROUP	SUB-GROUP	

ABSTRACT (Continue on reverse if necessary and identify by block number)

Corrosion rates and the nature of corrosive attack were investigated for several high damping alloys, including alloys based on the Cu-Mn, Fe-Cr-Al, Fe-Cr-Mo, Ti-Ni, and Cu-Zn-Al systems. Rates and modes of attack were determined for exposure of samples in synthetic and natural seawater. The results of potentiodynamic polarization and polarization resistance measurements made in the laboratory were compared with the results of actual sea exposures at the LaQue Center for Corrosion Technology, Wrightsville Beach, North Carolina. These results were used to make tentative recommendations for in-service application of high damping alloys used singly or in combination with common aluminum alloys and steels in a marine environment. Overlays of independently determined potentiodynamic polarization plots for selected pairs of alloys were used to project theoretical corrosion rates in galvanic couples. A Galvanic Series for high damping and conventional

DISTRIBUTION/AVAILABILITY OF ABSTRACT <input checked="" type="checkbox"/> UNCLASSIFIED/UNLIMITED <input type="checkbox"/> SAME AS RPT <input type="checkbox"/> DTIC USERS		21 ABSTRACT SECURITY CLASSIFICATION Unclassified	
NAME OF RESPONSIBLE INDIVIDUAL Prof. Jeff Perkins		22b TELEPHONE (Include Area Code) (408) 646-2216	22c OFFICE SYMBOL Code 69Ps

FORM 1473, 84 MAR

83 APR edition may be used until exhausted

All other editions are obsolete

SECURITY CLASSIFICATION OF THIS PAGE

UNCLASSIFIED

#19 - ABSTRACT - (CONTINUED)

alloys in quiescent synthetic seawater was developed. Results from laboratory and actual sea exposures showed that the Fe-Cr-Al and Fe-Cr-Mo high damping alloys experienced severe localized corrosion and pitting, the Ti-Ni alloy demonstrated a very slight corrosion rate, and the Cu-Mn-Al-based and Cu-Zn-Al-based alloys were characterized by low to moderate corrosion rates.

Approved for public release; distribution is unlimited

Characterization of the Corrosion Behavior
of High Damping Alloys in Seawater

by

William David Escue
Lieutenant Commander, United States Navy
B.S.I.E., Georgia Institute of Technology, 1977

Submitted in partial fulfillment of the
requirements for the degree of

MASTER OF SCIENCE IN MECHANICAL ENGINEERING

from the

NAVAL POSTGRADUATE SCHOOL
June 1987

Thesis
E666
C-1

ABSTRACT

Corrosion rates and the nature of corrosive attack were investigated for several high damping alloys, including alloys based on the Cu-Mn, Fe-Cr-Al, Fe-Cr-Mo, Ti-Ni, and Cu-Zn-Al systems. Rates and modes of attack were determined for exposure of samples in synthetic and natural seawater. The results of potentiodynamic polarization and polarization resistance measurements made in the laboratory were compared with the results of actual sea exposures at the LaQue Center for Corrosion Technology, Wrightsville Beach, North Carolina. These results were used to make tentative recommendations for in-service application of high damping alloys used singly or in combination with common aluminum alloys and steels in a marine environment. Overlays of independently determined potentiodynamic polarization plots for selected pairs of alloys were used to project theoretical corrosion rates in galvanic couples. A Galvanic Series for high damping and conventional alloys in quiescent synthetic seawater was developed. Results from laboratory and actual sea exposures showed that the Fe-Cr-Al and Fe-Cr-Mo high damping alloys experienced severe localized corrosion and pitting, the Ti-Ni alloy demonstrated a very

slight corrosion rate, and the Cu-Mn-Al-based and Cu-Zn-Al-based alloys were characterized by low to moderate corrosion rates.

TABLE OF CONTENTS

I.	INTRODUCTION -----	19
II.	BASIC CORROSION THEORY--A REVIEW OF EXPERIMENTAL TECHNIQUES -----	21
	A. POTENTIODYNAMIC POLARIZATION -----	21
	B. POLARIZATION RESISTANCE -----	26
	C. OTHER METHODS FOR ASSESSING CORROSION DAMAGE-----	29
	D. DETERMINATION OF TAFEL CONSTANTS -----	30
III.	EXPERIMENTAL EQUIPMENT AND PROCEDURES -----	35
	A. EXPERIMENTAL EQUIPMENT -----	35
	B. EXPERIMENTAL PROCEDURES FOR SYNTHETIC SEAWATER EXPOSURES -----	38
	C. SAMPLE PREPARATION -----	41
	D. TESTED MATERIALS -----	43
	E. EXPERIMENTAL PARAMETERS -----	45
	F. SCANNING ELECTRON MICROSCOPY -----	46
	G. EXPERIMENTAL PROCEDURES FOR NATURAL SEAWATER EXPOSURES -----	46
IV.	RESULTS AND DISCUSSION -----	50
	A. TITANIUM--NICKEL -----	50
	B. 1020 CARBON STEEL -----	55
	C. 7075 ALUMINUM -----	62
	D. 304 STAINLESS STEEL -----	67
	E. FE-CR-MO -----	72
	F. FE-CR-AL -----	79

G.	CU-MN-AL-FE-NI -----	85
H.	CU-MN-AL -----	90
I.	CU-ZN-AL -----	96
J.	630 SERIES BRONZE -----	101
K.	COMPARISON OF AVERAGE CORROSION RATE RESULTS FOR LABORATORY AND SEAWATER EXPOSURES -----	106
L.	GALVANIC SERIES OF SELECTED HIGH DAMPING AND BASELINE ALLOYS IN QUIESCENT SYNTHETIC SEAWATER -----	108
M.	SELECTED GALVANIC COUPLES -----	109
V.	RECOMMENDATIONS -----	121
APPENDIX A:	PREPARATION OF SYNTHETIC SEAWATER -----	122
APPENDIX B:	STANDARD OPERATING PROCEDURES FOR THE MODEL 351 CORROSION MEASUREMENT SYSTEM -----	124
LIST OF REFERENCES	-----	125
INITIAL DISTRIBUTION LIST	-----	126

LIST OF TABLES

I.	THEORETICAL CORROSION RATES EXPECTED FOR THE ANODIC MEMBER OF SELECTED GALVANIC COUPLES -----	110
----	--	-----

LIST OF FIGURES

1. Potentiodynamic Polarization Plot of 304 Stainless Steel in Dilute H ₂ SO ₄ -----	23
2. Theoretical Potentiodynamic Polarization Plot Showing Anodic and Cathodic Tafel Regions -----	23
3. Potentiodynamic Polarization Plot of Fe-Cr-Mo in Synthetic Seawater. No Distinct Tafel Regions Are Apparent -----	25
4. Polarization Resistance Plot for Ti-Ni in Synthetic Seawater -----	28
5. Tangent Method for Determination of the "Knee" of a Cathodic Polarization Curve for Fe-Cr-Al -----	32
6. Locations of I _p and I _g for the Potentiodynamic Polarization Plot of Fe-Cr-Al -----	32
7. Standard Specimen Holder Assembly -----	36
8. Assembled PAR Model K47 Corrosion Cell -----	37
9. Potentiodynamic Polarization Experimental Input Display for the Model 351 Corrosion Measurement System -----	39
10. The PAR Model 351 Corrosion Measurement System Showing the Model K47 Corrosion Cell, Model 272/273 Potentiostat, and the Model 1000 Processor from Left to Right -----	40
11. Electrical Connections for the Model 351 Corrosion Measurement System -----	42
12. Exploded View of the Model K105 Flat Specimen Holder -----	44
13. The LaQue Center for Corrosion Technology, Wrightsville Beach, N.C. -----	48
14. Low Velocity Seawater Exposure Trough at the LaQue Center for Corrosion Technology, Wrightsville Beach, N.C. -----	49

15. Potentiodynamic Polarization Plot for Ti-Ni in Synthetic Seawater -----	51
16. Polarization Resistance Plot for Ti-Ni in Synthetic Seawater -----	51
17. As-Machined Surface of Ti-Ni Prior to Corrosion Experimentation, 1000X -----	52
18. Corrosion Product on Ti-Ni after Polarization Experimentation, 2000X -----	52
19. Ti-Ni Samples after Removal from Exposure Troughs at the LaQue Center Following an Exposure Period of 67 Days -----	53
20. Corroded Surface of Ti-Ni after a 67 Day Exposure at the LaQue Center, 25X -----	54
21. Corroded Surface of Ti-Ni after a 67 Day Exposure at the LaQue Center, 1000X -----	54
22. Potentiodynamic Polarization Plot for 1020 C Steel in Synthetic Seawater -----	56
23. Polarization Resistance Plot for 1020 C Steel in Synthetic Seawater -----	56
24. As-Machined Surface of 1020 C Steel Prior to Corrosion Experimentation, 1000X -----	57
25. Corrosion Product on 1020 C Steel after Polarization Experimentation, 2160X -----	57
26. Corrosion Product on 1020 C Steel after Polarization Experimentation, 123X -----	58
27. 1020 C Steel Samples after Removal from Exposure Troughs at the LaQue Center Following an Exposure Period of 67 Days -----	59
28. Corroded Surface of 1020 C Steel after a 67 Day Exposure at the LaQue Center, 26X -----	60
29. Corroded Surface of 1020 C Steel after a 67 Day Exposure at the LaQue Center, 1000X -----	60
30. Potentiodynamic Polarization Plot for 7075 Aluminum in Synthetic Seawater -----	63
31. Polarization Resistance Plot for 7075 Aluminum in Synthetic Seawater -----	63

32. As-Machined Surface of 7075 Aluminum Prior to Corrosion Experimentation, 1000X -----	64
33. Corrosion Product on 7075 Aluminum after Polarization Experimentation, 1000X -----	64
34. 7075 Aluminum Samples after Removal from Exposure Troughs at the LaQue Center Following an Exposure Period of 67 Days -----	65
35. Corroded Surface of 7075 Aluminum after a 67 Day Exposure at the LaQue Center, 25X -----	66
36. Corroded Surface of 7075 Aluminum after a 67 Day Exposure at the LaQue Center, 1000X -----	66
37. Potentiodynamic Polarization Plot for 304 Stainless Steel in Synthetic Seawater -----	68
38. Polarization Resistance Plot for 304 Stainless Steel in Synthetic Seawater -----	68
39. As-Machined Surface of 304 Stainless Steel Prior to Corrosion Experimentation, 1000X -----	69
40. Corrosion Product on 304 Stainless Steel after Polarization Experimentation, 2000X -----	69
41. 304 Stainless Steel Samples after Removal from Exposure Troughs at the LaQue Center Following an Exposure Period of 67 Days -----	70
42. Corroded Surface of 304 Stainless Steel after a 67 Day Exposure at the LaQue Center, 26X -----	71
43. Corroded Surface of 304 Stainless Steel after a 67 Day Exposure at the LaQue Center, 1000X -----	71
44. Potentiodynamic Polarization Plot for Fe-Cr-Mo in Synthetic Seawater -----	74
45. Polarization Resistance Plot for Fe-Cr-Mo in Synthetic Seawater -----	74
46. As-Machined Surface of Fe-Cr-Mo Prior to Corrosion Experimentation, 1000X -----	75
47. Corrosion Product on Fe-Cr-Mo after Polarization Experimentation, 31X -----	75
48. Corrosion Product on Fe-Cr-Mo after Polarization Experimentation, 2000X -----	76

49. Fe-Cr-Mo Samples after Removal from Exposure Troughs at the LaQue Center Following an Exposure Period of 67 Days -----	77
50. Corroded Surface of Fe-Cr-Mo after a 67 Day Exposure at the LaQue Center, 25X -----	78
51. Corroded Surface of Fe-Cr-Mo after a 67 Day Exposure at the LaQue Center, 1000X -----	78
52. Potentiodynamic Polarization Plot for Fe-Cr-Al in Synthetic Seawater -----	80
53. Polarization Resistance Plot for Fe-Cr-Al in Synthetic Seawater -----	80
54. As-Machined Surface of Fe-Cr-Al Prior to Corrosion Experimentation, 1000X -----	81
55. Corrosion Product on Fe-Cr-Al after Polarization Experimentation, 31X -----	81
56. Corrosion Product on Fe-Cr-Al after Polarization Experimentation, 2000X -----	82
57. Fe-Cr-Al Samples after Removal from Exposure Troughs at the LaQue Center Following an Exposure Period of 67 Days -----	83
58. Corroded Surface of Fe-Cr-Al after a 67 Day Exposure at the LaQue Center, 25X -----	84
59. Corroded Surface of Fe-Cr-Al after a 67 Day Exposure at the LaQue Center, 1000X -----	84
60. Potentiodynamic Polarization Plot for Cu-Mn-Al-Fe-Ni in Synthetic Seawater -----	86
61. Polarization Resistance Plot for Cu-Mn-Al-Fe-Ni in Synthetic Seawater -----	86
62. As-Machined Surface of Cu-Mn-Al-Fe-Ni Prior to Corrosion Experimentation, 1000X -----	87
63. Corrosion Product on Cu-Mn-Al-Fe-Ni after Polarization Experimentation, 2000X -----	87
64. Cu-Mn-Al-Fe-Ni Samples after Removal from Exposure Troughs at the LaQue Center Following an Exposure Period of 67 Days -----	88

65. Corroded Surface of Cu-Mn-Al-Fe-Ni after a 67 Day Exposure at the LaQue Center, 25X -----	89
66. Corroded Surface of Cu-Mn-Al-Fe-Ni after a 67 Day Exposure at the LaQue Center, 1000X-----	89
67. Potentiodynamic Polarization Plot for Cu-Mn-Al in Synthetic Seawater -----	91
68. Polarization Resistance Plot for Cu-Mn-Al in Synthetic Seawater -----	91
69. As-Machined Surface of Cu-Mn-Al Prior to Corrosion Experimentation, 1000X -----	93
70. Corrosion Product on Cu-Mn-Al after Polarization Experimentation, 1900X -----	93
71. Cu-Mn-Al Samples after Removal from Exposure Troughs at the LaQue Center Following an Exposure Period of 67 Days -----	94
72. Corroded Surface of Cu-Mn-Al after a 67 Day Exposure at the LaQue Center, 25X -----	95
73. Corroded Surface of Cu-Mn-Al after a 67 Day Exposure at the LaQue Center, 1000X -----	95
74. Potentiodynamic Polarization Plot for Cu-Zn-Al in synthetic Seawater -----	97
75. Polarization Resistance Plot for Cu-Zn-Al in Synthetic Seawater -----	97
76. As-Machined Surface of Cu-Zn-Al Prior to Corrosion Experimentation, 1000X -----	98
77. Corrosion Product on Cu-Zn-Al after Polarization Experimentation, 2160X -----	98
78. Cu-Zn-Al Samples after Removal from Exposure Troughs at the LaQue Center Following an Exposure Period of 67 Days (a) Side View (b) Top View -----	99
79. Corroded Surface of Cu-Zn-Al after a 67 Day Exposure at the LaQue Center, 12X -----	100
80. Corroded Surface of Cu-Zn-Al after a 67 Day Exposure at the LaQue Center, 1000X -----	100

81. Potentiodynamic Polarization Plot for 630 Series Bronze in Synthetic Seawater -----	102
82. Polarization Resistance Plot for 630 Series Bronze in Synthetic Seawater -----	102
83. As-Machined Surface of 630 Series Bronze Prior to Corrosion Experimentation, 1000X -----	103
84. Corrosion Product on 630 Series Bronze after Polarization Experimentation, 2000X -----	103
85. 630 Series Bronze Samples after Removal from Exposure Troughs at the LaQue Center Following an Exposure Period of 67 Days -----	104
86. Corroded Surface of 630 Series Bronze after a 67 Day Exposure at the LaQue Center, 25X -----	105
87. Corroded Surface of 630 Series Bronze after a 67 Day Exposure at the LaQue Center, 560X -----	105
88. Overlay of Potentiodynamic Plots for 7075 Aluminum (A) and Cu-Zn-Al (B) -----	112
89. Overlay of Potentiodynamic Plots for 7075 Aluminum (A) and Ti-Ni (B) -----	112
90. Overlay of Potentiodynamic Plots for 7075 Aluminum (A) and Cu-Mn-Al (B) -----	113
91. Overlay of Potentiodynamic Plots for 7075 Aluminum (A) and Cu-Mn-Al-Fe-Ni -----	113
92. Overlay of Potentiodynamic Plots for 7075 Aluminum (A) and Fe-Cr-Mo (B) -----	114
93. Overlay of Potentiodynamic Plots for 7075 Aluminum (A) and Fe-Cr-Al (B) -----	114
94. Overlay of Potentiodynamic Plots for 1020 C Steel (A) and Cu-Zn-Al (B) -----	115
95. Overlay of Potentiodynamic Plots for 1020 C Steel (A) and Ti-Ni (B) -----	115
96. Overlay of Potentiodynamic Plots for 1020 C Steel (A) and Cu-Mn-Al (B) -----	116
97. Overlay of Potentiodynamic Plots for 1020 C Steel (A) and Cu-Mn-Al-Fe-Ni (B) -----	116

98.	Overlay of Potentiodynamic Plots for 1020 C Steel (A) and Fe-Cr-Mo (B) -----	117
99.	Overlay of Potentiodynamic Plots for 1020 C Steel (A) and Fe-Cr-Al (B) -----	117
100.	Overlay of Potentiodynamic Plots for 304 Stainless Steel (A) and Cu-Zn-Al (B) -----	118
101.	Overlay of Potentiodynamic Plots for 304 Stainless Steel (A) and Ti-Ni (B) -----	118
102.	Overlay of Potentiodynamic Plots for 304 Stainless Steel (A) and Cu-Mn-Al (B) -----	119
103.	Overlay of Potentiodynamic Plots for 304 Stainless Steel (A) and Cu-Mn-Al-Fe-Ni (B) -----	119
104.	Overlay of Potentiodynamic Plots for 304 Stainless Steel (A) and Fe-Cr-Mo (B) -----	120
105.	Overlay of Potentiodynamic Plots for 304 Stainless Steel (A) and Fe-Cr-Al (B) -----	120

LIST OF SYMBOLS AND ABBREVIATIONS

cm	centimeter
cm ²	centimeter squared
C.R.	corrosion rate
E _{corr}	corrosion potential of a single metal
E _{couple}	corrosion potential of a metal couple
E.W.	equivalent weight
g	gram
i _{corr}	corrosion current density of a single metal
i _{couple}	corrosion current density of a metal couple
kg	kilogram
L(1)	liter
LPM	Linear Polarization Method
m	meter
ml	milliliter
mm	millimeter
mpy	mils per year
mV	millivolt
μA	microampere
PAR	Princeton Applied Research
PDP	potentiodynamic polarization
Rmpy	corrosion rate in mils per year
SCE	saturated calomel electrode
SEM	scanning electron microscope/microscopy

V volt
X magnification

ACKNOWLEDGMENT

The author wishes to express his gratitude for the advice and guidance received from Professor Jeff Perkins. Professor Perkin's assistance was greatly appreciated and his enthusiasm and encouragement stimulated the author's interest in the subject area.

Laboratory technician Tom Kellogg deserves special thanks. His positive, "can do" attitude coupled with his strong background in Chemistry and Corrosion Engineering saved the author numerous hours of "tail chasing." The tremendous amount of time he spent in both hands-on training and experimental analysis was most appreciated.

I. INTRODUCTION

Structures and equipment for use in marine environments are commonly subjected to conditions which lead to corrosive attack. The prediction of a materials' performance in a corrosive environment can be made using standard laboratory techniques. However, these techniques may not fully predict the corrosion rates and characteristics of a given alloy or galvanic couple when exposed in the actual marine environment. The prediction of a system's performance can be enhanced by correlating laboratory results with those results achieved in a natural environment. The purpose of the present research is to present the results and experimental procedures used to obtain corrosion rates and corrosion characteristics of high damping alloys in a marine environment.

To achieve this goal, a number of experimental techniques were applied, resulting in the determination of representative corrosion rates and anticipated modes of corrosive attack. Linear Polarization and Potentiodynamic Polarization techniques (performed on the Princeton Applied Research Model 351 Corrosion Measurement System) were utilized to determine the corrosion rates of the tested alloys. These techniques were also used for the determination of a galvanic series for both high damping and

common baseline alloys in quiescent, synthetic seawater. These results allowed the prediction of the corrosion characteristics of selected galvanic couples in a marine environment.

Results from concurrent sea exposure of the alloys (conducted at The LaQue Center for Corrosion Technology, Wrightsville Beach, N.C.) were compared with the laboratory results to better predict the corrosion behavior of the high damping alloys for in-service marine applications.

Scanning electron microscopy was used following laboratory experimentation and sea exposures to analyze the modes of surface attack experienced by each alloy.

Prior to discussing experimental procedures and results, a brief summary of applicable corrosion/electrochemical theory and analytical expressions will prove useful.

II. BASIC CORROSION THEORY--A REVIEW OF EXPERIMENTAL TECHNIQUES

Many corrosion processes can be explained in terms of electrochemical reactions. Measurements of current and potential in a controlled environment can provide information regarding corrosion rates, film formation and pitting tendencies.

A. POTENTIODYNAMIC POLARIZATION

Potentiodynamic Polarization is an electrochemical technique in which the potential of the metal sample of interest is continuously scanned in the anodic direction. Conventionally, potential values achieved during the scan are plotted against the current density (current per surface area). Generally, as the potential is increased, current increases, due to anodic dissolution. However, in some cases, as the specimen is scanned anodically, an oxide coating forms on the surface of the specimen, thus reducing the current and corrosion rate. Potentiodynamic polarization measurements are commonly used to calculate corrosion rates of an alloy in a given solution.

When a metal specimen is immersed in a corrosive medium, the sample assumes a potential relative to a reference electrode. This relative potential is termed the corrosion potential of the specimen, E_{corr} . At E_{corr} , simultaneous

anodic and cathodic reactions are occurring at the surface. The specimen is at an equilibrium condition and no net external current is passed. The rate of oxidation and reduction are equal at E_{corr} .

An example of a potentiodynamic polarization experiment is shown in Figure 1. Region A exhibits typical active corrosion of the sample. At B, a continued increase in applied potential results in a decreasing current density, corresponding to a decreased rate of corrosion. This occurs at the onset of film formation. Region C is characterized by decreasing current density with further increase in potential, as the passivating film develops and more fully covers the surface of the sample. Region D shows minimal changes in current density as the potential is increased; this is designated as the Passivation Region. A further increase in potential may result in an increase in current density and a breakdown of the passivating film, so that Region E is designated as the Transpassive Region and is usually characterized by pitting of the sample.

Corrosion rates can be obtained by extrapolation of the linear (Tafel) regions (near E_{corr}) for either or both the anodic and cathodic branches of the Potentiodynamic Polarization plot. For example, Figure 2 shows extrapolations of the Tafel regions intercepting at E_{corr} . The value of current density at the intercept is defined as i_{corr} , which is directly related to corrosion rate

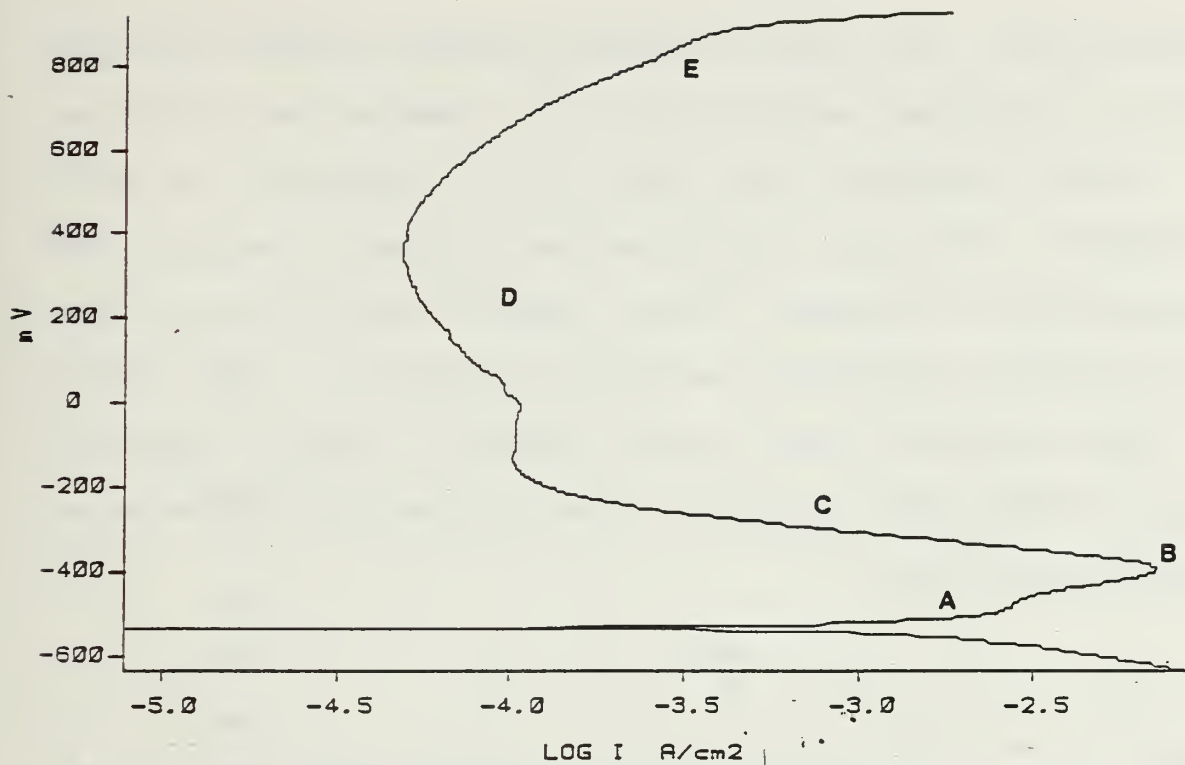


Figure 1. Potentiodynamic Polarization Plot of 304 Stainless Steel in Dilute H_2SO_4

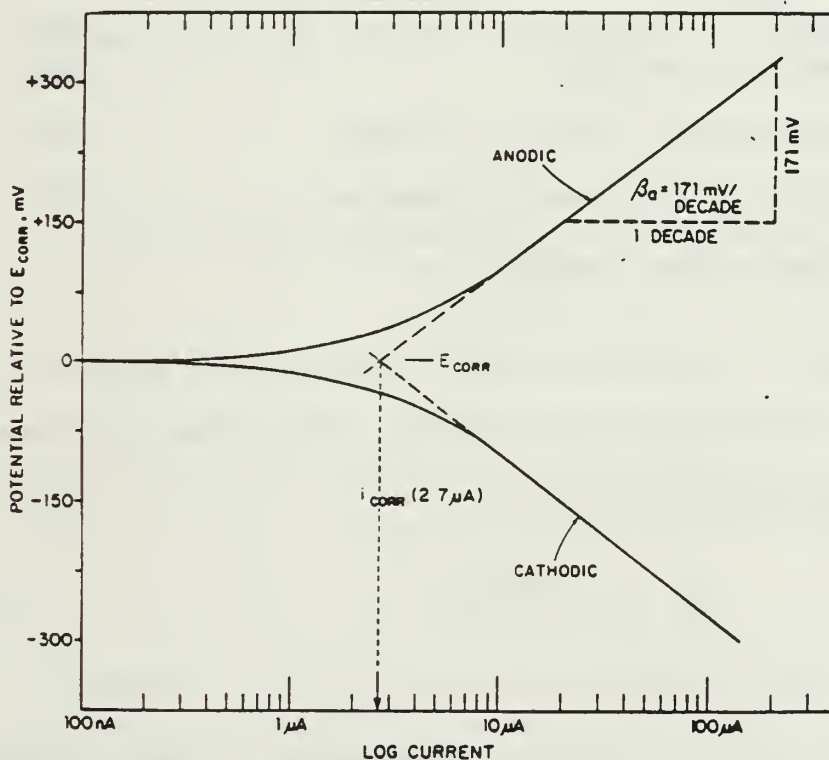


Figure 2. Theoretical Potentiodynamic Polarization Plot Showing Anodic and Cathodic Tafel Regions

calculations. The Tafel regions generally start ± 50 mV from E_{corr} and may extend from 1 to 3 decades in length on the current density axis [Ref. 1]. However, in many experiments, the Tafel region can be extremely limited, and determination of slopes in the Tafel region (β_a, β_c) can prove extremely difficult as shown in Figure 3. This point will be addressed later in more detail. Once a value of i_{corr} is determined, corrosion rate calculations can be made using Faraday's Law:

$$Q = \frac{nFW}{M} \quad (1)$$

where:

Q = Coulombs

n = number of electrons involved in the electrochemical reaction

F = the Faraday, 96,487 coulombs

W = weight of the atomic species

M = the molecular weight.

Since M/n is defined as the Equivalent Weight of the sample, and Q is equal to current multiplied by time, the following relationship holds:

$$\frac{W}{t} = \frac{i(E.W.)}{F} \quad (2)$$

where W/t is the corrosion rate in grams per second.

Corrosion rate is typically expressed in milliinches per year (mils per year). Dividing Equation (2) by the sample

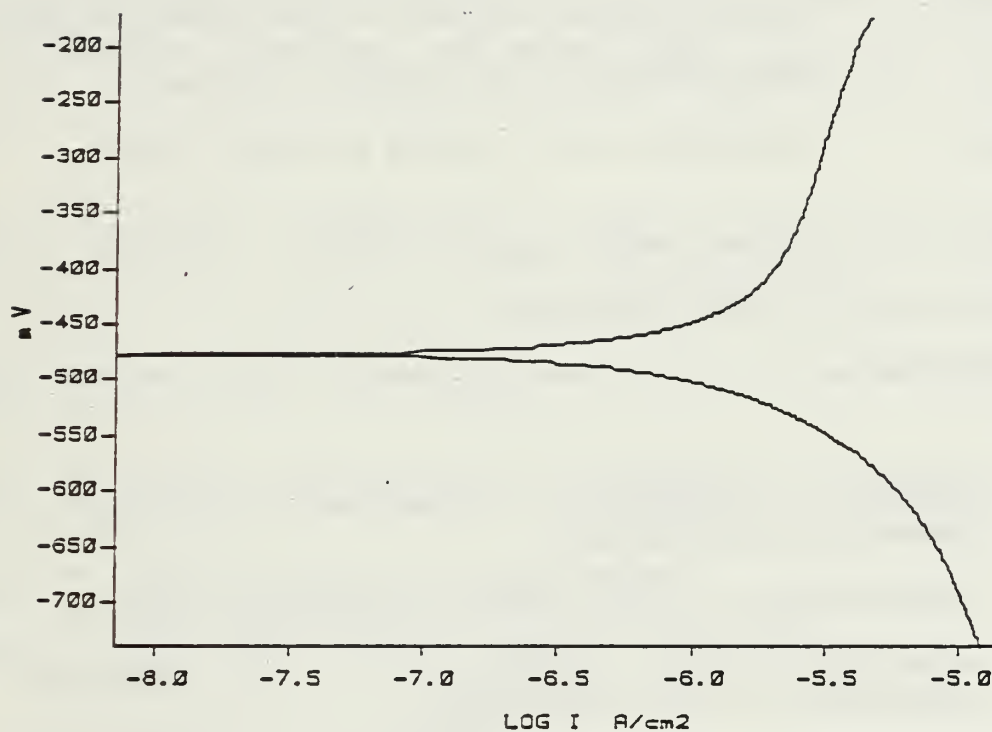


Figure 3. Potentiodynamic Polarization Plot of Fe-Cr-Mo in Synthetic Seawater. No distinct Tafel Regions Are Apparent

area and density and using appropriate conversions results in the following:

$$\text{C.R.} = \frac{0.1287 i_{\text{corr}} (\text{E.W.})}{d} \quad (3)$$

where:

- i_{corr} = the corrosion current density. (A/cm²)
- E.W. = the Equivalent Weight of the material (g)
- d = the density of the sample in g/cm³
- C.R. = corrosion rate in mils per year (mpy).

Equation (3) can be used to calculate the corrosion rate of a given alloy in mils per year.

Advantages of the Potentiodynamic Polarization method are:

- 1) Readily apparent observation of film formation/passivation;
- 2) Determination of the rate of corrosion; and
- 3) Relatively short period of time required for completion of the experiment.

Disadvantages of this method are:

- 1) Tafel slopes may be very difficult to determine;
- 2) Scanning the sample deteriorates the sample's surface, preventing further experimentation using the same sample.

B. POLARIZATION RESISTANCE

The Polarization Resistance Technique is a rapid method for determining the corrosion rate of a material. The experimental apparatus is identical to that used for the

Potentiodynamic Polarization technique. However, potential scanning of the sample is only performed over a small range (± 25 mV) near E_{corr} . In this region of scanning, the applied current density is nearly a linear function of the applied potential. Current density and potential are both plotted on a linear scale as shown in Figure 4.

The value for i_{corr} is directly related to the slope of the Polarization plot by the Stern-Geary equation [Refs. 1,2,3]:

$$\text{P.R.} = \frac{\Delta E}{\Delta i} = \frac{\beta_a \beta_c}{2.303 i_{\text{corr}} (\beta_a + \beta_c)} \quad (4)$$

where:

P.R. = slope of the Polarization Resistance plot in ohms

β_a, β_b = Tafel slopes in Volts/Decade

i_{corr} = corrosion current density in A/cm².

Rearranging Equation (4) yields:

$$i_{\text{corr}} = \frac{\beta_a \beta_c}{2.303 (\beta_a + \beta_c)} \times \frac{\Delta i}{\Delta E} \quad (5)$$

Solving for i_{corr} using Equation (5) allows for direct substitution into Equation (3) for determination of corrosion rate. The major advantage of this method is the speed of determination of a sample's corrosion rate. The

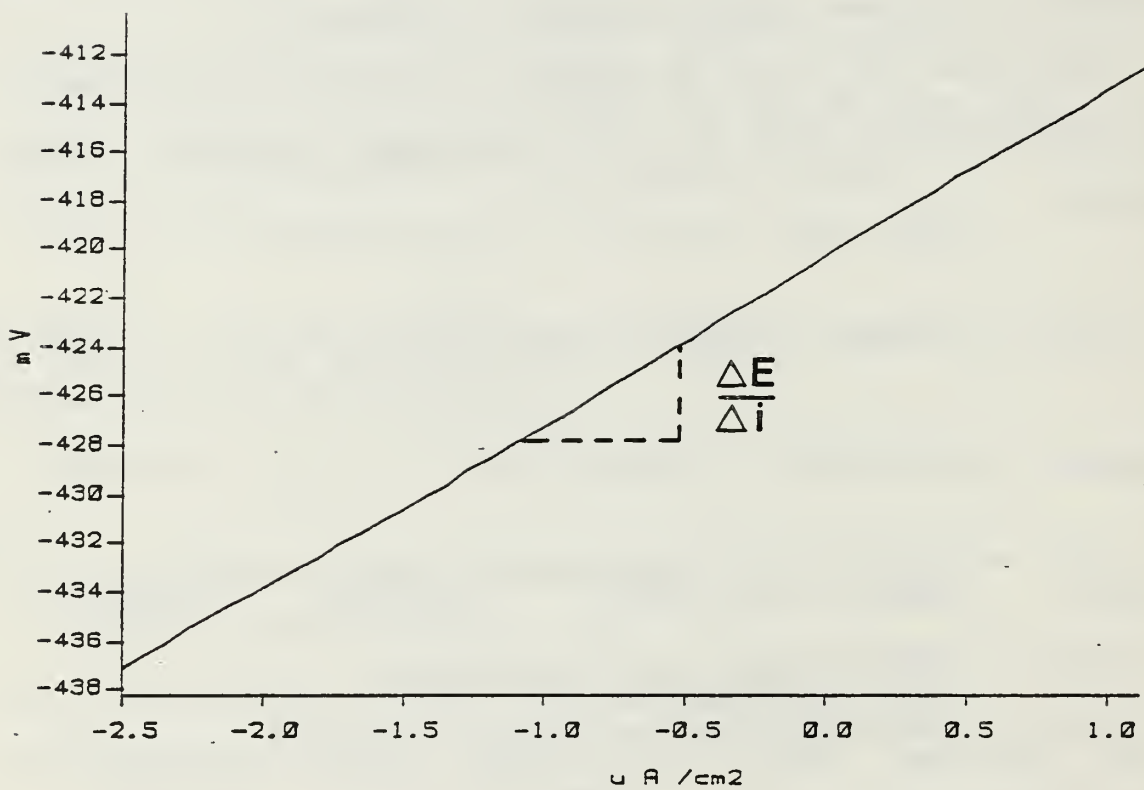


Figure 4. Polarization Resistance Plot for Ti-Ni in Synthetic Seawater

Polarization Resistance experiment can be performed in a matter of only several minutes.

C. OTHER METHODS FOR ASSESSING CORROSION DAMAGE

Direct weight loss measured on a corroded specimen is another commonly used technique for determining corrosion rates. This method is extremely simple in nature and can be performed with relatively unsophisticated equipment. Concurrent corrosion experiments performed at the LaQue Center as part of the present research program utilized direct weight loss measurements for determination of corrosion rates.

In order to achieve the most consistent results, weight loss measurements should be made on samples of equal size and geometry and exposed to the corrosive medium for an identical period of time. The corrosion rate can be determined from the following relation:

$$\text{C.R.} = \frac{\text{Weight Loss}}{\text{Area} \times \text{Time} \times \text{Density}} \quad (6)$$

Even though this method is quickly and easily accomplished, there are several disadvantages, including:

- 1) Corrosion rate determinations assume that all weight loss has occurred from general corrosion; localized corrosion modes are not considered.
- 2) This method assumes that the material has not been internally attacked by other forms of corrosion such as dealloying, intergranular corrosion, etc.
- 3) Extreme care is required when the corrosion product is removed from the sample. Some of the base metal may

accidentally be removed, leading to inaccurate results.

Pit depth determination is another valuable method for assessing corrosion damage. The LaQue Center also performed this analysis when applicable. If the pitting is broad and shallow, pit depth calipers can be used. Deeper, narrower pits require depth determination by means of cross-sectional microscopy.

D. DETERMINATION OF TAFEL CONSTANTS

As discussed previously, determination of the Tafel slopes can prove to be extremely difficult in some cases, depending on the material and corrosive medium. The extent of Tafel regions is directly influenced by several factors, including concentration polarization, multiple reduction processes, active to passive transitions, and the IR drop related to the conductivity of the electrolyte. Tafel slopes are generally found to be in the range of 0.06 to 0.12 V/Decade [Refs. 1,2,3]. Pourbaix has shown that using a value of 0.1 V/Decade for both Tafel constants yields a corrosion rate within a factor of 2.2 [Ref. 4]. Since both polarization techniques used in this study require determination of Tafel slopes for the calculation of corrosion rates, several methods for approximating the Tafel constants are described here and will later be used in the calculations on the experimental data.

1. Method 1: The "Knee" Method with PDP Curves

As exemplified by Figure 3, sometimes no distinct Tafel regions are apparent in PDP curves. In such a case, the "Knee" method can be employed. This method requires determination of the "knee" point for either/or both the anodic and cathodic curves. The "knee" is located as shown in Figure 5 for a cathodic branch of a Potentiodynamic Polarization plot. When angles A and B are equal, the point of tangency locates the "knee" and the slope of the tangent becomes the Tafel constant. A similar technique is used if the anodic branch demonstrates no readily apparent Tafel region. The intercepts of these tangents locate i_{corr} , and corrosion rate can be determined using Equation (3). This method has been used successfully by B.E. Wilde [Ref. 5].

2. Method 2: Tafel "Knee" Slopes and LPM Data

Using the results from Method 1, the Tafel constants so-determined are used in conjunction with Polarization Resistance results to determine the corrosion current density using Equation (5). Solution for i_{corr} then allows determination of the corrosion rate using Equation (3).

3. Method 3: Pearson Method with PDP Curves

This method, also known as "The Polarization Break Method" was developed by J.M. Pearson and allows for a direct determination of i_{corr} [Ref. 1:pp. 586-587]. As shown in Figure 6, points A and B are determined using the same technique for finding the "knee" as discussed

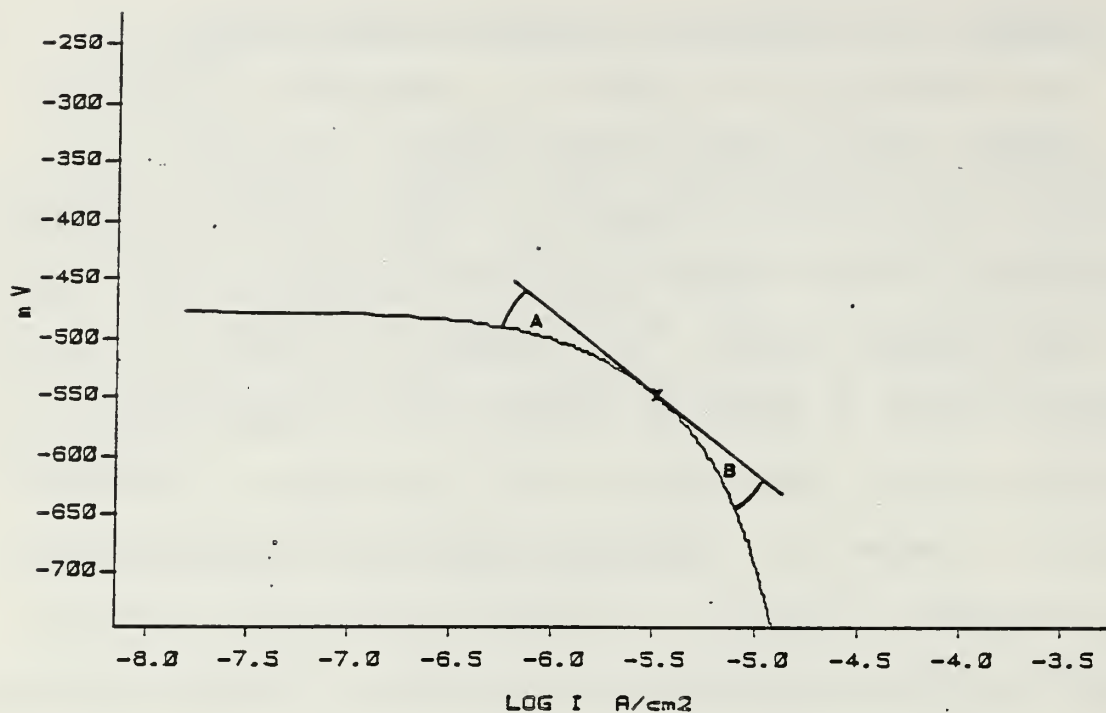


Figure 5. Tangent Method for Determination of the "knee" of a Cathodic Polarization Curve for Fe-Cr-Al

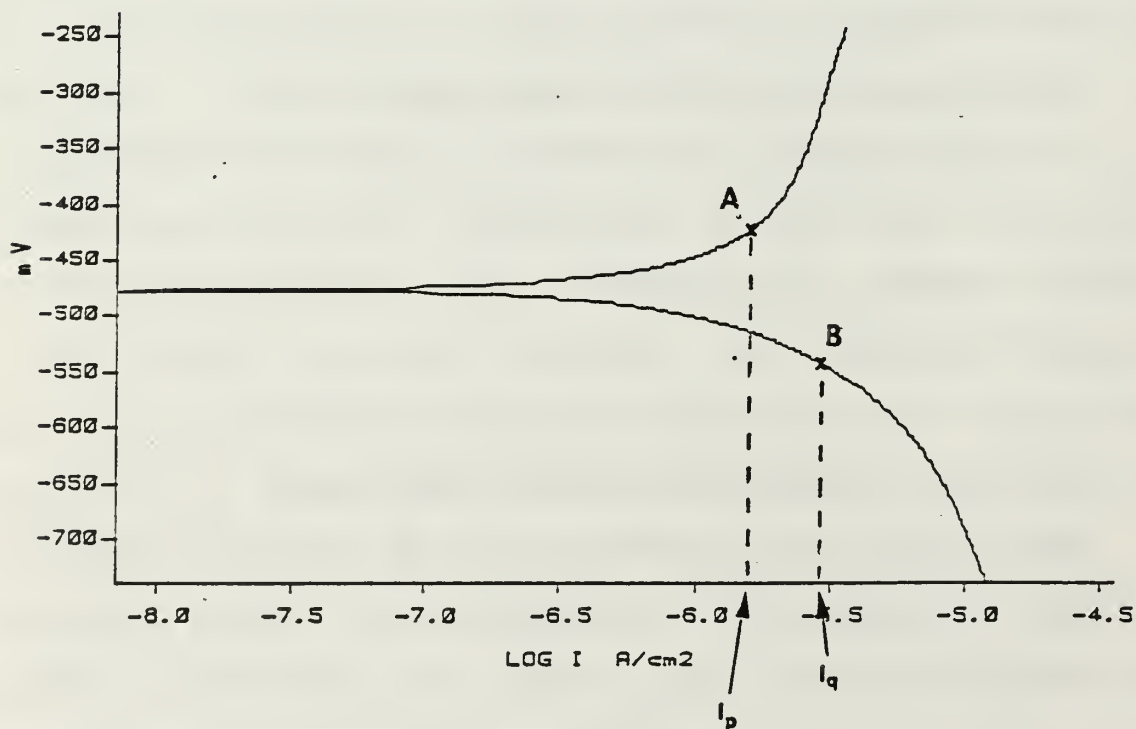


Figure 6. Locations of I_p and I_q for the Potentiodynamic Polarization Plot of Fe-Cr-Al

previously. Once values for I_p and I_q have been determined, i_{corr} is defined as follows:

$$i_{corr} = \frac{I_p I_q}{I_p + I_q} \quad (7)$$

This value for i_{corr} can be used directly in Equation (3) for corrosion rate determination.

4. Method 4: Assumed Tafel Slopes of 0.1 V/Decade with PDP Curves

In this method, values of 0.1 V/Decade simply are selected for both Tafel constants. Then, a "best fit" using these Tafel slopes is made for both the anodic and cathodic portions of a Potentiodynamic Polarization plot. The intercept of these tangents yields i_{corr} and Equation (3) is solved to obtain the corrosion rate.

5. Method 5: Assumed Tafel Slopes of 0.1 V/Decade with LPM Data

This method is identical to Method 2 but uses the arbitrarily selected Tafel constants of 0.1 V/Decade (mentioned above in Method 4) in the Stern-Geary equation.

As will be shown in this research, corrosion rates measured in actual seawater exposures are generally within a factor of 2 to 3 of the corrosion rates calculated using these 5 methods. This is considered acceptable, but points out that a factor of safety is of paramount importance when using laboratory results to project service performance. Corrosion rate determinations in a natural service

environment, when used in conjunction with laboratory results, will allow for a better determination of in-service corrosion characteristics.

III. EXPERIMENTAL EQUIPMENT AND PROCEDURES

A. EXPERIMENTAL EQUIPMENT

The key to producing consistent polarization diagrams in this work proved to be the use of a rigidly standardized experimental procedure. With the exception of the potential ranges scanned versus E_{corr} , the methodology for performing the polarization experiments was identical for each alloy tested.

1. The Corrosion Cell

The basic PAR Model K47 corrosion cell consists of a multi-port flask, 2 Carbon counter electrodes, a working electrode with a threaded tip for sample attachment (Figure 7), and the Saturated Calomel Reference Electrode. Figure 8 shows an actual view of the corrosion cell.

2. The Potentiostat

The PAR Model 272/273 Potentiostat was used throughout this research. The potentiostat processes the potentials and currents experienced by the operating corrosion cell to allow for data collection and graphical plotting.

3. The Processor

The PAR Model 1000 Processor/computer receives input of the potential and current values from the Potentiostat, processes the data, and generates the polarization plots.

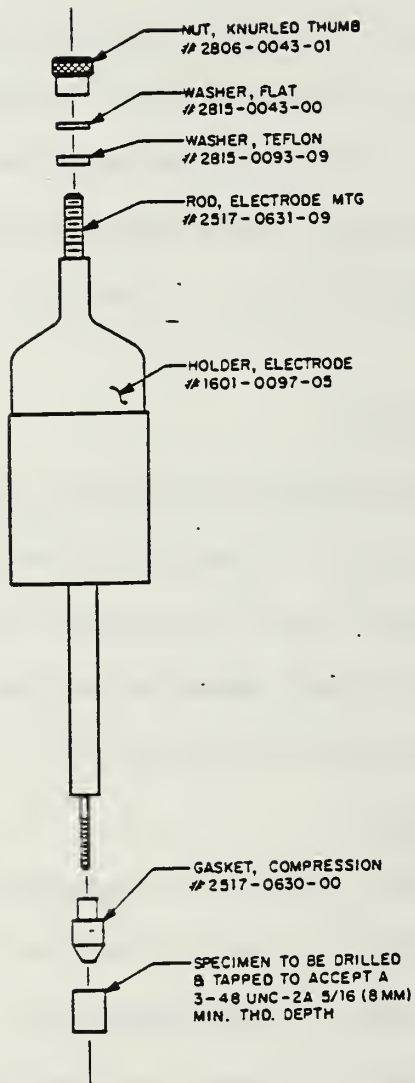


Figure 7. Standard Specimen Holder Assembly

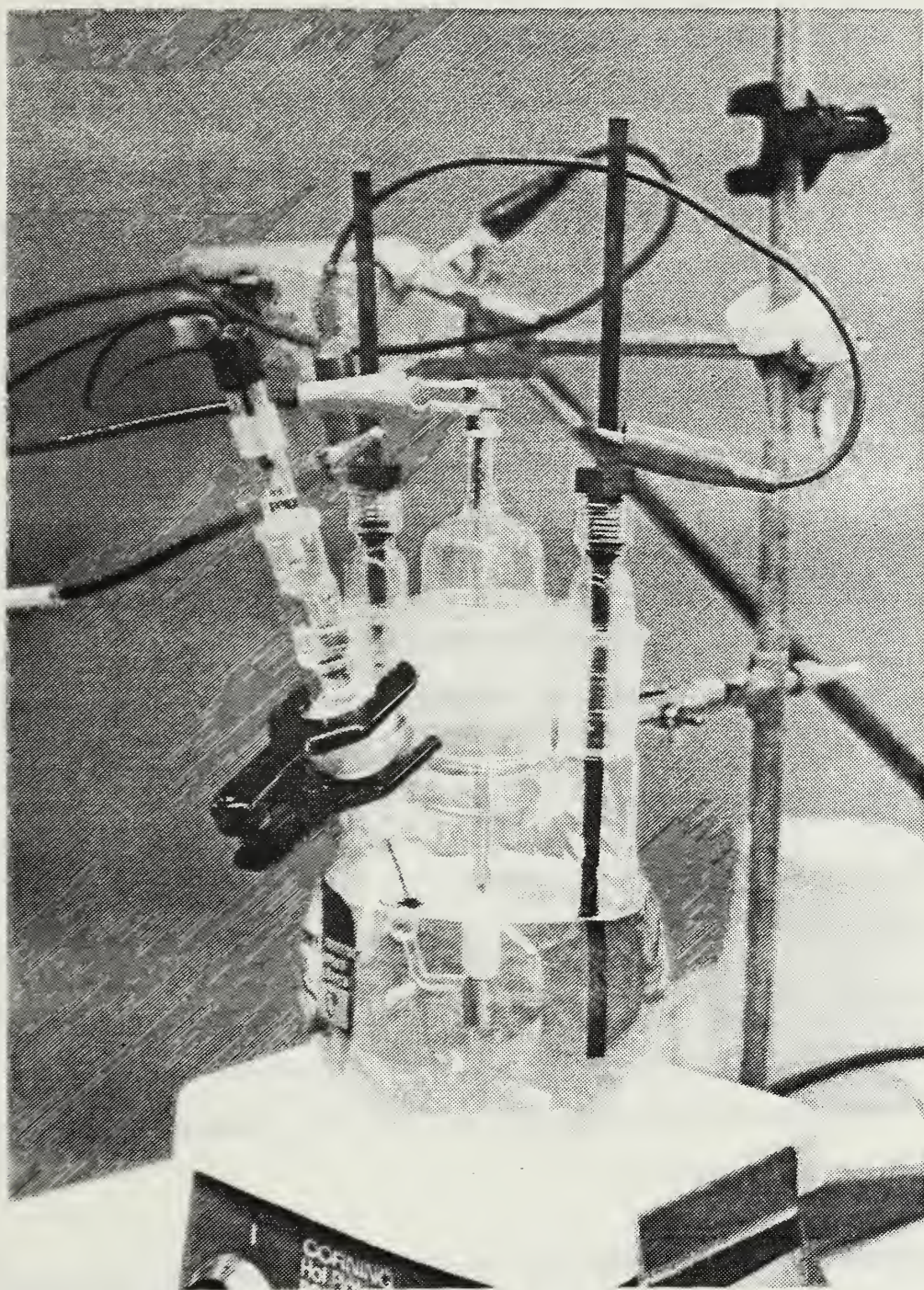


Figure 8. Assembled PAR Model K47 Corrosion Cell

The Processor permits an input of customized test procedures which may be saved for later recall.

4. The Model 351 Corrosion Measurement System

The PAR Model 351 System couples the Model K47 Corrosion Cell, Model 272/273 Potentiostat, the Model 1000 Processor, and a plotter to achieve a versatile, easy-to-use system suited to perform a variety of corrosion experiments. The touch screen format allows rapid modification of experimental procedures. Figure 9 shows a typical format for a Potentiodynamic Polarization experiment. Figure 10 shows the basic system installation for performance of corrosion experiments.

The Model 351 Corrosion Measurement System can also process the data from a Potentiodynamic Polarization experiment to obtain Tafel constants. However, the programming used to perform this calculation is relatively simplistic and was considered to be inadequate for determination of the true Tafel regions in this work. As a result, hand calculations were utilized by the author to determine Tafel constants, i_{corr} , and corrosion rates.

Basic operating procedures for the Model 351 system are listed in Appendix B.

B. EXPERIMENTAL PROCEDURES FOR SYNTHETIC SEAWATER EXPOSURES

Rigid and consistent experimental procedures are necessary for reproducibility of a given experiment. ASTM

POTENTIODYNAMIC CREATE/EDIT: PAGE 1		SAMPLE ID: UNNAMED COMMENT: EG&G PARC MODEL 351	
SELECTED TECHNIQUE POTENTIODYNAMIC			
<input type="text"/> INITIAL E -250 mV- E_c	<input type="text"/> INITIAL DELAY 3600 SEC	<input type="text"/> SCAN RATE 0.166 mV/SEC	
<input type="text"/> FINAL E 1.2 V			
	<input type="text"/> SMOOTH 7 POINTS	<input type="text"/> IR COMPENSATION DISABLED	
<input type="button" value="MAIN
MENU"/>	<input type="button" value="NEXT
PAGE"/>	<input type="button" value="SELECT NEW
TECHNIQUE"/>	

Figure 9. Potentiodynamic Polarization Experimental Input Display for the Model 351 Corrosion Measurement System

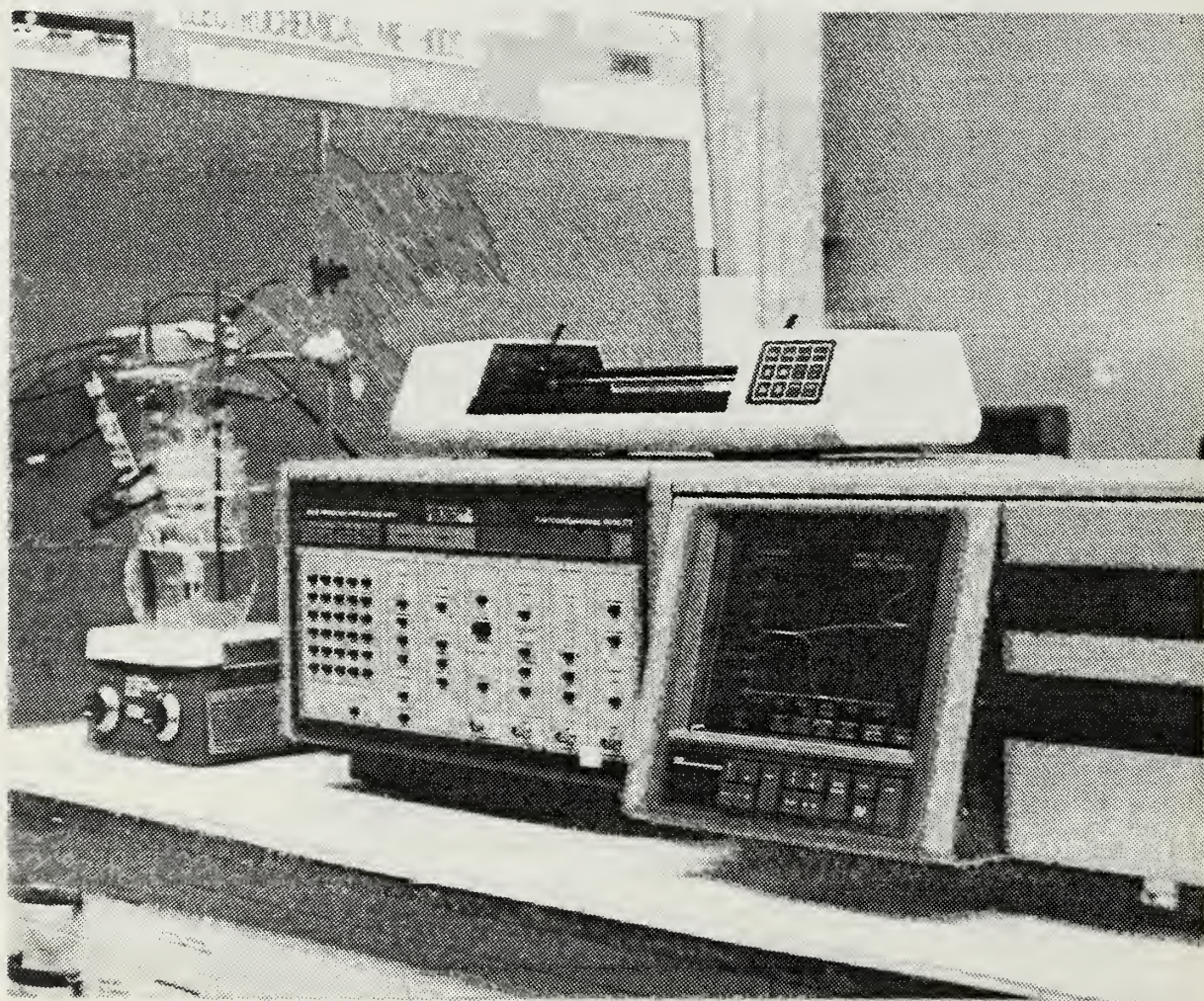


Figure 10. The PAR Model 351 Corrosion Measurement System Showing the Model K47 Corrosion Cell, Model 272/273 Potentiostat, and the Model 1000 Processor from Left to Right

Standard G 5-72 ("Standard Reference Method for Making Potentiostatic and Potentiodynamic Anodic Polarization Measurements") was utilized as the procedure for conducting polarization experiments. Prior to performing an experiment, all components of the corrosion cell were thoroughly cleaned and dried. A magnetic stirrer was placed in the corrosion cell after filling with approximately 800 mL of synthetic seawater. The carbon counter electrodes, working electrode with the attached sample, and the Saturated Calomel reference electrode (SCE) were then inserted as shown in Figure 8. The working distance between the tip of the reference electrode and the sample was adjusted to 2 mm and the sample was allowed to "age" for approximately 1 hour. The electrodes were connected to the Potentiostat via the electrometer as shown in Figure 11. Once "aging" of the sample was completed, the experiment was started, data recorded and polarization plots generated.

C. SAMPLE PREPARATION

The alloys to be studied were originally provided in various forms (bars, plates, rods, etc.). Most of the alloys were machined into 9.55 mm diameter by 9.55 mm height right circular cylinders and threaded for attachment to the working electrode sample holder shown in Figure 7. However, some of the samples could not be machined to the above dimensions and were produced in different shapes. This proved to be no problem since the K-47 Corrosion Cell is

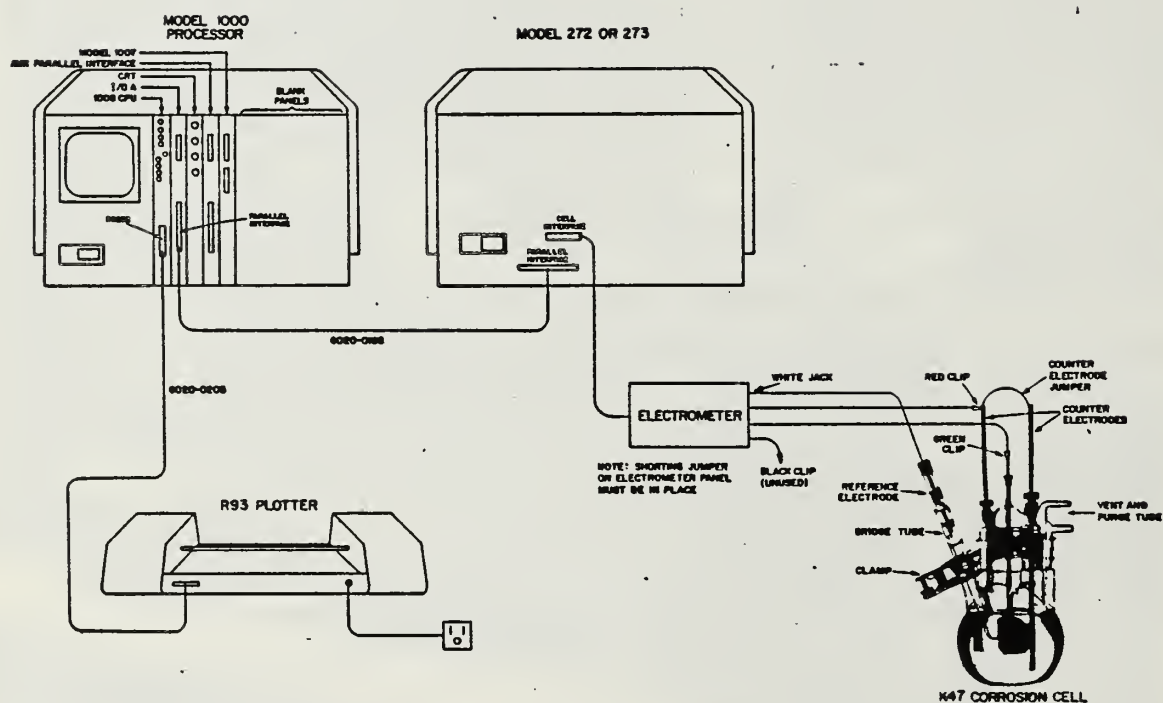


Figure 11. Electrical Connections for the Model 351 Corrosion Measurement System

designed to accommodate any threaded sample up to 45 mm diameter. In addition, the machinability of one alloy was extremely poor; in this case unthreaded samples were utilized with the flat specimen holder shown in Figure 12.

After machining, the samples were always stored in a dessicator during inactive periods. After thorough sanding with 600 grit sandpaper and prior to immersion in the corrosion cell, each sample was weighed and measured. This ensured that each sample would have a freshly prepared surface, free of any surface oxidation, prior to experimentation.

D. TESTED MATERIALS

Six high damping alloys and four "baseline" alloys were examined during this research. The nominal compositions of the high damping alloys are as follows:

Delta Alloy C	-	73.0% Cu, 21.0% Zn, 6.0% Al
Titanium-Nickel	-	50.0% Ti, 50.0% Ni
INCRAMUTE	-	58.0% Cu, 40.0% Mn, 2.0% Al
SONOSTON	-	37.0% Cu, 54.25% Mn, 4.25% Al, 3.0% Fe, 1.5% Ni
Fe-Cr-Mo	-	85.43% Fe, 11.65% Cr, 2.92% Mo
Fe-Cr-Al	-	85.51% Fe, 11.60%, 2.89% Al

The nominal chemical composition of the baseline alloys were as follows:

304 Stainless Steel	-	71.92% Fe, 18.5% Cr, 9.5% Ni, .08% C (max)
---------------------	---	---

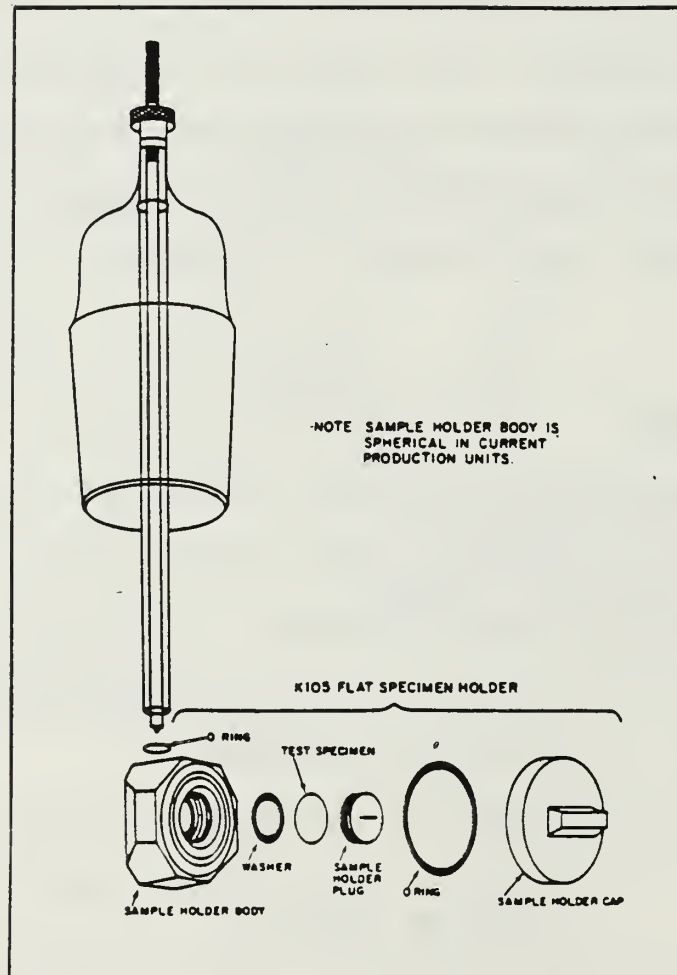


Figure 12. Exploded View of the Model K105 Flat Specimen Holder

1020 Carbon Steel	-	98.72% Fe, .30% Si, .20% C, .7% Mn, .040% S (max), .040% P (max)
7075 Aluminum	-	90% Al, 2.5% Mg, 1.6% Cu, 5.6% Zn, .30% Cr
630 Series Bronze	-	79.1% Cu, .12% Zn, .032% Sn, .021% Si, 1.4% Mn, 2.76% Fe, 5.35% Ni, 10.9% Al

E. EXPERIMENTAL PARAMETERS

Potentiodynamic Polarization and Polarization Resistance studies were conducted as part of this research. All tests were conducted in synthetic seawater (Appendix A). The following experimental parameters were used during testing:

1. Potentiodynamic Polarization Technique

a. Scanning Values

- (1) Final Potential--Typically +750 mV vs E_{corr}
- (2) Initial Potential--Typically -600 mV vs E_{corr}
- (3) Scanning Rate--1 mV per second

b. Material Characteristics

- (1) Equivalent Weight--Calculated for each specimen
- (2) Surface Area--Calculated for each specimen
- (3) Density--Calculated for each specimen

2. Polarization Resistance Technique

a. Scanning Values

- (1) Final Potential--(+25) mV vs E_{corr}
- (2) Initial Potential--(-25) mV vs E_{corr}
- (3) Scanning Rate--1 mV per second

b. Material Characteristics--same as previous method.

During all experimentation, corrosion cell temperatures were maintained at 21.5 ± 0.5 degrees C.

F. SCANNING ELECTRON MICROSCOPY

The Cambridge Model S200 Scanning Electron Microscope (SEM) was used to determine the nature of corrosive attack and the extent of film formation on the surface of each alloy. Photographs of the original as-machined samples, samples experimentally exposed in synthetic seawater, and samples exposed in natural seawater at the LaQue Center were examined. In general, machined samples were photographed at 1000X while the corroded samples were studied at magnifications up to 2000X. Prior to SEM photography, corroded samples were rinsed in distilled water to remove any salt products adhering to the surface of the sample.

G. EXPERIMENTAL PROCEDURES FOR NATURAL SEAWATER EXPOSURES

Concurrent natural seawater exposures were conducted at the LaQue Center. Specimens of the high damping alloys and the baseline alloys were exposed to ambient temperature, low flow, filtered seawater in accordance with ANSI/ASTM Standard G 52-76 ("Standard Recommended Practice for Conducting Surface Seawater Exposure Tests on Metals and Alloys"). Prior to immersion of the samples, monofilament fishing line was attached and the specimens were degreased, lightly brushed, rinsed and dried. The specimens were allowed to cool to ambient temperature prior to weighing.

Each specimen was suspended on a support bar and immersed. The 7075 aluminum alloy samples were exposed in a separate trough to prevent attack from copper ions emanating from the copper-based alloys. A continuous supply of uncontaminated, full strength seawater at a nominal velocity of 0.3 m/s was maintained (Figure 13). During the exposure in the low velocity seawater trough (Figure 14), PH, temperature, salinity, and dissolved Oxygen content were monitored. After an exposure period of 67 days, 3 to 4 samples of each alloy were removed from the seawater trough. The corrosion product was removed from each of the samples and corrosion rates and surface characteristics were recorded. One sample of each alloy was returned in its corroded state to allow for subsequent SEM analysis.

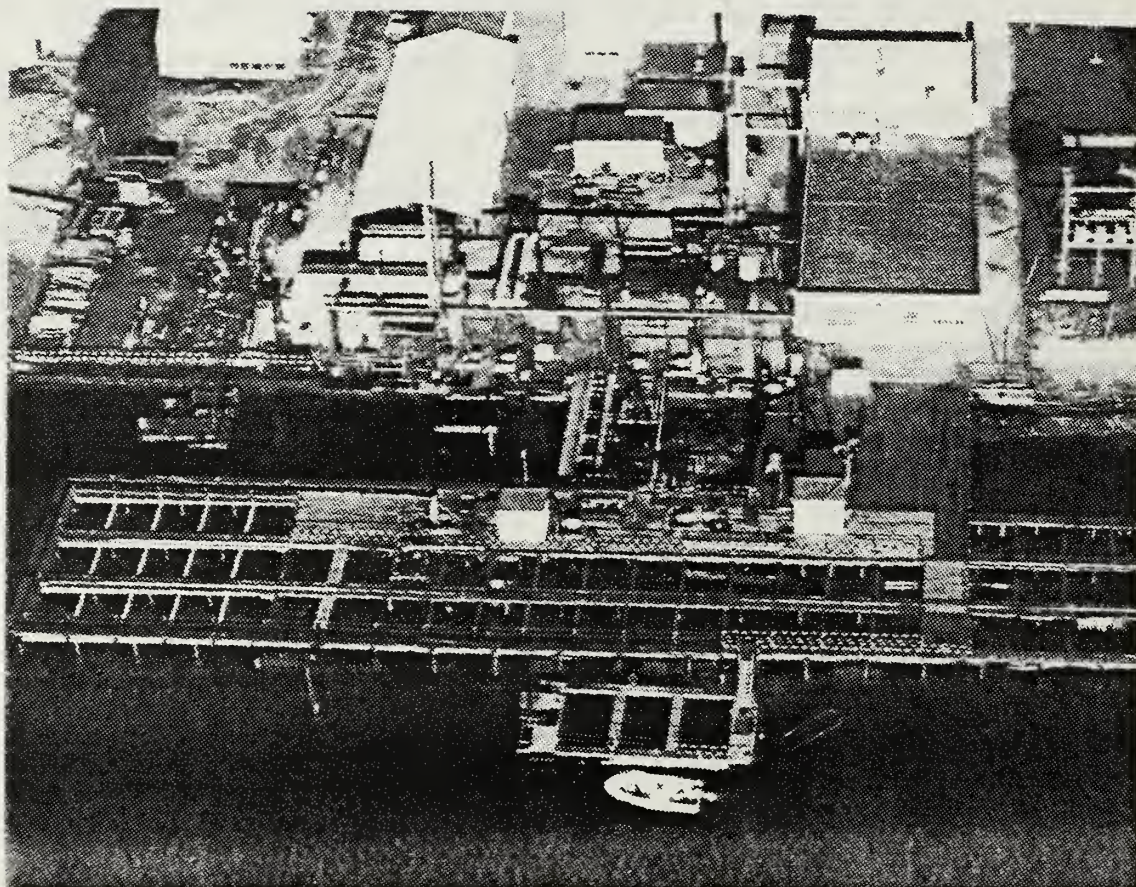


Figure 13. The LaQue Center for Corrosion Technology, Wrightsville Beach, N.C.



Figure 14. Low Velocity Seawater Exposure Trough at the LaQue Center for Corrosion Technology, Wrightsville Beach, N.C.

IV. RESULTS AND DISCUSSION

A. TITANIUM-NICKEL

The electrochemical laboratory polarization results for high damping Ti-Ni are shown in Figures 15 and 16, and microscopic observations in Figures 17 to 21. Using the PDP and LPM plots (Figures 15 and 16), Methods 1-5 yield the following results: (I_p , I_q , and i_{corr} in $\mu A/cm^2$)

Method	β_a	β_c	I_q	I_p	i_{corr}	R_{mpy}
1	0.174	0.132	-	-	1.734	0.799
2	0.174	0.132	-	-	4.960	0.216
3	-	-	6.486	7.112	3.392	1.563
4	0.100	0.100	-	-	1.116	0.535
5	0.100	0.100	-	-	3.090	<u>1.440</u>
					AVG	1.348

Direct weight loss results from seawater exposure at the LaQue Center are:

Sample	R_{mpy}	Maximum Attack (mils)
1	< 0.1	0.0
2	< 0.1	0.0
3	<u>< 0.1</u>	<u>0.0</u>
AVG	< 0.1	AVG 0.0

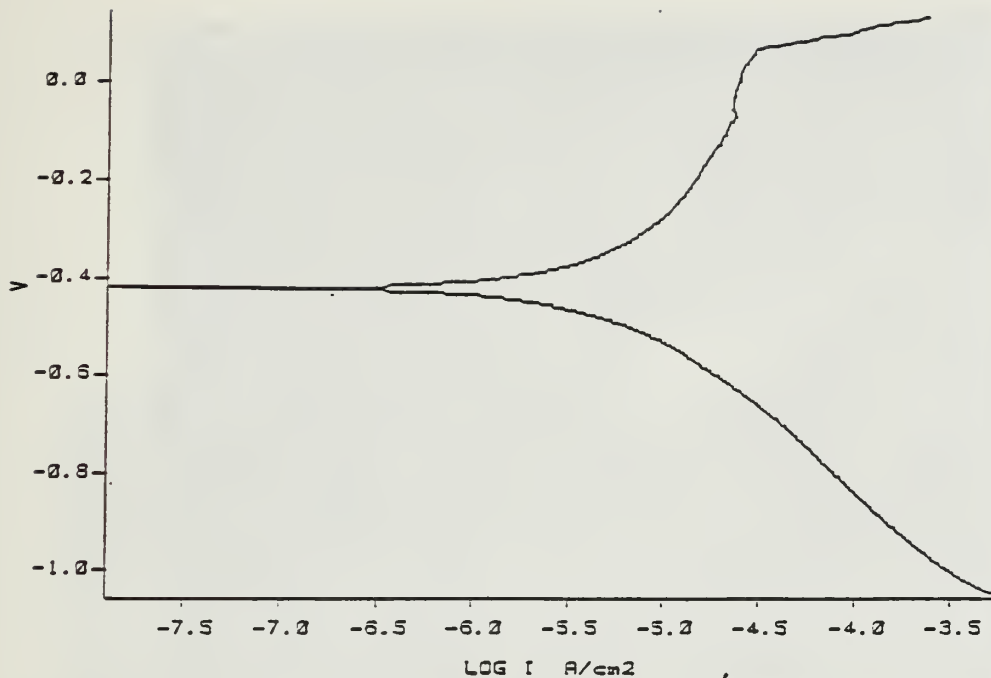


Figure 15. Potentiodynamic Polarization Plot for Ti-Ni in Synthetic Seawater

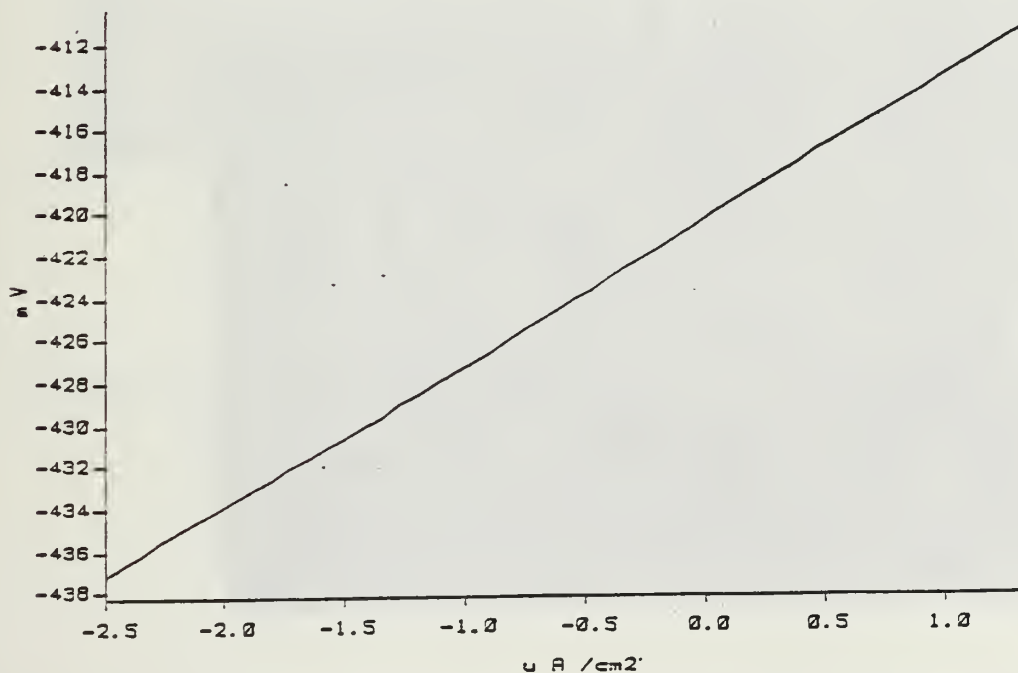


Figure 16. Polarization Resistance Plot for Ti-Ni in Synthetic Seawater

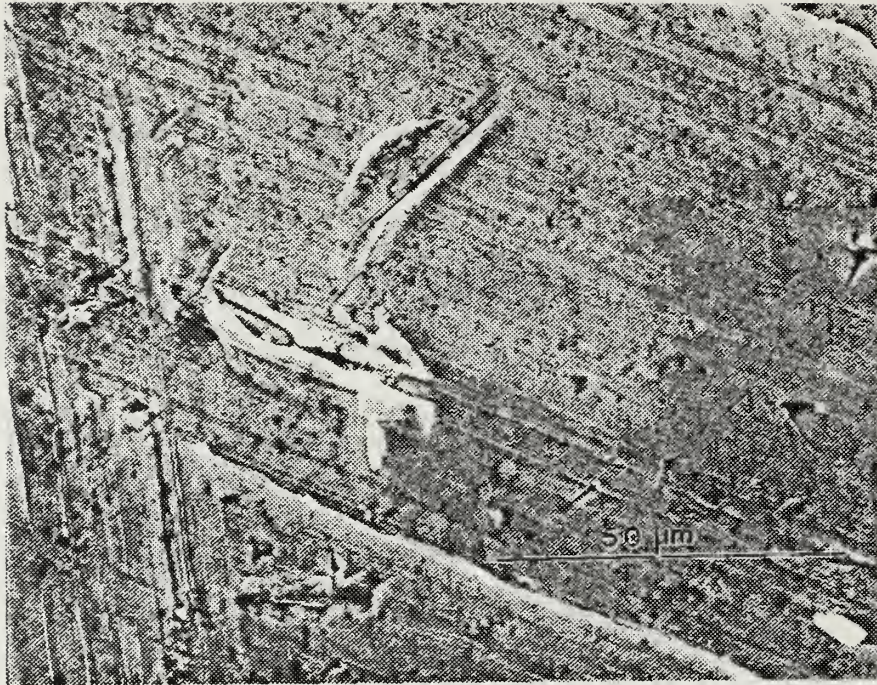


Figure 17. As-Machined Surface of Ti-Ni Prior to Corrosion Experimentation, 1000X

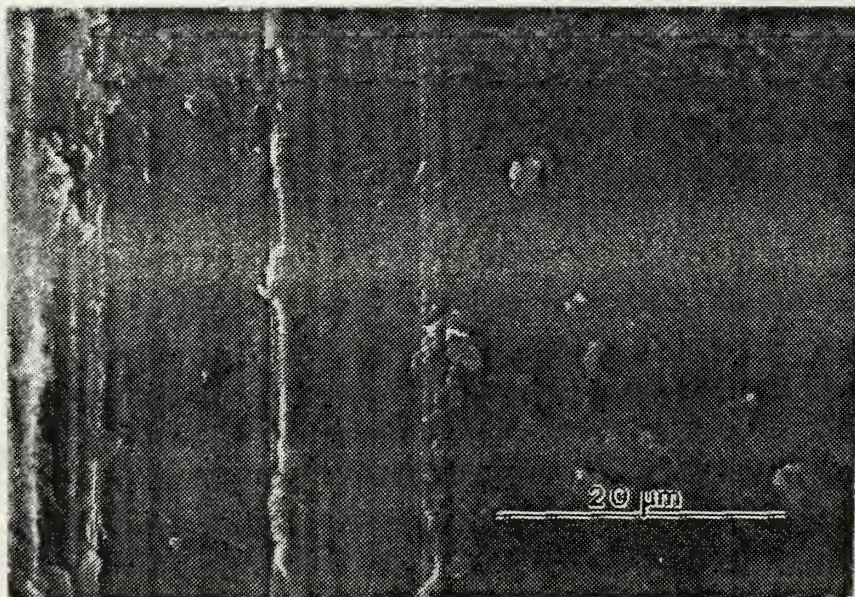


Figure 18. Corrosion Product on Ti-Ni after Polarization Experimentation, 2000X

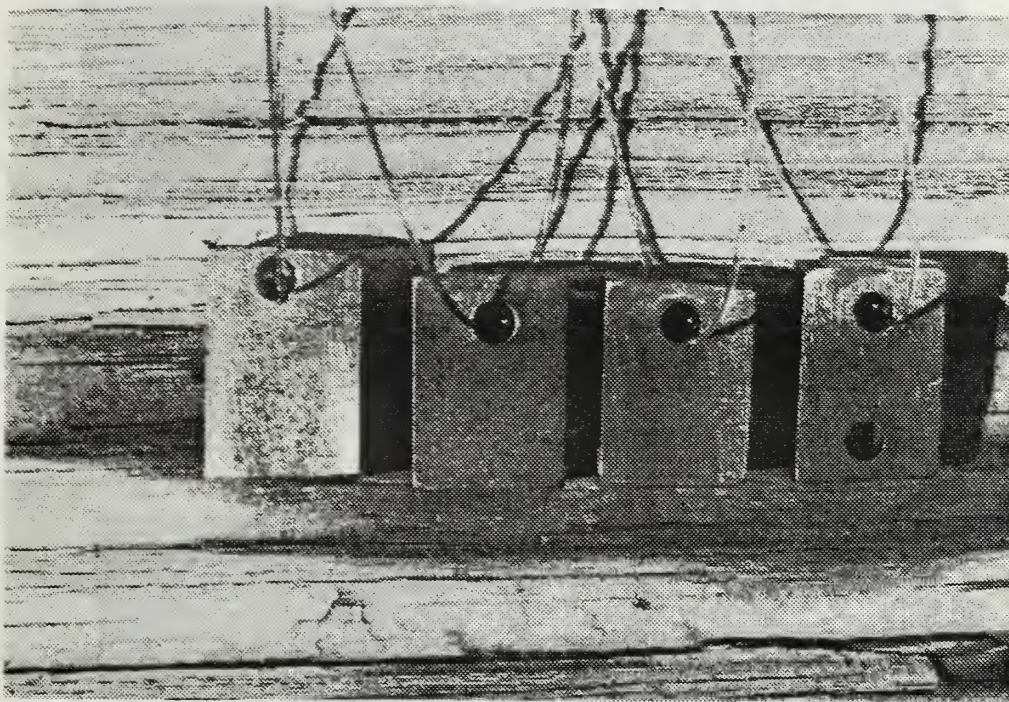


Figure 19. Ti-Ni Samples after Removal from
Exposure Troughs at the LaQue Center
Following an Exposure Period of 67 Days



Figure 20. Corroded Surface of Ti-Ni after a 67 Day Exposure at the LaQue Center, 25X

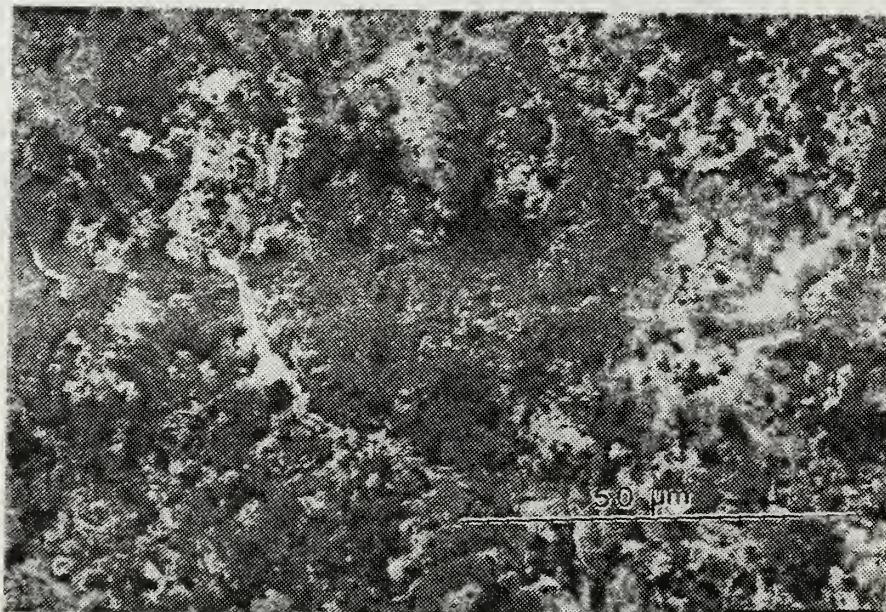


Figure 21. Corroded Surface of Ti-Ni after a 67 Day Exposure at the LaQue Center, 1000X

Agreement between laboratory and LaQue results was not that good, but this is not surprising in view of the very low corrosion rates. The PDP plot showed a potential range where a film is apparently trying to form (-0.3 V 0.0 V), with an apparent film breakdown at approximately 0.05 V. Figures 17 through 21 support this conclusion. The Ti-Ni lab samples displayed a definite film, evenly distributed across the surface. Specimens photographed immediately after removal from the seawater exposure troughs at the LaQue Center showed a slightly tarnished surface; these Ti-Ni samples demonstrated excellent corrosion resistance in the actual marine environment. Samples exposed in seawater for 67 days had a minimal corrosion rate and no evidence of pitting or localized corrosion.

B. 1020 CARBON STEEL

The polarization results for 1020 Carbon steel are shown in Figures 22 and 23; microscopic observations in Figures 24 to 29. Using the PDP plot and the LPM plot (Figures 22 and 23), Methods 1-5 yield the following results: (I_p , I_q , and i_{corr} in $\mu A/cm^2$)

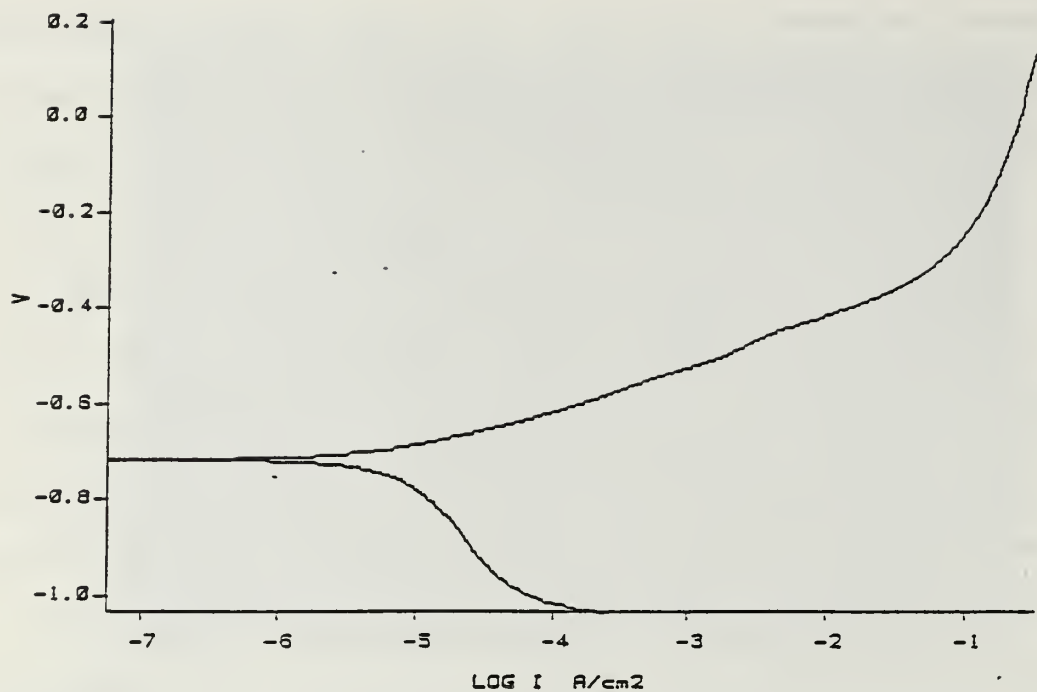


Figure 22. Potentiodynamic Polarization Plot for 1020 C Steel in Synthetic Seawater

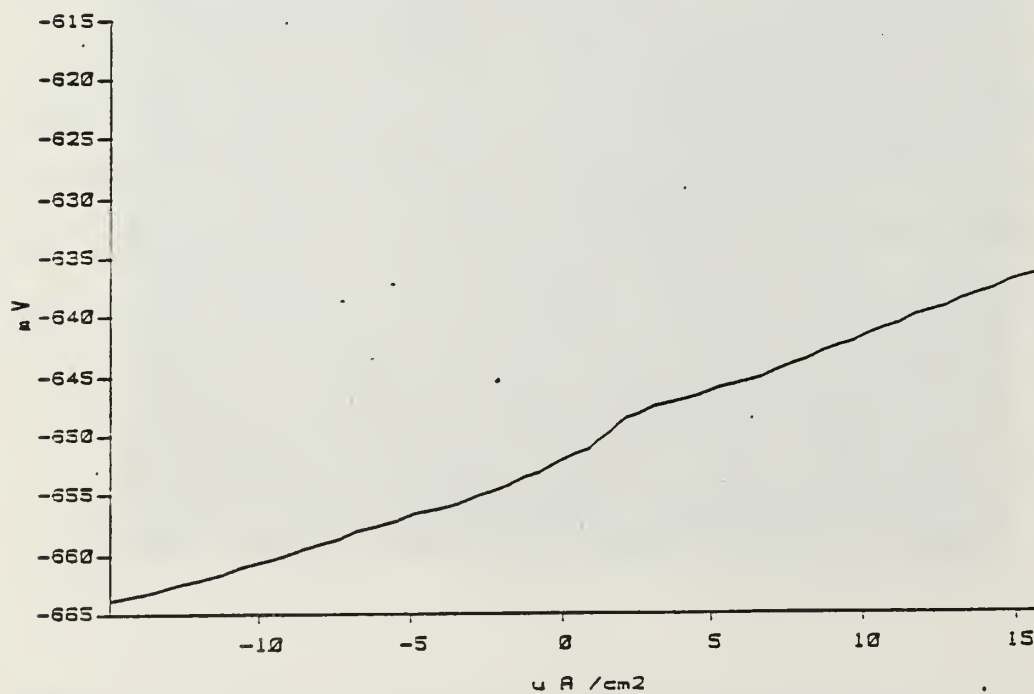


Figure 23. Polarization Resistance Plot for 1020 C Steel in Synthetic Seawater



Figure 24. As-Machined Surface of 1020 C Steel Prior to Corrosion Experimentation, 1000X

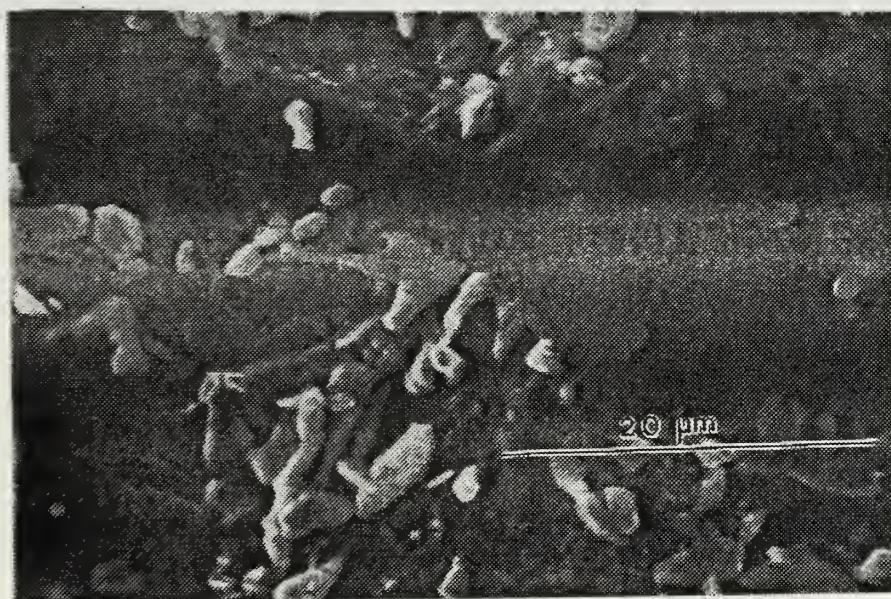


Figure 25. Corrosion Product on 1020 C Steel after Polarization Experimentation, 2160X

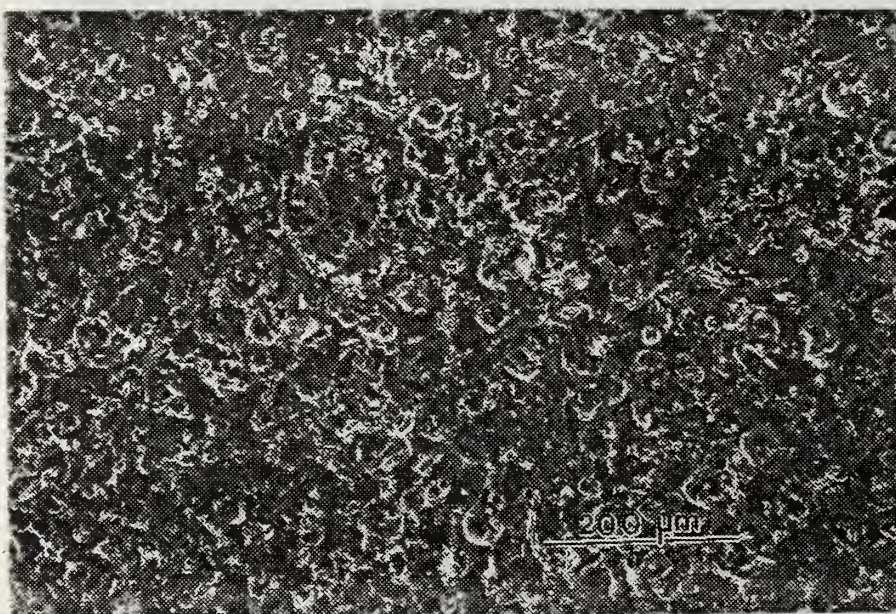


Figure 26. Corrosion Product on 1020 C Steel after Polarization Experimentation, 123X

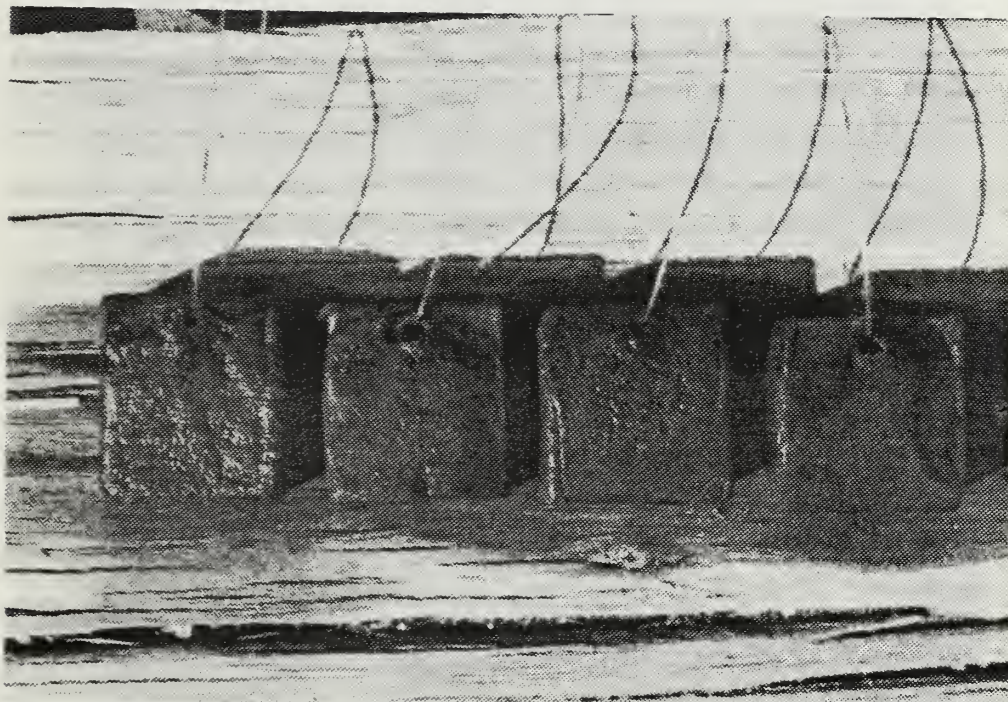


Figure 27. 1020 C Steel Samples after Removal from Exposure Troughs at the LaQue Center Following an Exposure Period of 67 Days

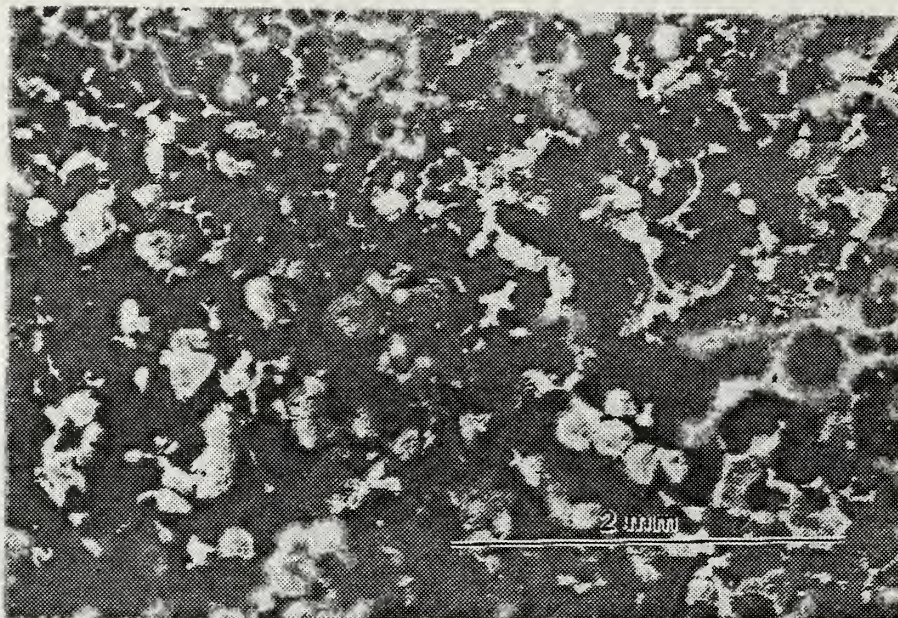


Figure 28. Corroded Surface of 1020 C Steel after a 67 Day Exposure at the LaQue Center, 26X

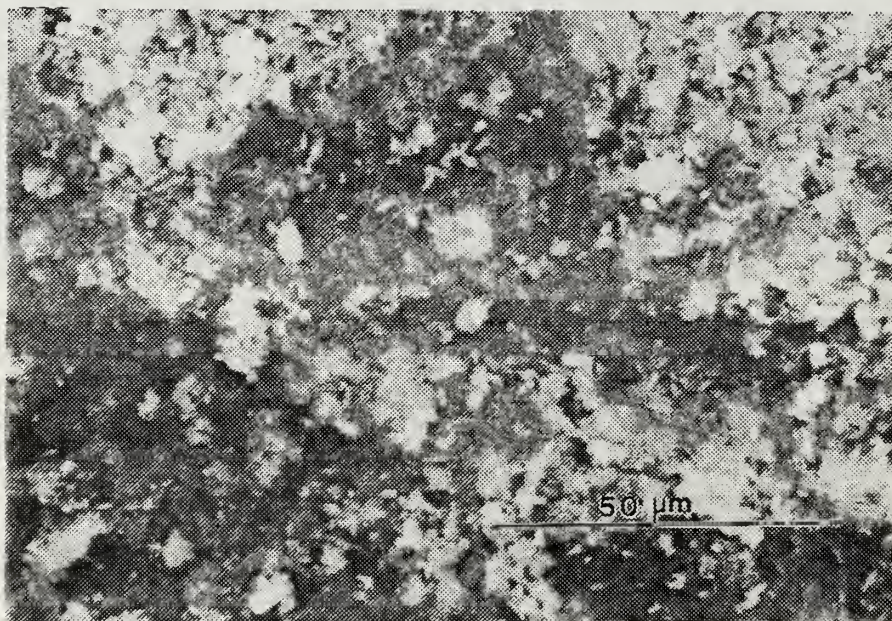


Figure 29. Corroded Surface of 1020 C Steel after a 67 Day Exposure at the LaQue Center, 1000X

Method	β_a	β_c	I_q	I_p	i_{corr}	Rmpy
1	0.068	0.114	-	-	3.837	1.805
2	0.068	0.114	-	-	17.201	8.110
3	-	-	-	-	-	-
4	0.100	0.100	-	-	3.069	1.450
5	0.100	0.100	-	-	20.202	<u>9.540</u>
						AVG 5.226

Direct weight loss results from seawater exposure are:

Sample	Rmpy	Maximum Attack (mils)
1	3.7	3.1
2	3.1	0.8
3	<u>3.6</u>	<u>0.8</u>
AVG	3.47	AVG 1.57

Agreement between laboratory results and the LaQue on-site results was quite good in this case. The PDP plot showed a consistently increasing current density until approximately -0.2 V. Beyond this potential, current density remained fairly constant. No evidence of film formation was shown on the PDP plot. However, Figures 24 through 29 indicate that some type of corrosion product was forming. Samples exposed in the actual seawater trials, photographed immediately after removal (Figure 27), had a thick, porous coating over the entire surface; here we can note that the corrosion product has already begun to drop off the specimen. The corrosion product does not adhere to

the surface, seems extremely vulnerable to any disturbance, and does not constitute an effective protective film.

C. 7075 ALUMINUM

The electrochemical results for 7075 aluminum samples are shown in Figures 30 and 31, the surface appearances in Figures 32 to 36. Using the PDP and LPM plots (Figures 30 and 31), Methods 1-5 yield the following results: (I_p , I_q , and i_{corr} in $\mu A/cm^2$)

Method	β_a	β_c	I_q	I_p	i_{corr}	Rmpy
1	0.087	0.062	-	-	0.421	0.176
2	0.087	0.062	-	-	0.994	0.415
3	-	-	2.014	1.213	0.757	0.316
4	0.100	0.100	-	-	0.590	0.246
5	0.100	0.100	-	-	1.370	<u>0.571</u>
AVG						0.345

Direct weight loss results from seawater exposure are:

Sample	Rmpy	Maximum Attack (mils)
1	4.0	7.9 (Pitting)
2	4.6	24.0 (Pitting)
3	<u>4.2</u>	<u>15.7 (Pitting)</u>
AVG	4.27	AVG 15.87

The classical "muddying effect" is seen in Figure 33 on the surface of 7075 aluminum samples polarized anodically in synthetic seawater. These specimens showed a thick, black

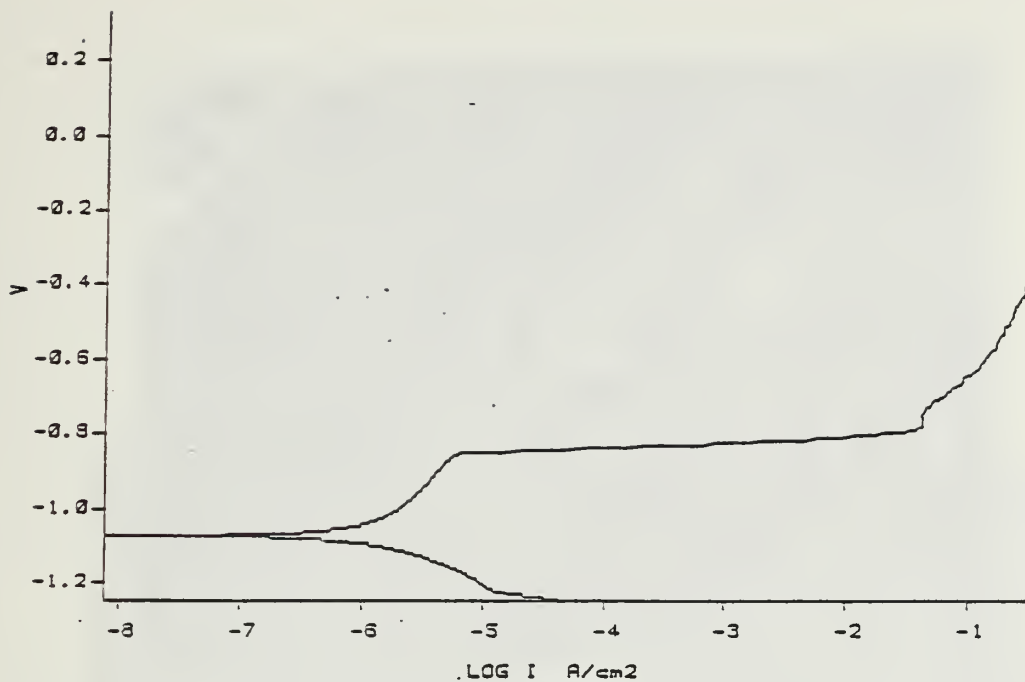


Figure 30. Potentiodynamic Polarization Plot for 7075 Aluminum in Synthetic Seawater

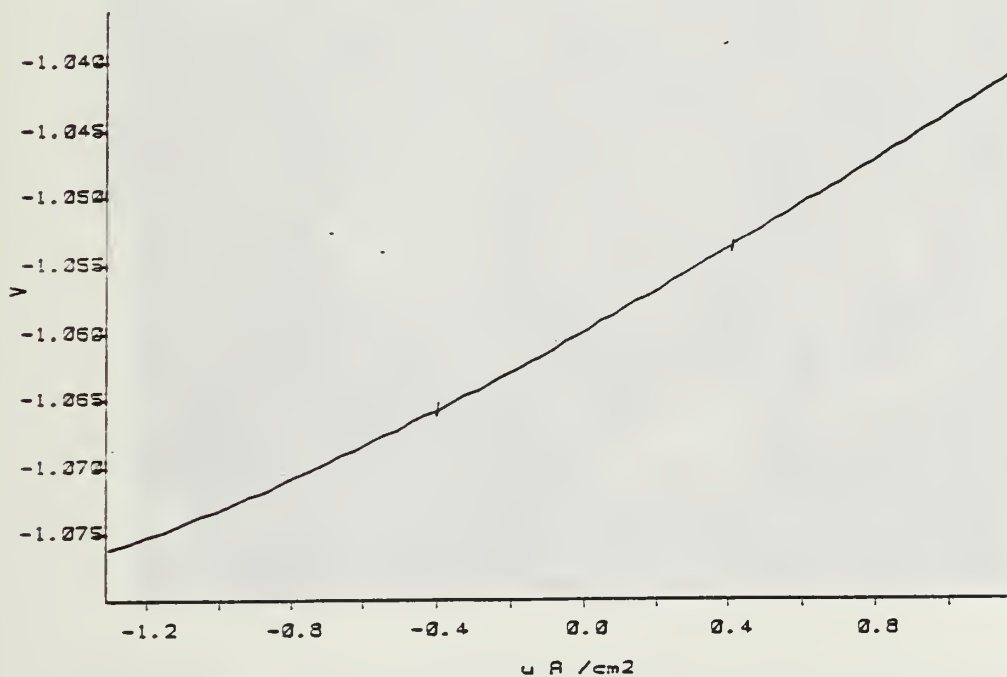


Figure 31. Polarization Resistance Plot for 7075 Aluminum in Synthetic Seawater

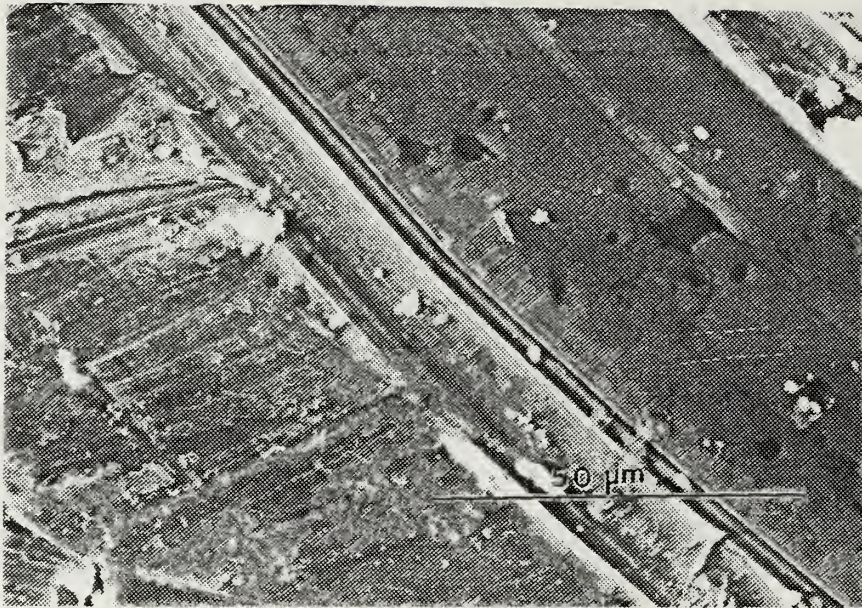


Figure 32. As-Machined Surface of 7075 Aluminum Prior to Corrosion Experimentation, 1000X

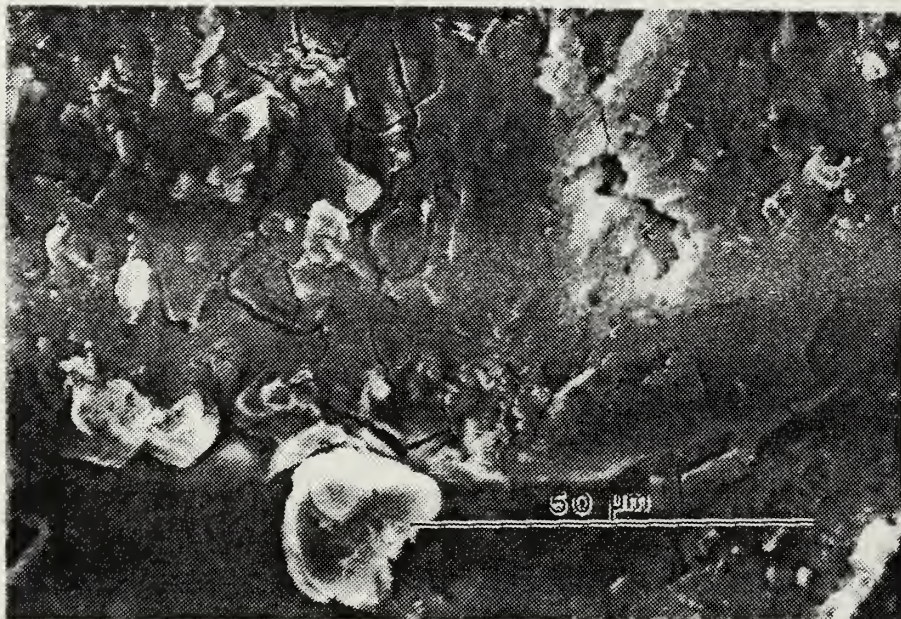


Figure 33. Corrosion Product on 7075 Aluminum after Polarization Experimentation, 1000X

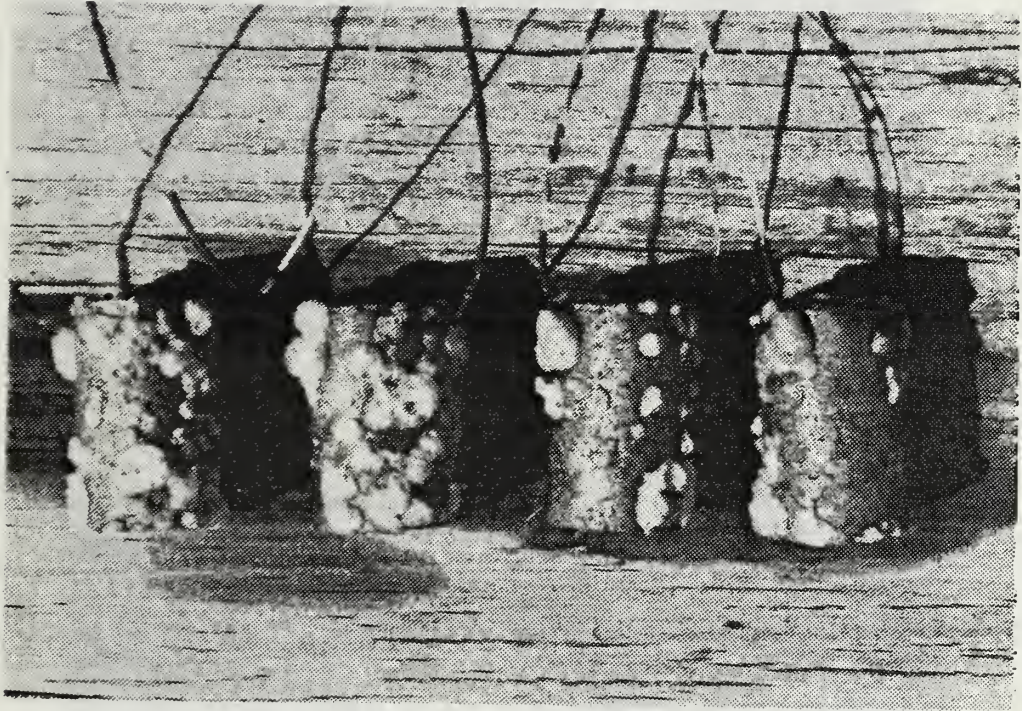


Figure 34. 7075 Aluminum Samples after Removal from Exposure Troughs at the LaQue Center Following an Exposure Period of 67 Days

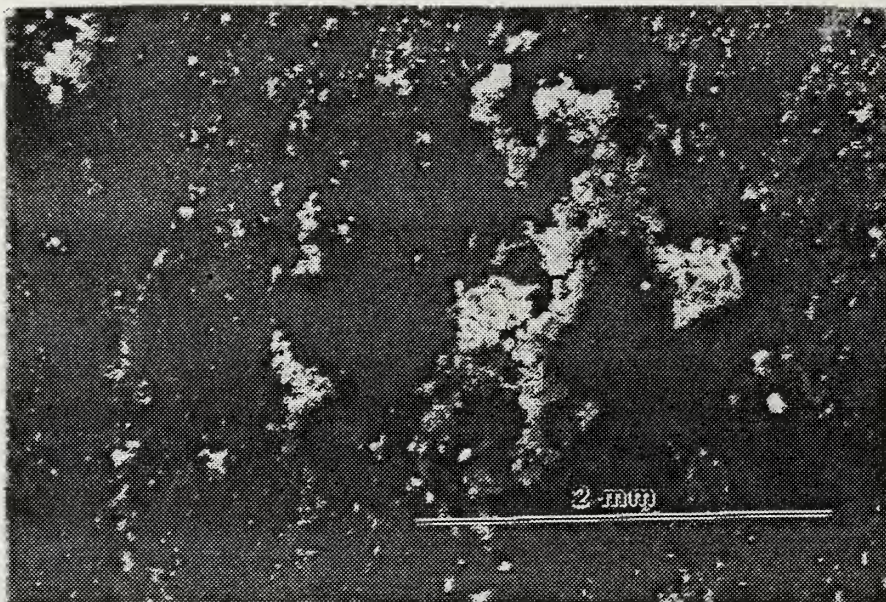


Figure 35. Corroded Surface of 7075 Aluminum after a 67 Day Exposure at the LaQue Center, 25X



Figure 36. Corroded Surface of 7075 Aluminum after a 67 Day Exposure at the LaQue Center, 1000X

porous coating that failed to adhere to the surface. This tendency could explain the significantly lower corrosion rates experienced by samples in the laboratory. Examination of actual seawater-exposed samples (Figure 34) also show certain areas of dark oxidation. However, these samples also are characterized by severe localized corrosion (white oxidation product) and significant pitting (15.87 mils), in agreement with the PDP plot. Figures 35 and 36 show a similar surface appearance to the laboratory exposures as well as regions of "outcropping" oxides. This severe localized corrosion experienced in the seawater exposures directly affects the Rmpy calculated at the Laque Center, which indicates a significantly higher rate of corrosion than that measured in the laboratory for the relatively unadvanced and essentially general corrosion. Other experimental results have confirmed the wide discrepancy between laboratory and seawater corrosion rates for aluminum alloys [Refs. 6,7].

D. 304 STAINLESS STEEL

The polarization results for Type 304 stainless steel are shown in Figures 37 and 38. Surface morphologies are shown in Figures 39 to 43. Using the PDP plot and the LPM plot (Figures 37 and 38), Methods 1-5 yield the following results: (I_p , I_q and i_{corr} in $\mu A/cm^2$)

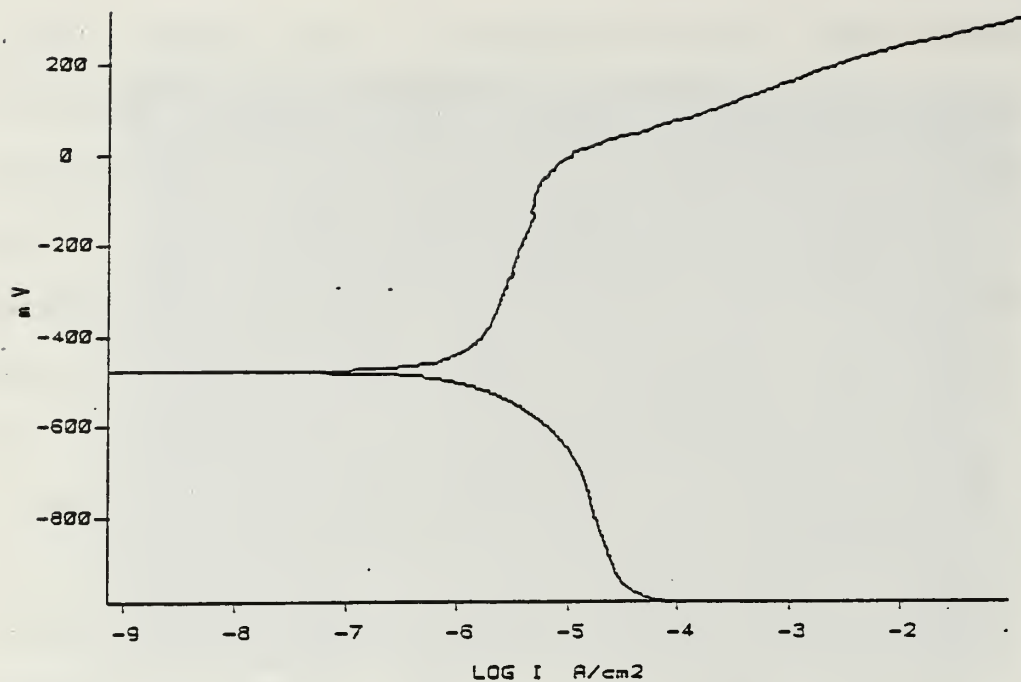


Figure 37. Potentiodynamic Polarization Plot for 304 Stainless Steel in Synthetic Seawater

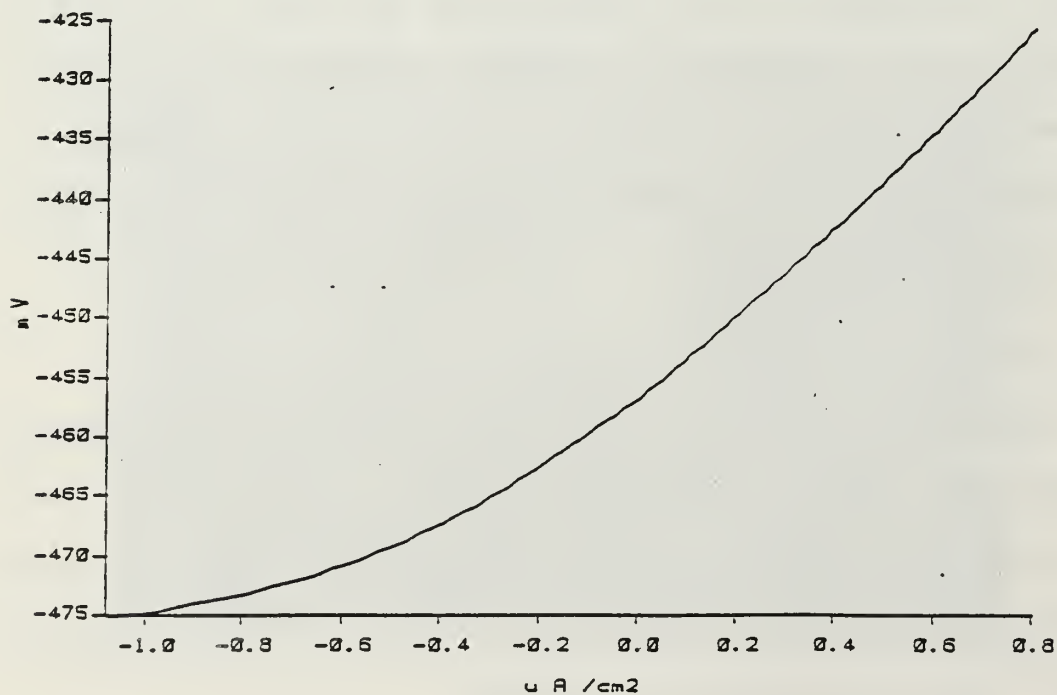


Figure 38. Polarization Resistance Plot for 304 Stainless Steel in Synthetic Seawater

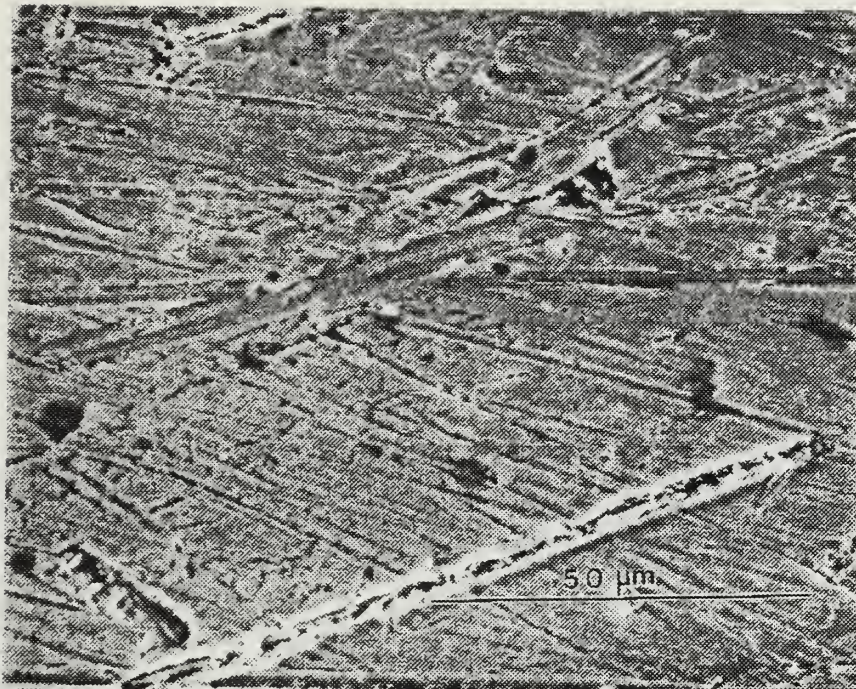


Figure 39. As-Machined Surface of 304 Stainless Steel Prior to Corrosion Experimentation, 1000X

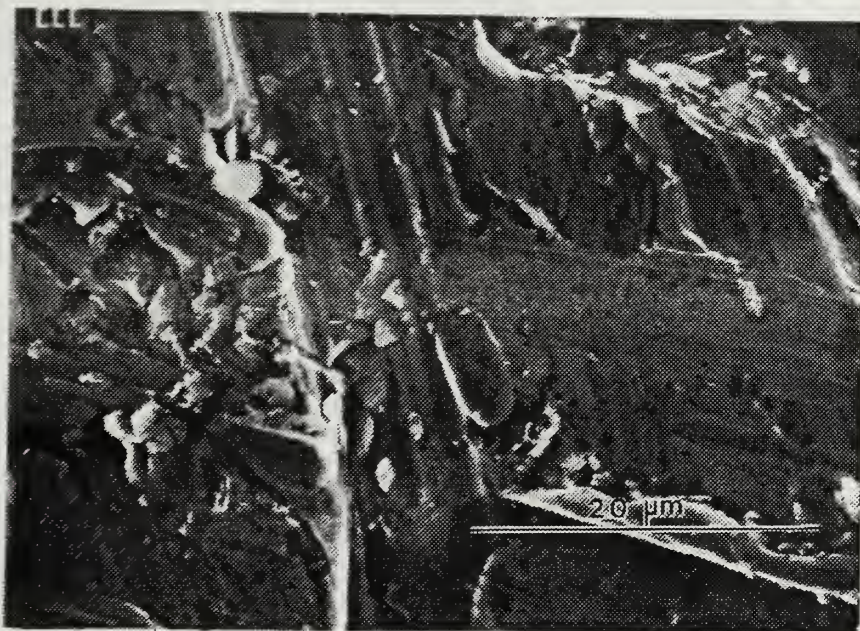


Figure 40. Corrosion Product on 304 Stainless Steel after Polarization Experimentation, 2000X

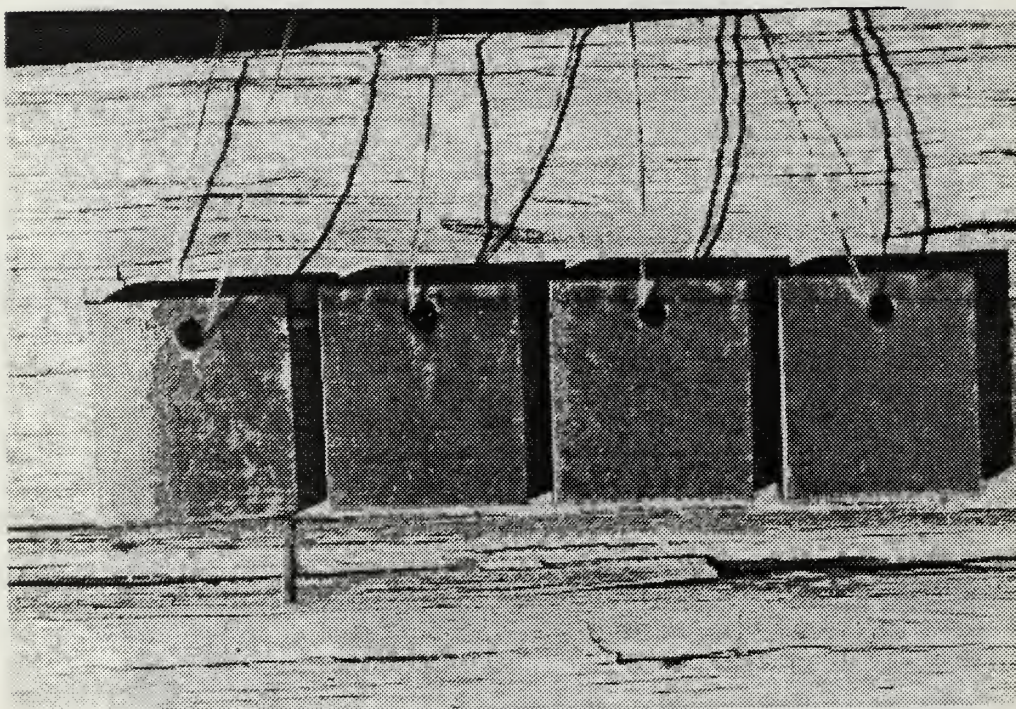


Figure 41. 304 Stainless Steel Samples after Removal from Exposure Troughs at the LaQue Center Following an Exposure Period of 67 Days



Figure 42. Corroded Surface of 304 Stainless Steel after a 67 Day Exposure at the LaQue Center, 26X

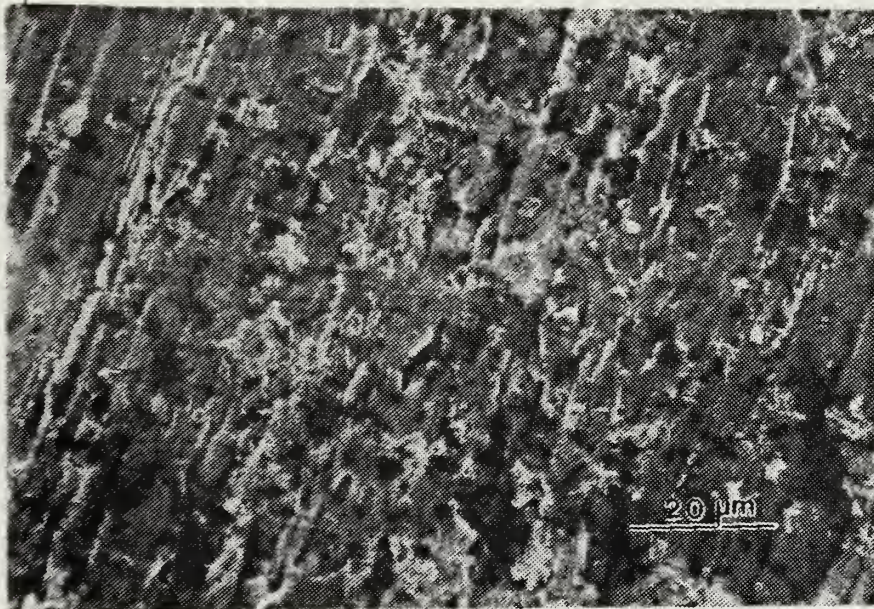


Figure 43. Corroded Surface of 304 Stainless Steel after a 67 Day Exposure at the LaQue Center, 1000X

Method	β_a	β_c	I_q	I_p	i_{corr}	Rmpy
1	0.178	0.161	-	-	0.728	0.329
2	0.178	0.161	-	-	1.190	0.537
3	-	-	7.690	1.393	1.173	0.533
4	0.100	0.100	-	-	0.481	0.218
5	0.100	0.100	-	-	0.702	<u>0.318</u>
AVG						0.387

Direct weight loss results from seawater exposure are:

Sample	Rmpy	Maximum Attack (mils)
1	0.0	0.0
2	<0.1	0.0
3	<u>0.0</u>	<u>0.0</u>
AVG	<0.1	AVG 0.0

Both the laboratory and LaQue results confirmed the low corrosion rate of 304 stainless steel in seawater. Figures 40 through 43 all show a uniform coating on the surface. This observation is in agreement with the PDP plot. No localized corrosion or pitting was indicated after a 67 day sea exposure period. Previous experimentation has indicated that 304 stainless steel shows only slight tendencies toward pitting when exposed to seawater [Ref. 8].

E. FE-CR-MO

Lab results for samples of the high damping Fe-Cr-Mo alloy (essentially ferritic stainless steel composition) are

presented in Figures 44 and 45, surfaces in Figures 46 to 51. Using the PDP and LPM plots (Figures 44 and 45), Methods 1-5 yield the following results: (I_p , I_q , and i_{corr} in $\mu A/cm^2$)

Method	β_a	β_c	I_q	I_q	i_{corr}	Rmpy
1	0.121	0.141	-	-	0.804	0.380
2	0.121	0.141	-	-	2.060	0.974
3	-	-	6.180	2.228	1.638	0.775
4	0.100	0.100	-	-	0.608	0.288
5	0.100	0.100	-	-	1.590	<u>0.750</u>
AVG						0.633

Direct weight loss results from seawater exposure are:

Sample	Rmpy	Maximum Attack (mils)
1	2.7	47.2 (Pitting)
2	<u>2.3</u>	<u>64.2 (Pitting)</u>
AVG	2.50	AVG 55.7

PDP results indicated that this alloy has a tendency for film formation. Corrosion rates for seawater and laboratory exposures were low to moderate. However, this alloy exhibited severe localized corrosion. SEM photography conducted on laboratory samples (Figures 47 and 48) clearly shows the development of the initial "attack points," which are uniformly distributed across the surface. Figure 48 shows a partially formed film near an attack point. Samples

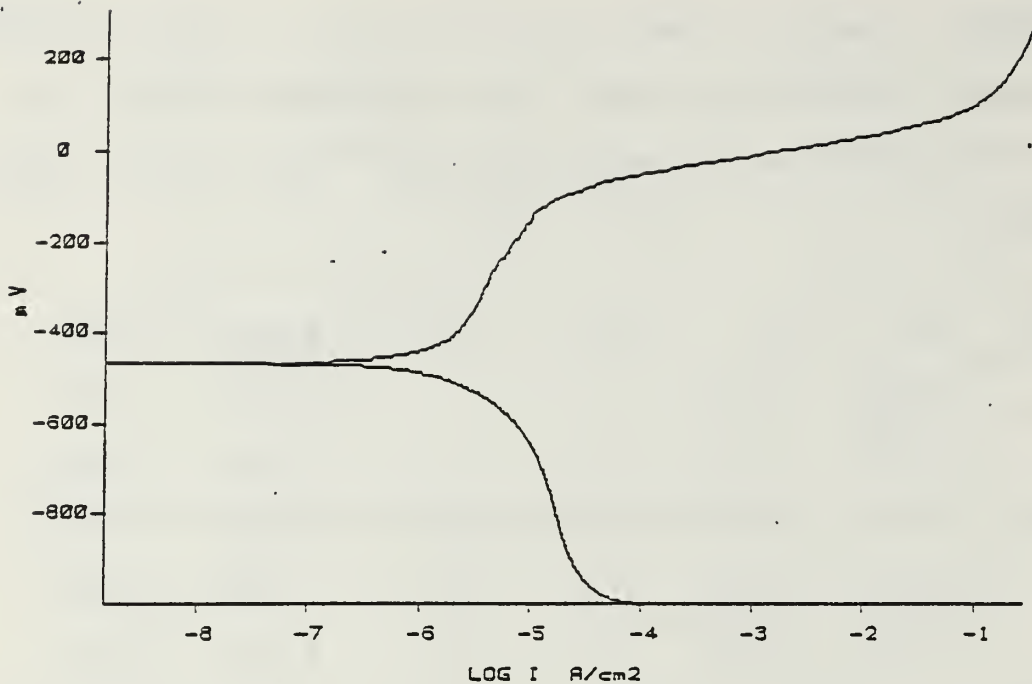


Figure 44. Potentiodynamic Polarization Plot for Fe-Cr-Mo in Synthetic Seawater

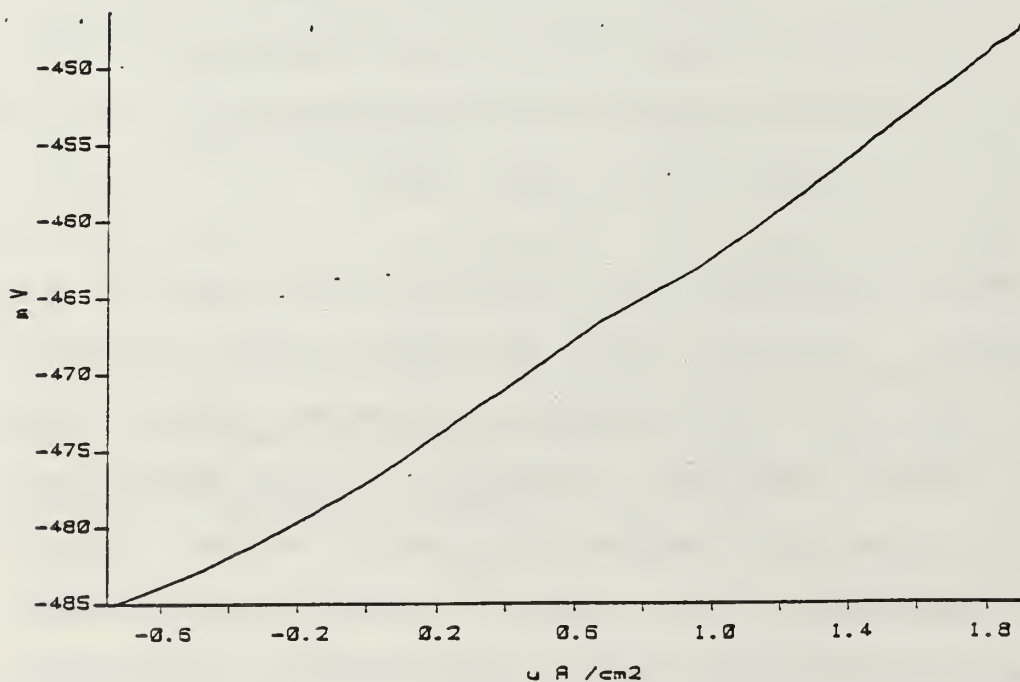


Figure 45. Polarization Resistance Plot for Fe-Cr-Mo in Synthetic Seawater



Figure 46. As-Machined Surface of Fe-Cr-Mo Prior to Corrosion Experimentation, 1000X

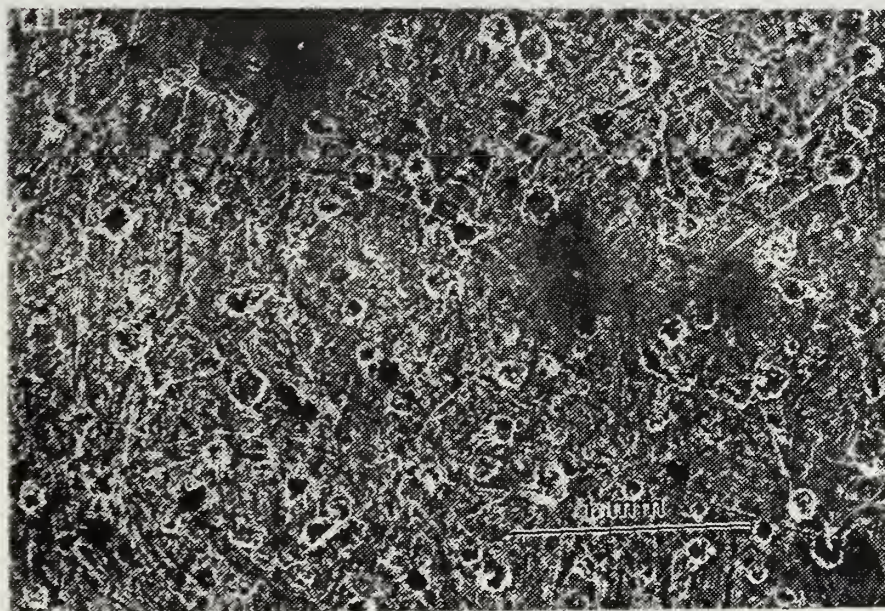


Figure 47. Corrosion Product on Fe-Cr-Mo after Polarization Experimentation, 31X

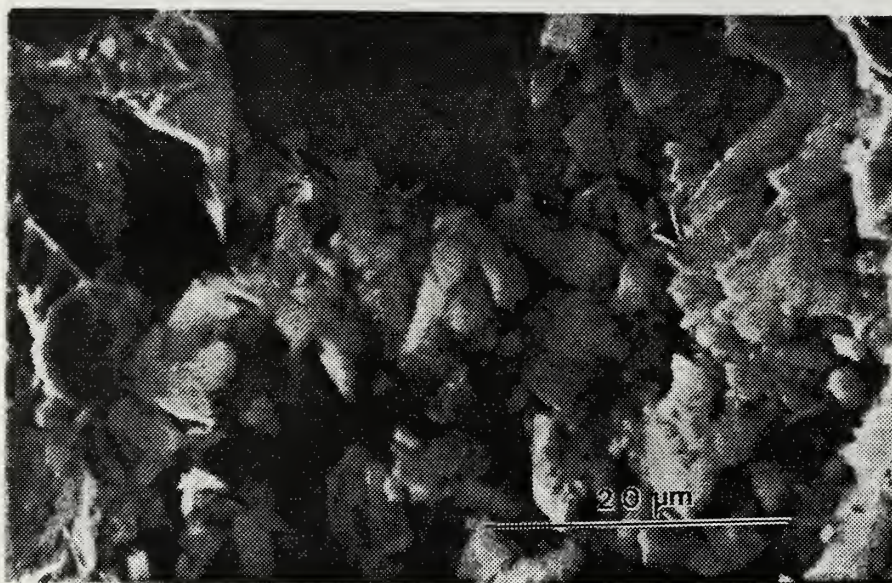


Figure 48. Corrosion Product on Fe-Cr-Mo after Polarization Experimentation, 2000X



Figure 49. Fe-Cr-Mo Samples after Removal from Exposure Troughs at the LaQue Center Following an Exposure Period of 67 Days

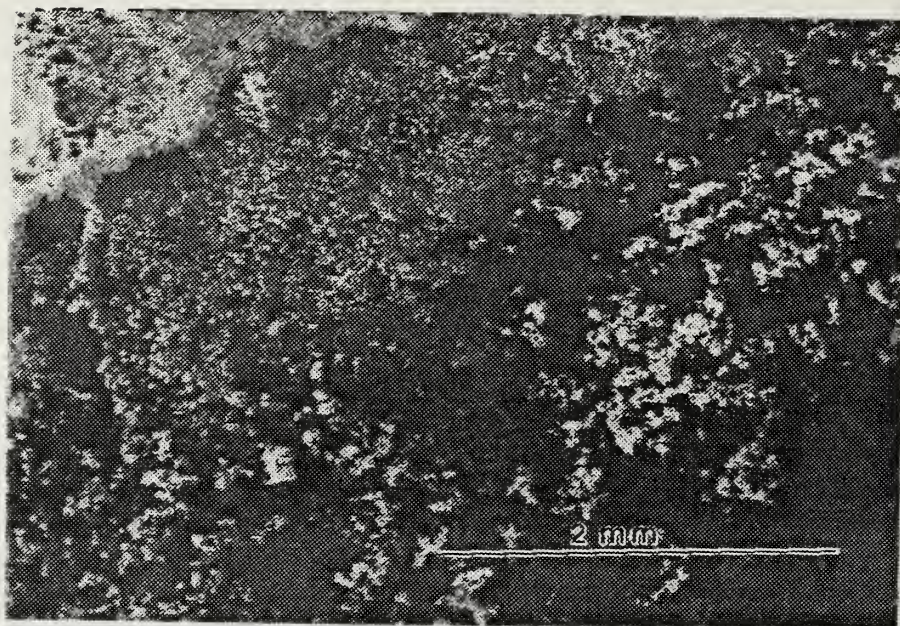


Figure 50. Corroded Surface of Fe-Cr-Mo after a 67 Day Exposure at the LaQue Center, 25X

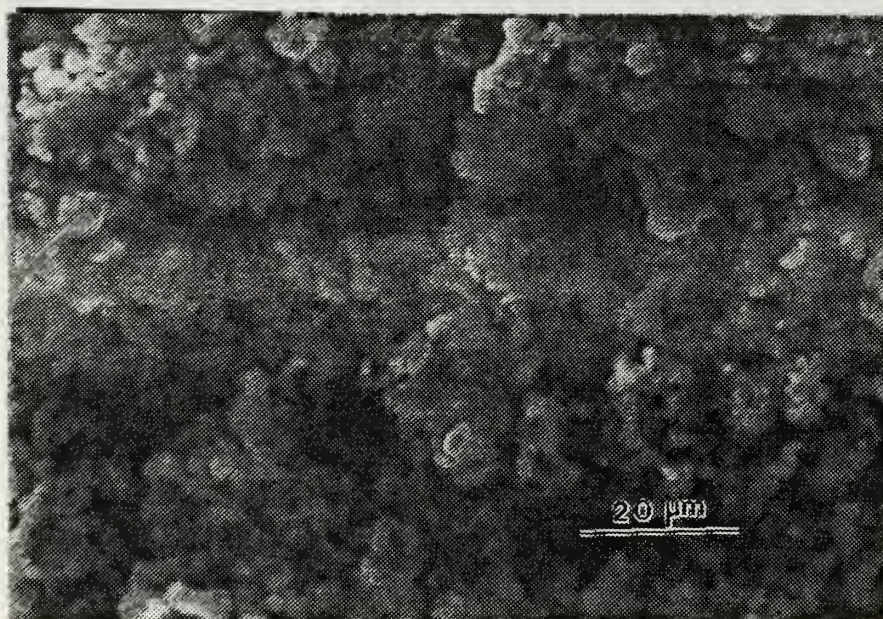


Figure 51. Corroded Surface of Fe-Cr-Mo after a 67 Day Exposure at the LaQue Center, 1000X

exposed at the LaQue Center (Figures 49-51) show very irregular attack patterns caused by a localized breakdown of the film. SEM photography indicates that the corrosion products are "outcropping" from the darker, layered surface. Even though this alloy showed nearly identical polarization and corrosion rate data as 304 stainless steel, the Fe-Cr-Mo alloy was highly susceptible to severe pitting and was extremely sensitive to geometric features.

F. FE-CR-AL

Lab results for the other high damping Fe-Cr based alloy, an Fe-Cr-Al composition, are shown in Figures 52 and 53 with surfaces shown in Figures 54 to 59. Using the PDP plot and the LPM plot, Methods 1-5 yield the following results (I_p , I_q , and i_{corr} in $\mu A/cm^2$)

Method	β_a	β_c	I_q	I_p	i_{corr}	R_{mpy}
1	0.180	0.151	-	-	0.830	0.365
2	0.180	0.151	-	-	1.240	0.545
3	-	-	5.129	1.995	1.436	0.636
4	0.100	0.100	-	-	0.531	0.234
5	0.100	0.100	-	-	0.755	<u>0.332</u>
AVG						0.422

Direct weight loss results from seawater exposure are:

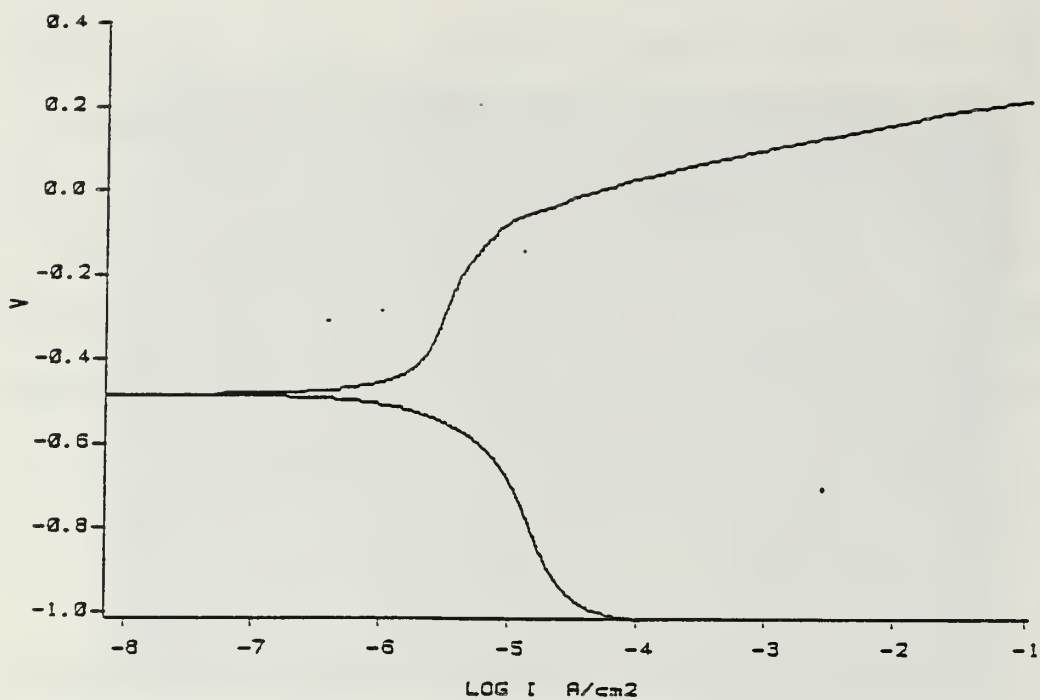


Figure 52. Potentiodynamic Polarization Plot for Fe-Cr-Al in Synthetic Seawater

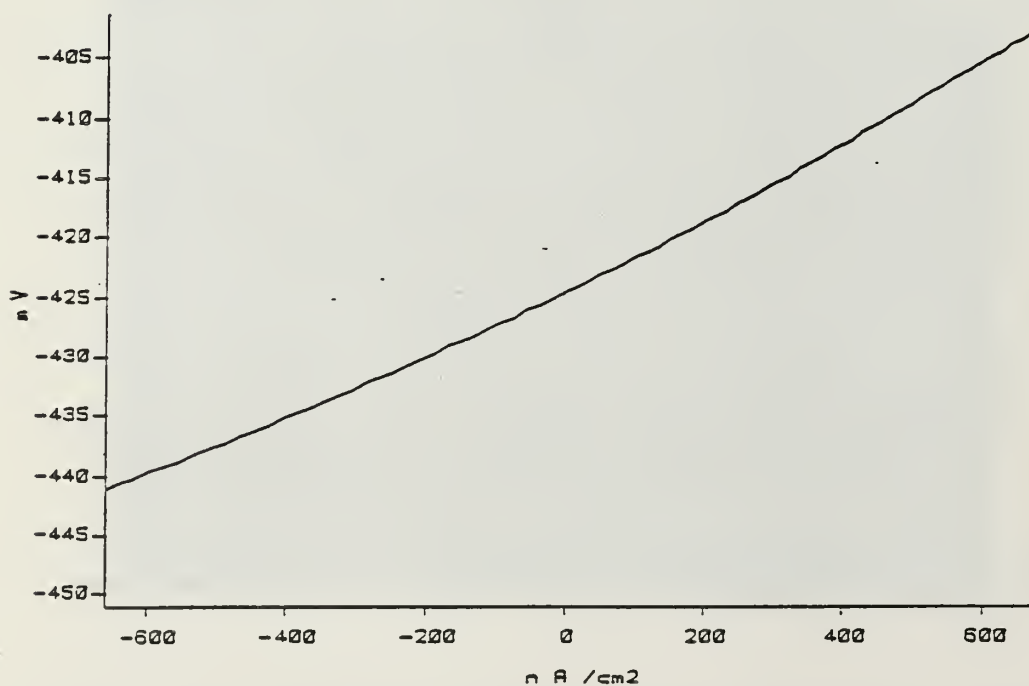


Figure 53. Polarization Resistance Plot for Fe-Cr-Al in Synthetic Seawater

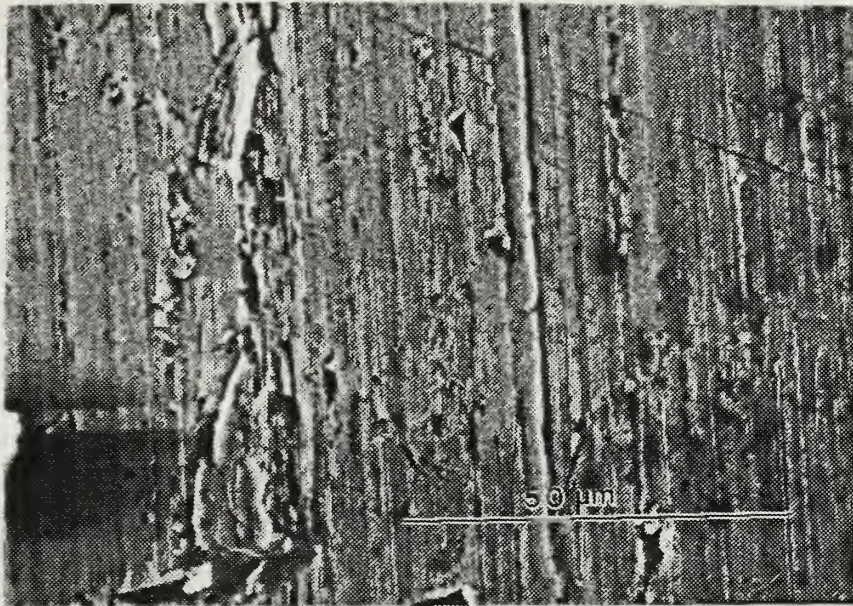


Figure 54. As-Machined Surface of Fe-Cr-Al Prior to Corrosion Experimentation, 1000X

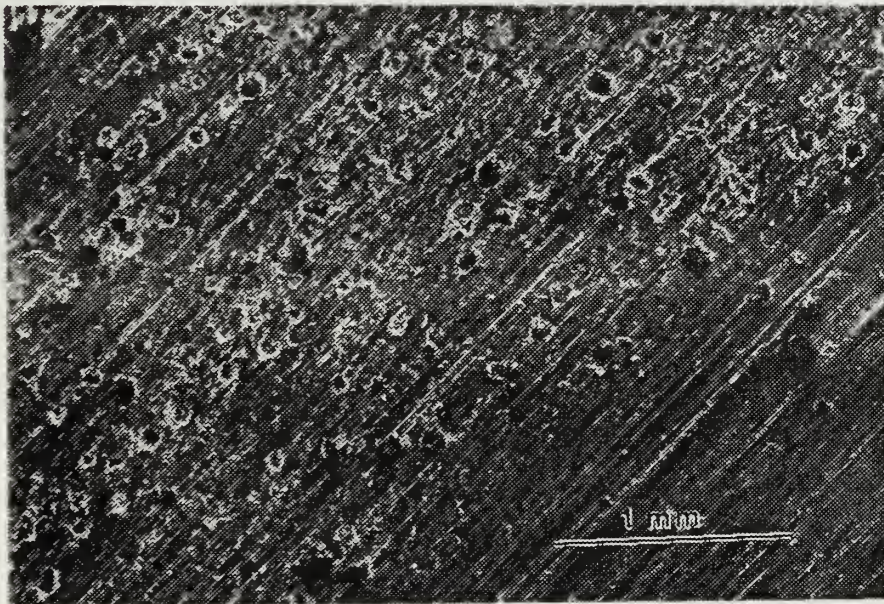


Figure 55. Corrosion Product on Fe-Cr-Al after Polarization Experimentation, 31X

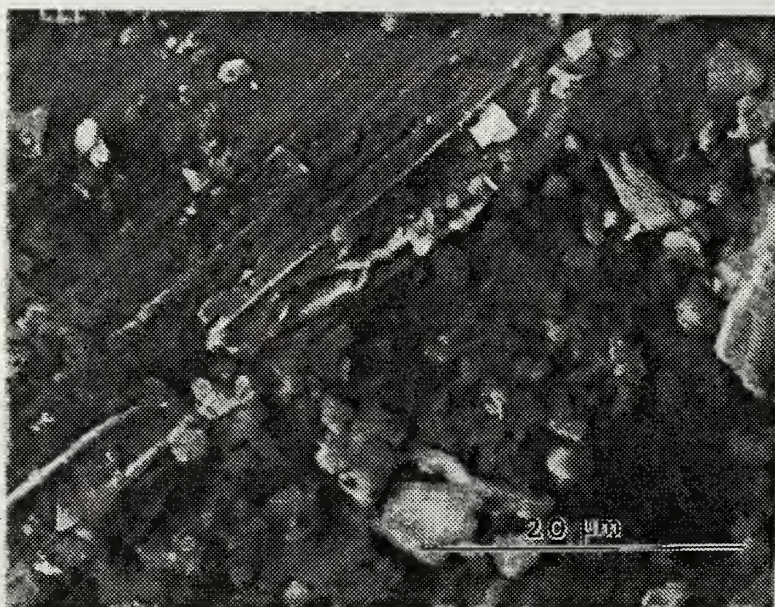


Figure 56. Corrosion Product on Fe-Cr-Al after Polarization Experimentation, 2000X

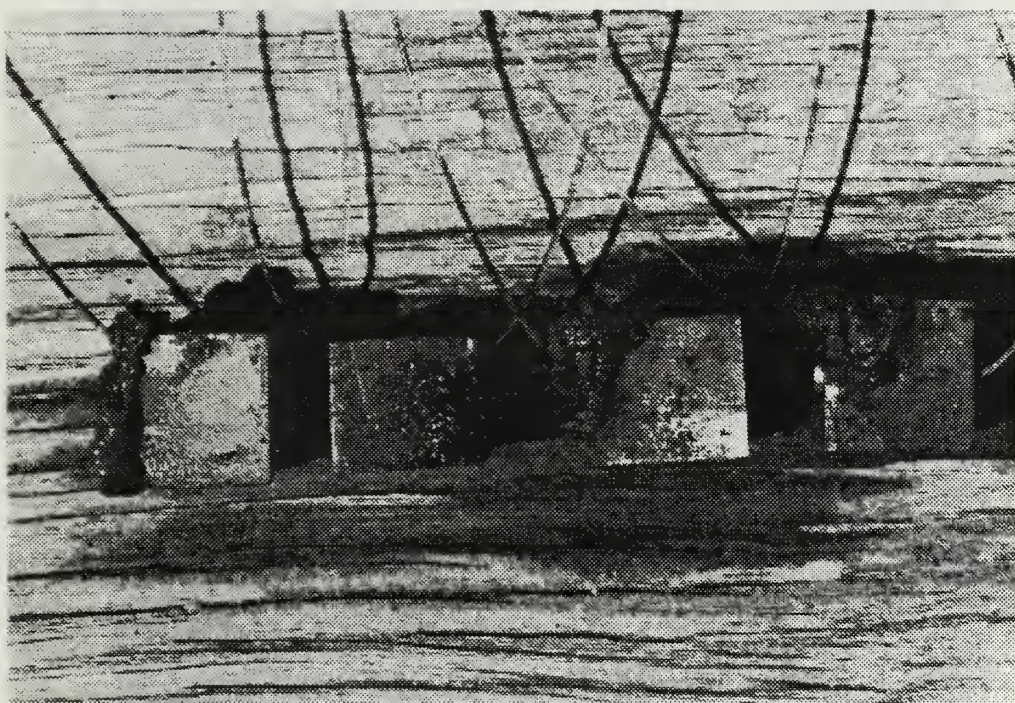


Figure 57. Fe-Cr-Al Samples after Removal from Exposure Troughs at the LaQue Center Following an Exposure Period of 67 Days

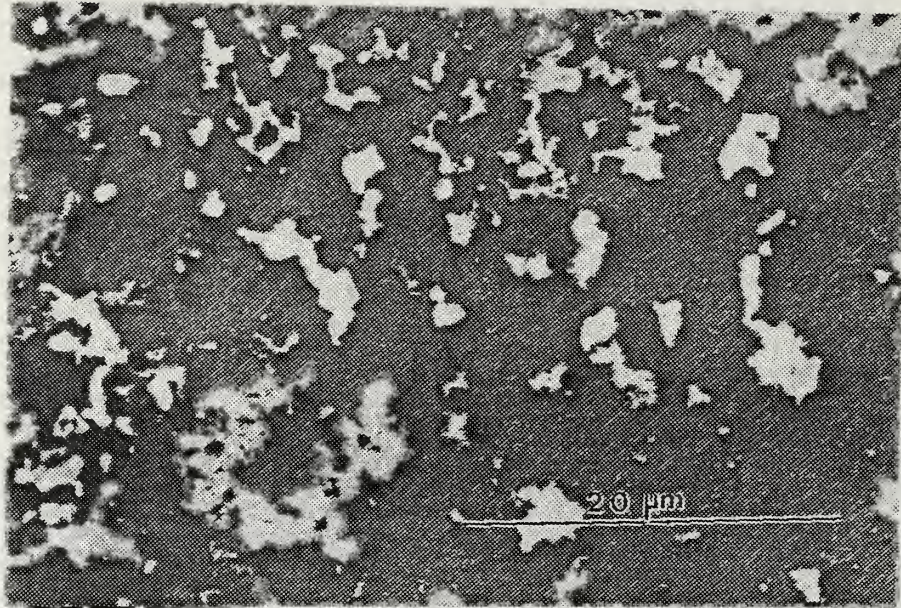


Figure 58. Corroded Surface of Fe-Cr-Al after a 67 Day Exposure at the LaQue Center, 25X

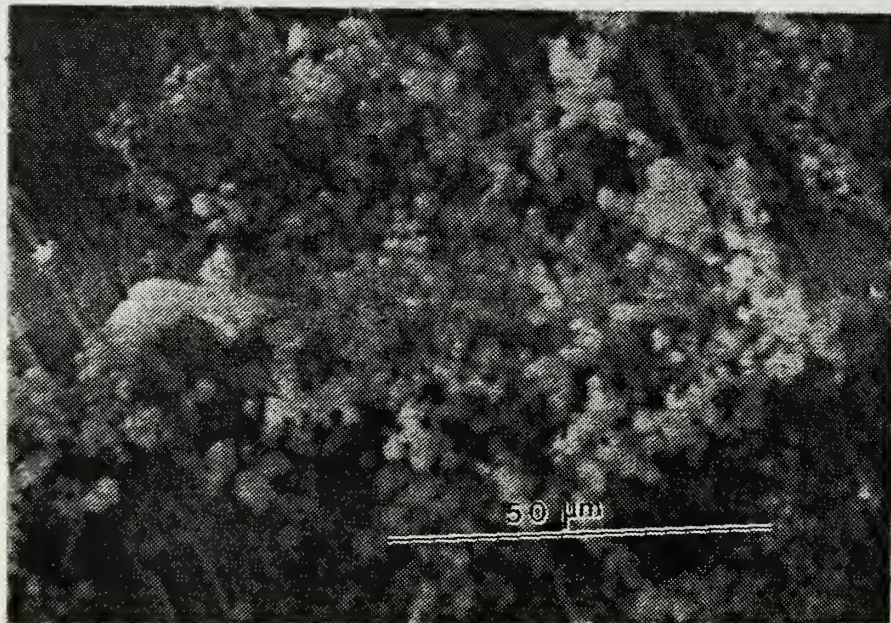


Figure 59. Corroded Surface of Fe-Cr-Al after a 67 Day Exposure at the LaQue Center, 1000X

Sample	Rmpy	Maximum Attack (mils)
1	3.7	30.3 (Pitting)
2	0.9	24.4 (Pitting)
3	<u>3.9</u>	<u>56.3 (Pitting)</u>
AVG	2.83	AVG 37.0

This alloy showed features similar to those experienced by the Fe-Cr-Mo samples. PDP results (Figure 52) were nearly identical to the results for both the 304 stainless steel and Fe-Cr-Mo samples. Microscopic examination of laboratory-exposed samples (Figures 55 and 56) again shows evidence of localized attack, dispersed across the surface of the sample. Seawater exposures (Figures 57-59) were characterized by similar visual appearances as that shown by the Fe-Cr-Mo specimens, that is, gross corrosion products outcropping from the surrounding layered surface. This alloy was extremely vulnerable to pitting and localized film breakdown. This trait, augmented by the development of an adverse area effect, lead to extreme attack patterns.

G. CU-MN-AL-FE-NI

Laboratory polarization results for samples of a high damping Cu-Mn-based alloy (SONOSTON: Cu-Mn-Al-Fe-Ni) are shown in Figures 60 and 61. Surfaces are shown in Figures 62 to 66. Using the PDP and LPM plots, Methods 1-5 yield the following results: (I_p , I_q , and i_{corr} in $\mu A/cm^2$)

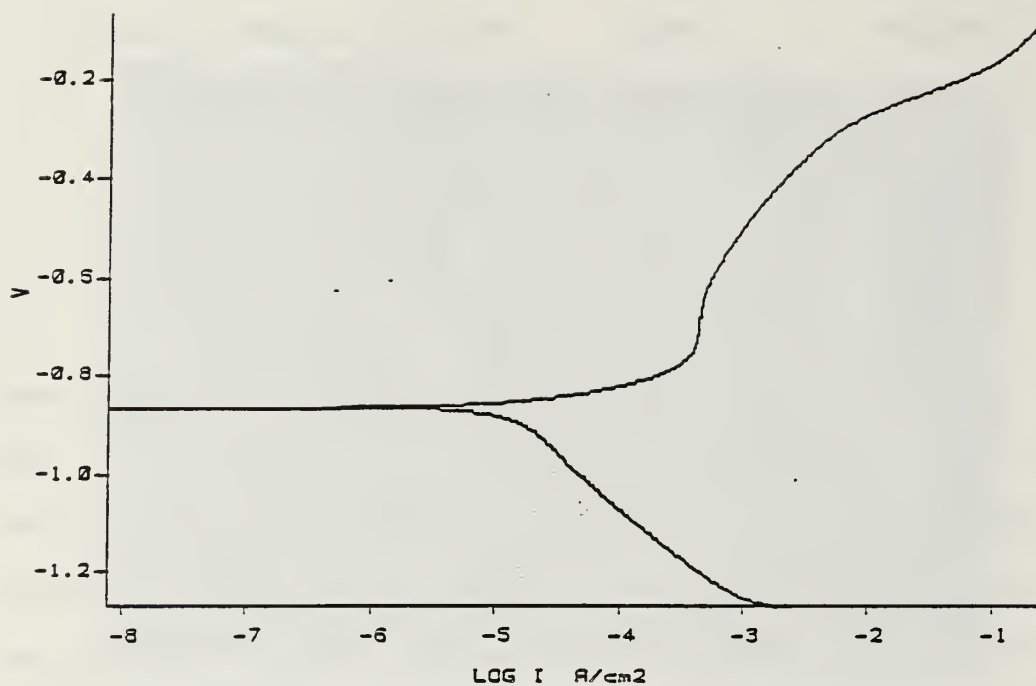


Figure 60. Potentiodynamic Polarization Plot for Cu-Mn-Al-Fe-Ni in Synthetic Seawater

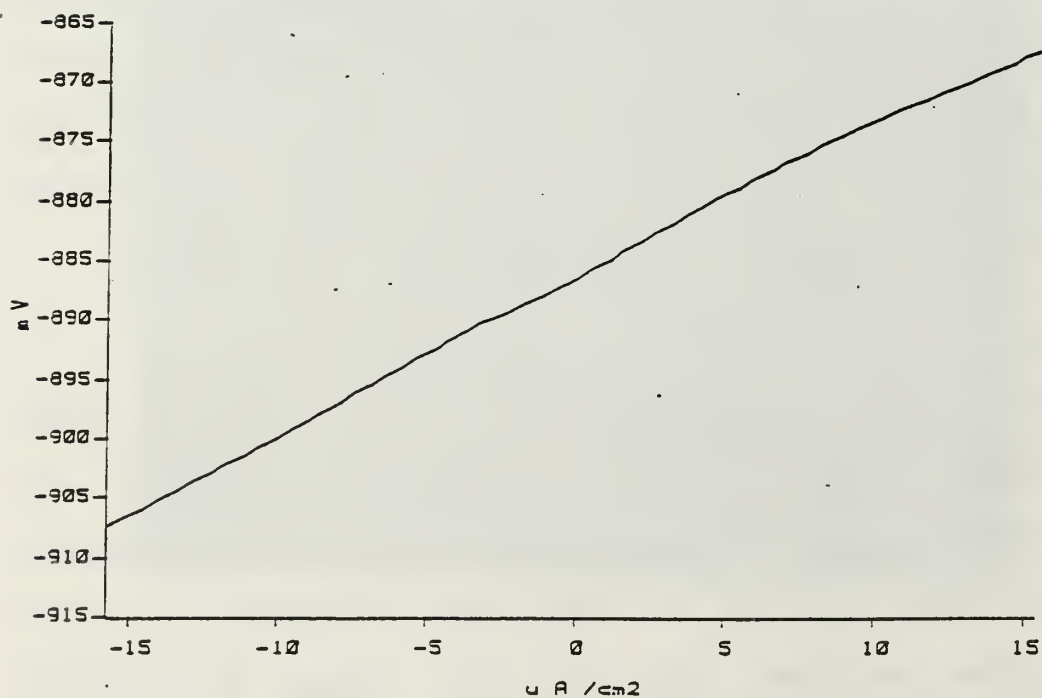


Figure 61. Polarization Resistance Plot for Cu-Mn-Al-Fe-Ni in Synthetic Seawater

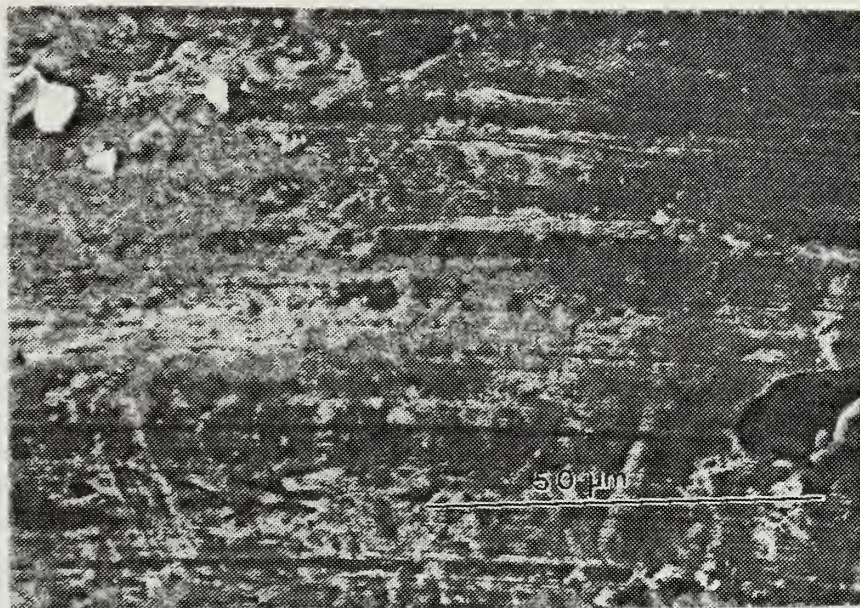


Figure 62. As-Machined Surface of Cu-Mn-Al-Fe-Ni Prior to Corrosion Experimentation, 1000X

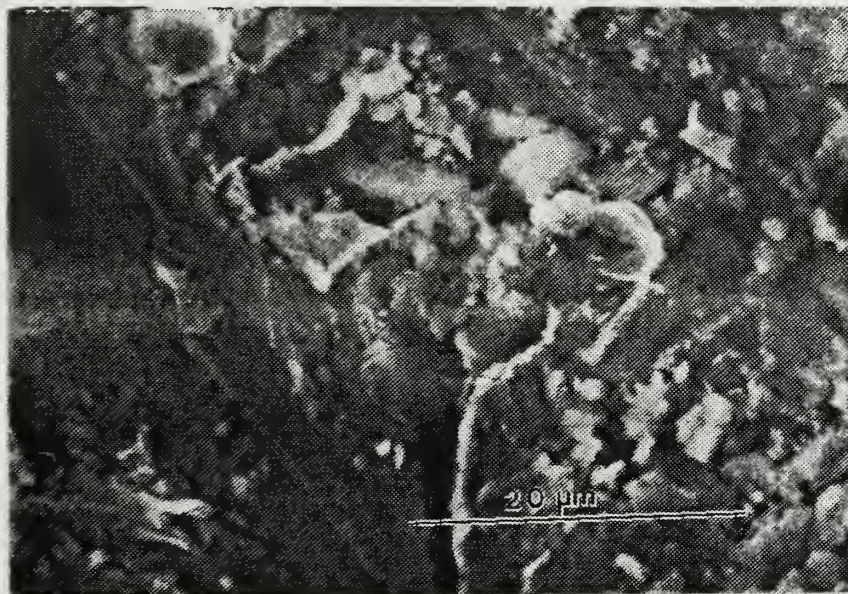


Figure 63. Corrosion Product on Cu-Mn-Al-Fe-Ni after Polarization Experimentation, 2000X

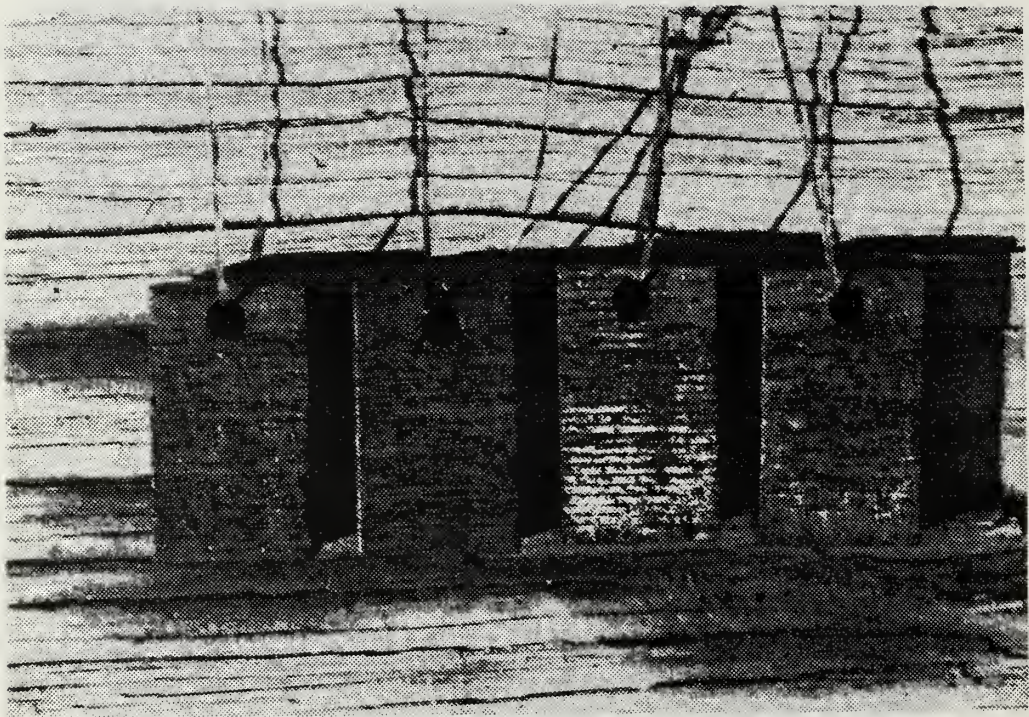


Figure 64. Cu-Mn-Al-Fe-Ni Samples after Removal from Exposure Troughs at the LaQue Center Following an Exposure Period of 67 Days



Figure 65. Corroded Surface of Cu-Mn-Al-Fe-Ni after a 67 Day Exposure at the LaQue Center, 25X

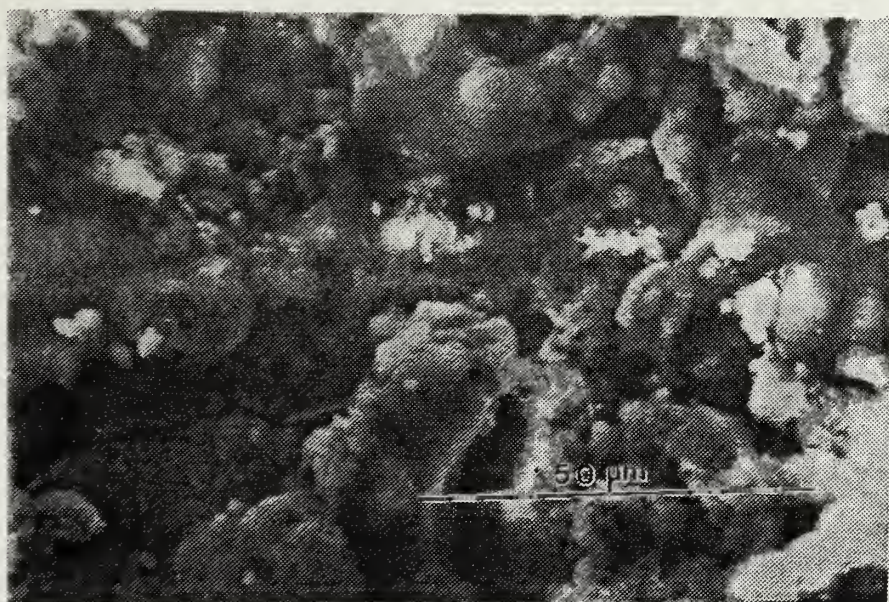


Figure 66. Corroded Surface of Cu-Mn-Al-Fe-Ni after a 67 Day Exposure at the LaQue Center, 1000X

Method	β_a	β_c	I_q	I_p	i_{corr}	Rmpy
1	0.048	0.120	-	-	8.054	4.070
2	0.048	0.120	-	-	10.400	5.260
3	-	-	-	-	-	-
4	0.100	0.100	-	-	8.260	4.174
5	0.100	0.100	-	-	15.200	<u>7.680</u>
AVG						5.296

Direct weight loss results from seawater exposure are:

Sample	Rmpy	Maximum Attack (mils)
1	3.4	< 0.5 (General)
2	2.7	< 0.5 (General)
3	<u>2.8</u>	<u>< 0.5 (General)</u>
AVG	2.97	AVG < 0.5

Agreement between corrosion rates calculated for synthetic and natural seawater exposures is quite good. SEM photography performed on the corroded specimens (Figures 63, 65, and 66) indicated film formation, concurring with the PDP plot. This alloy experienced uniform attack as shown in Figures 64 to 66. Outcropping corrosion products are again seen in Figure 65.

H. CU-MN-AL

Experimental polarization results for the other Cu-Mn-based alloy studied (INCRAMUTE: Cu-Mn-Al) are presented in Figures 67 and 68. Microscopic observations are seen in

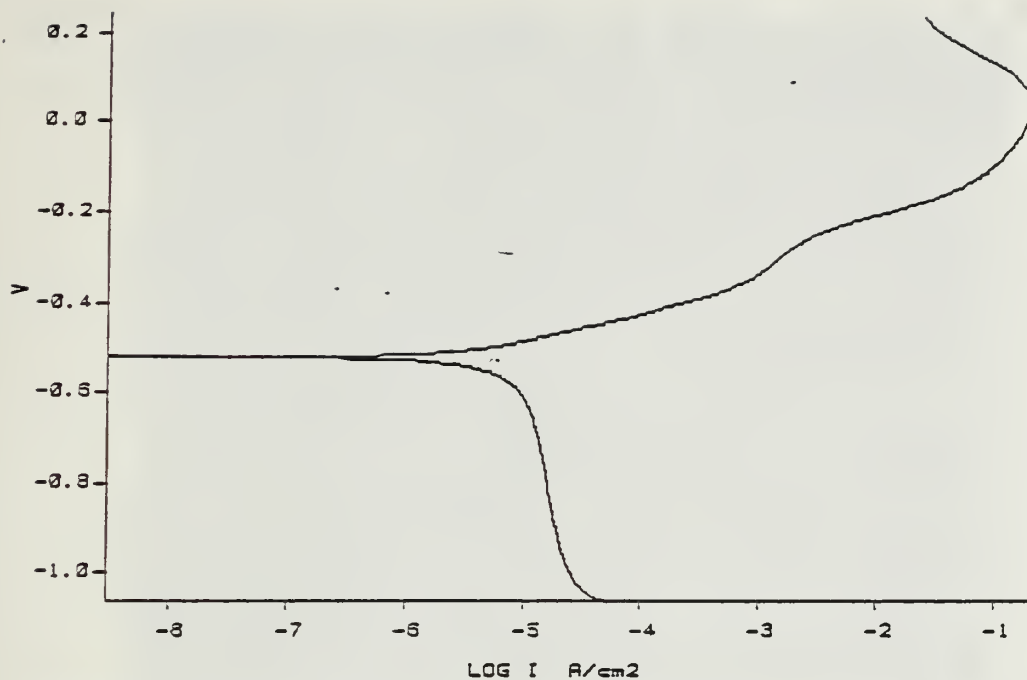


Figure 67. Potentiodynamic Polarization Plot for Cu-Mn-Al in Synthetic Seawater

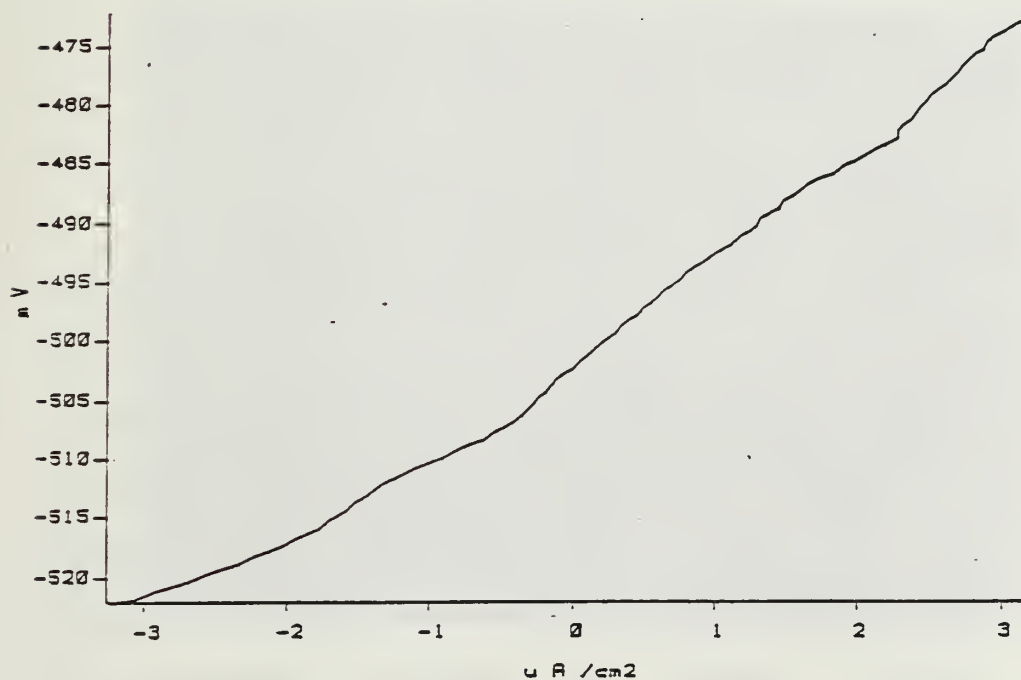


Figure 68. Polarization Resistance Plot for Cu-Mn-Al in Synthetic Seawater

in Figures 69 to 73. Using the PDP and LPM plots, Methods 1-5 yield the following results: (I_p , I_q , and i_{corr} in $\mu A/cm^2$)

Method	β_a	β_c	I_q	I_p	i_{corr}	R_{mpy}
1	0.035	0.045	-	-	1.119	0.595
2	0.035	0.045	-	-	1.900	0.483
3	-	-	-	-	-	-
4	0.100	0.100	-	-	1.718	0.383
5	0.100	0.100	-	-	2.270	<u>1.220</u>
AVG						0.670

Direct weight loss results from seawater exposure are:

Sample	R_{mpy}	Maximum Attack (mils)
1	3.7	3.1 (Pitting)
2	3.5	2.0 (Pitting)
3	<u>3.6</u>	<u>2.4 (Pitting)</u>
AVG	3.50	AVG 2.5

Agreement between laboratory and natural seawater exposures was fair. Even though the Cu-Mn-Al samples had a significantly lower corrosion rate than that experienced by the previously discussed Cu-Mn-Al-based samples, this alloy experienced slight pitting. Specimens photographed immediately after removal from the seawater exposure troughs (Figure 71) showed regions of shallow pitting. An

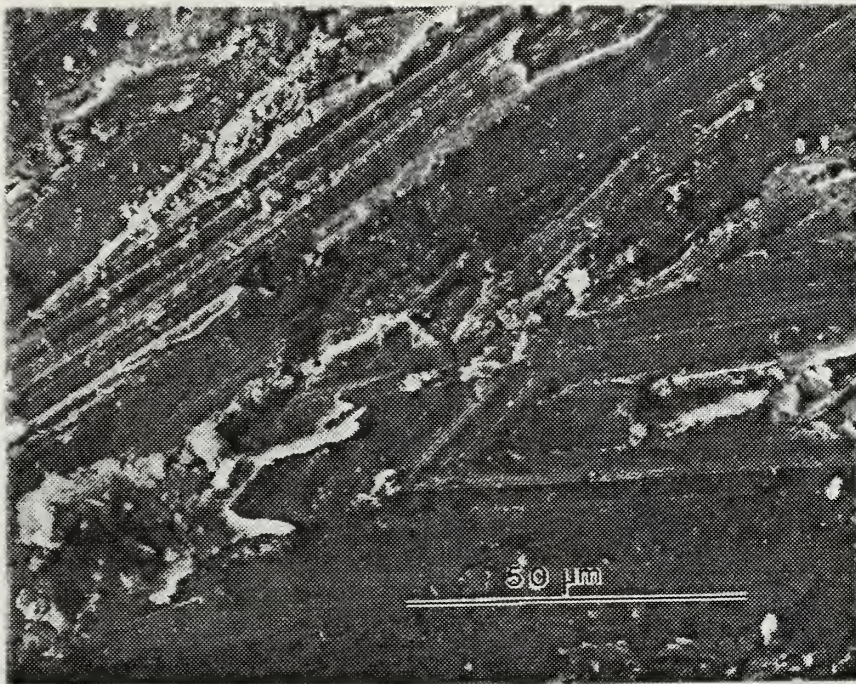


Figure 69. As-Machined Surface of Cu-Mn-Al prior to Corrosion Experimentation, 1000X

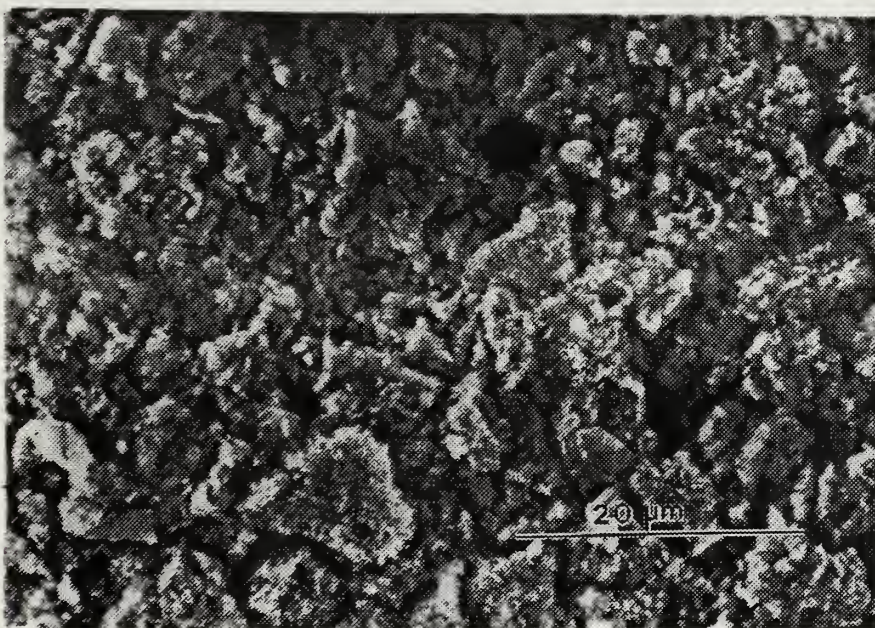


Figure 70. Corrosion Product on Cu-Mn-Al after Polarization Experimentation, 1900X

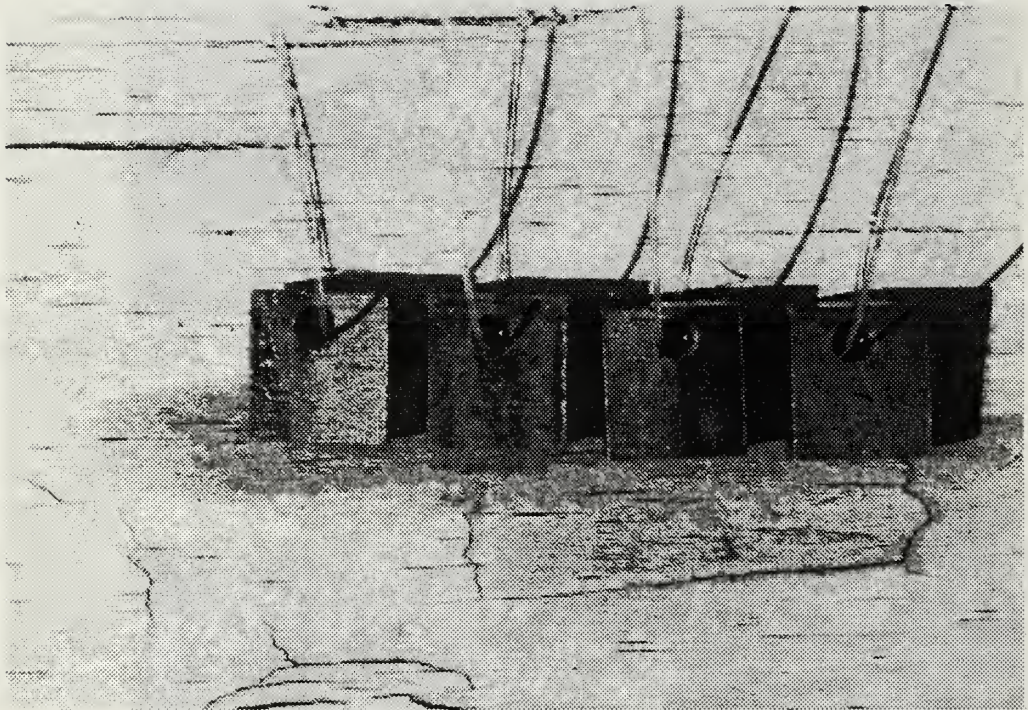


Figure 71. Cu-Mn-Al Samples after Removal from Exposure Troughs at the LaQue Center Following an Exposure Period of 67 Days



Figure 72. Corroded Surface of Cu-Mn-Al after a 67 Day Exposure at the LaQue Center, 25X

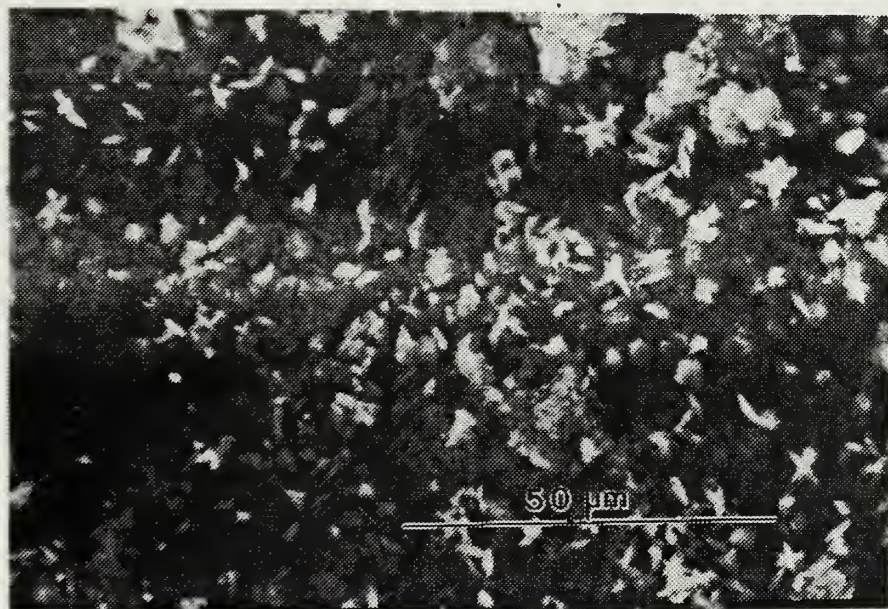


Figure 73. Corroded Surface of Cu-Mn-Al after a 67 Day Exposure at the LaQue Center, 1000X

outcropping of corrosion products from the surrounding film is again seen in Figures 72 and 73.

I. CU-ZN-AL

Laboratory polarization curves for the high damping (and shape-memory-capable) Cu-Zn-Al alloy are shown in Figures 74 and 75, surfaces in Figures 76 to 80. Using the PDP plot and the LPM plot, Methods 1-5 yield the following results:

(I_p , I_q , and i_{corr} in $\mu A/cm^2$)

Method	β_a	β_c	I_q	I_p	i_{corr}	R_{mpy}
1	0.062	0.075	-	-	1.897	0.963
2	0.062	0.075	-	-	3.230	1.640
3	-	-	-	-	-	-
4	0.100	0.100	-	-	3.069	1.558
5	0.100	0.100	-	-	4.770	<u>2.420</u>
AVG						1.645

Direct weight loss results from seawater exposure are:

Sample	R_{mpy}	Maximum Attack (mils)
1	0.5	1.2 (Pitting)
2	0.5	1.6 (Pitting)
3	<u>0.5</u>	<u>1.2 (Pitting)</u>
AVG	0.50	AVG 1.33

The results for laboratory and seawater exposures were in fairly close agreement. The PDP plot indicated a classic region of passivation. However, this passive region is

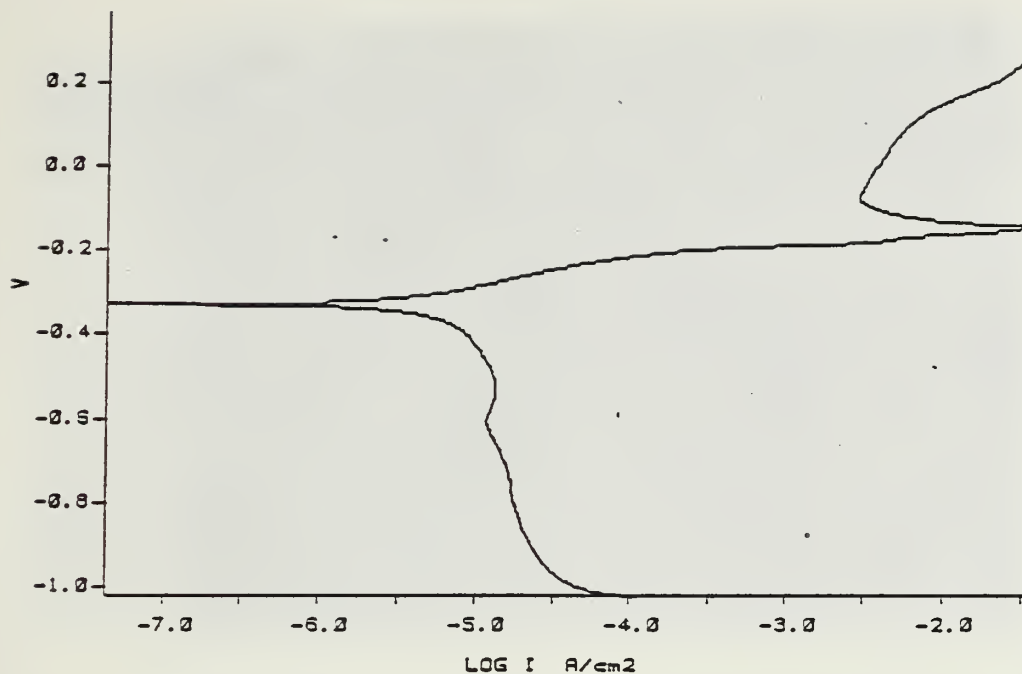


Figure 74. Potentiodynamic Polarization Plot for Cu-Zn-Al in Synthetic Seawater

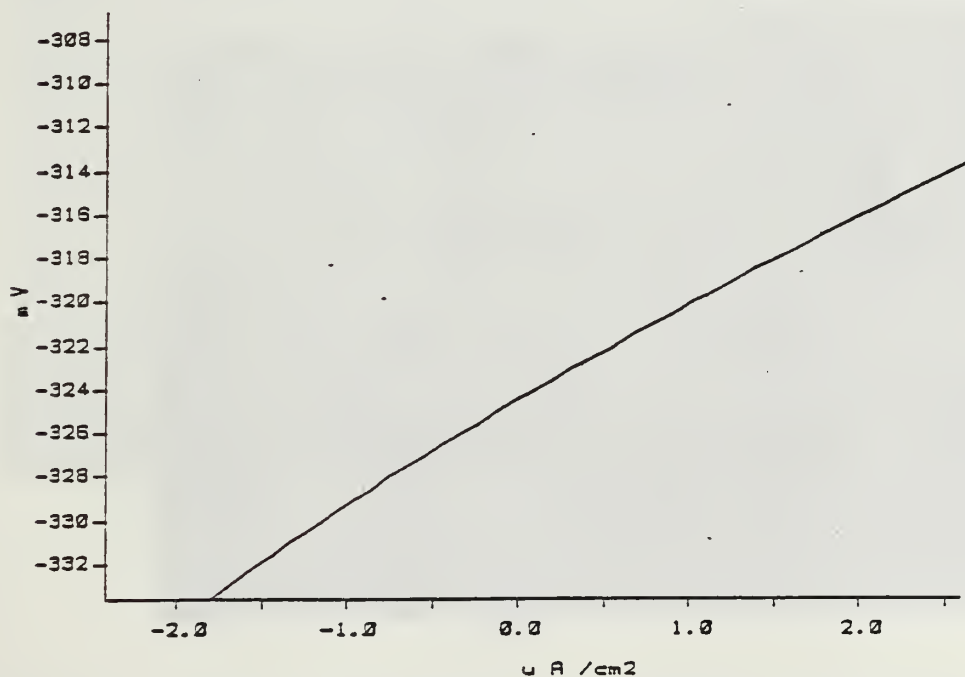


Figure 75. Polarization Resistance Plot for Cu-Zn-Al in Synthetic Seawater

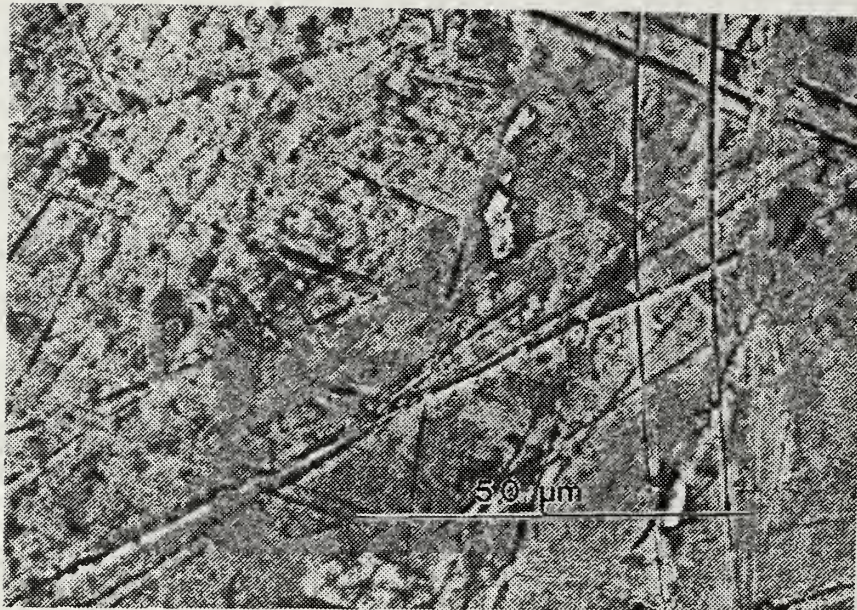


Figure 76. As-Machined Surface of Cu-Zn-Al Prior to Corrosion Experimentation, 1000X

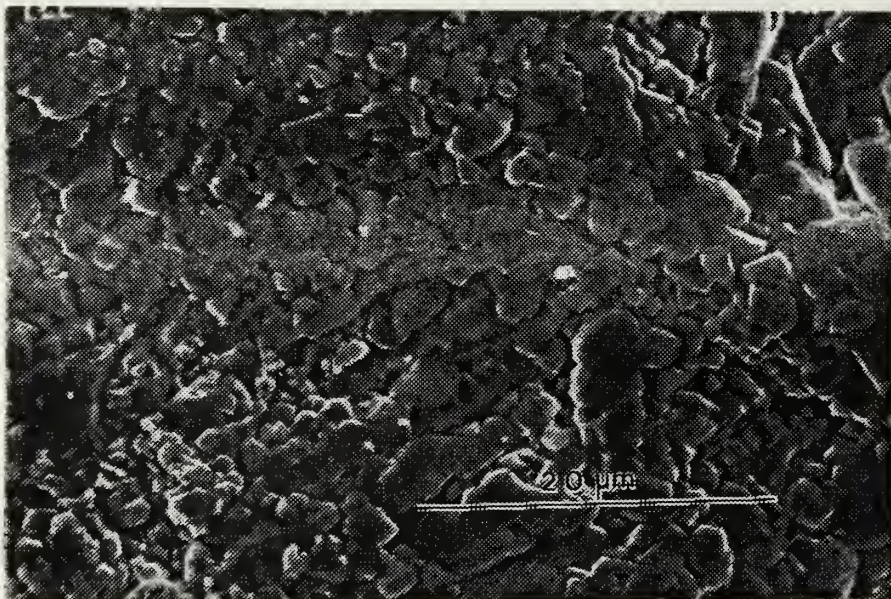
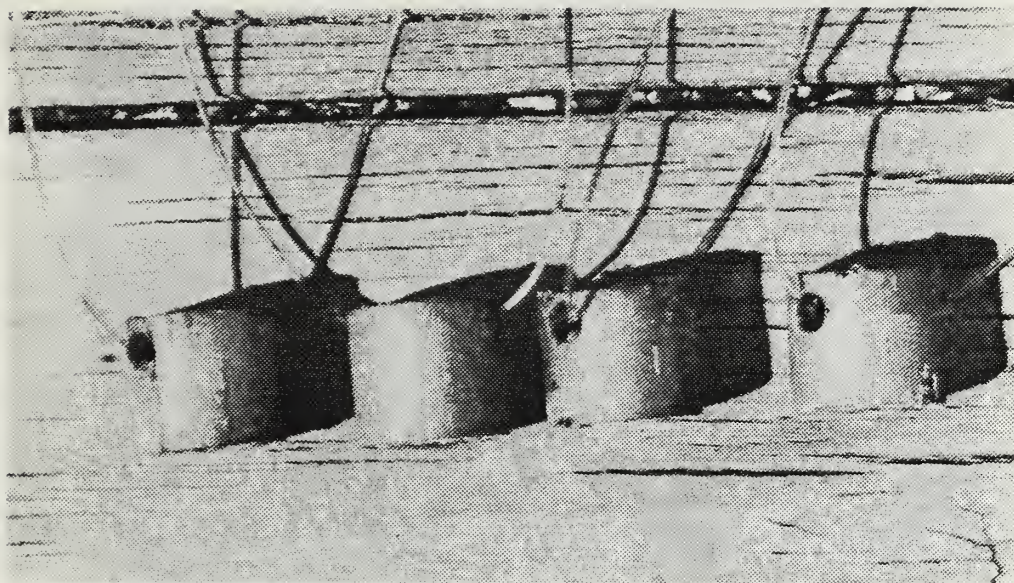
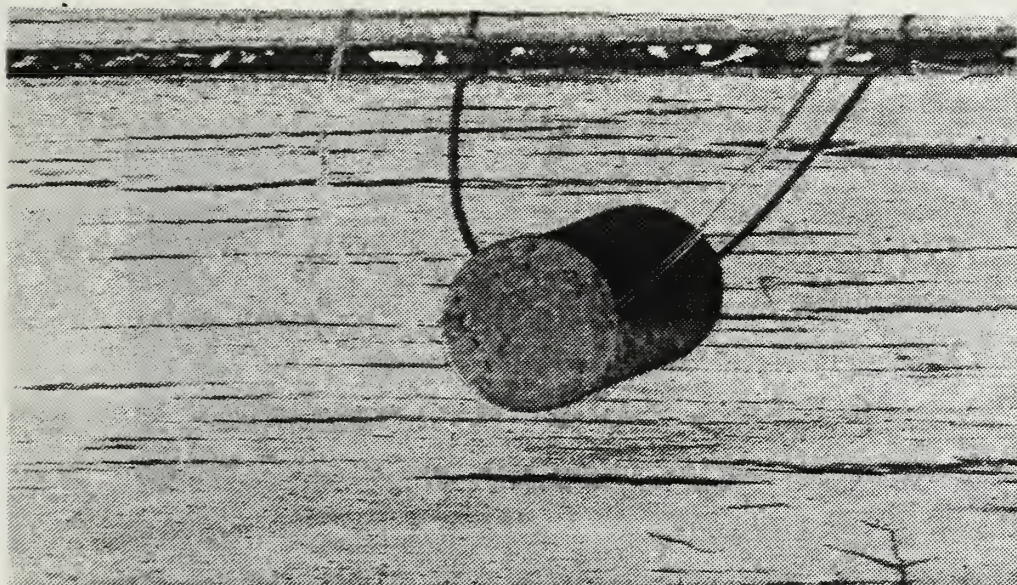


Figure 77. Corrosion Product on Cu-Zn-Al after Polarization Experimentation, 2160X



(a)



(b)

Figure 78. Cu-Zn-Al Samples after Removal from Exposure Troughs at the LaQue Center Following an Exposure Period of 67 Days (a) Side View (b) Top View



Figure 79. Corroded Surface of Cu-Zn-Al after a 67 Day Exposure at the LaQue Center, 12X

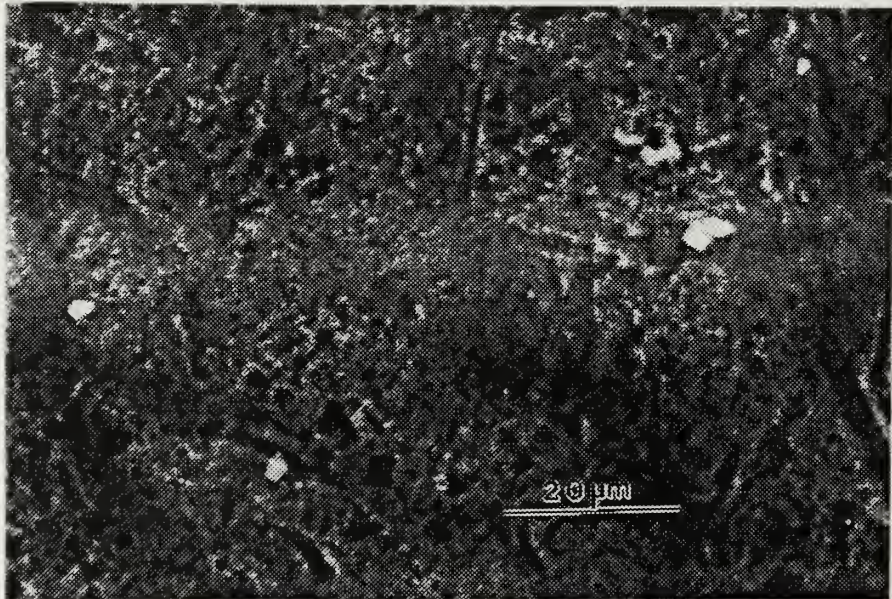


Figure 80. Corroded Surface of Cu-Zn-Al after a 67 Day Exposure at the LaQue Center, 1000X

located at a significantly large value of current density. Laboratory exposures showed a thin film over the surface (Figure 77). This film is relatively unstable, as indicated by the pitting characteristics of this alloy shown in Figure 79.

J. 630 SERIES BRONZE

The polarization results for samples of a 630 Series bronze are shown in Figures 81 and 82, surface exposures in Figures 83 to 87. Using the PDP and the LPM plots, Methods 1-5 yield the following results: (I_p , I_q , and i_{corr} in $\mu A/cm^2$)

Method	β_a	β_c	I_q	I_p	i_{corr}	R_{mpy}
1	0.031	0.041	-	-	1.442	0.737
2	0.031	0.041	-	-	4.690	2.420
3	-	-	-	-	-	-
4	0.100	0.100	-	-	3.177	1.640
5	0.100	0.100	-	-	13.400	<u>6.930</u>
					AVG	2.932

Direct weight loss results from seawater exposure are:

Sample	R_{mpy}	Maximum Attack (mils)
1	0.4	< 0.5 (General)
2	0.4	< 0.5 (General)
3	<u>0.4</u>	<u>< 0.5 (General)</u>
AVG	0.40	AVG < 0.5

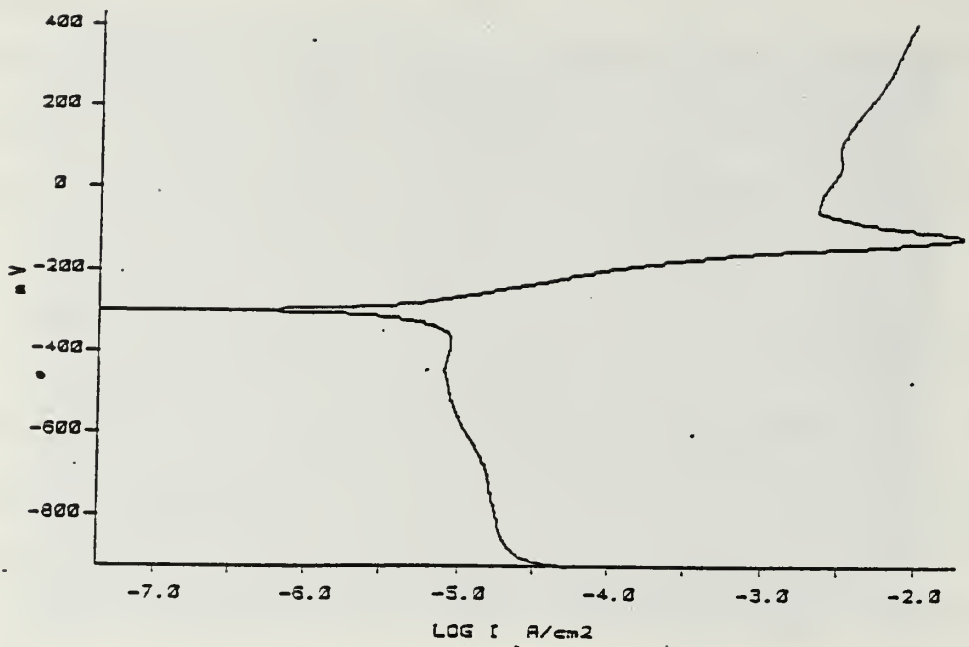


Figure 81. Potentiodynamic Polarization Plot for 630 Series Bronze in Synthetic Seawater

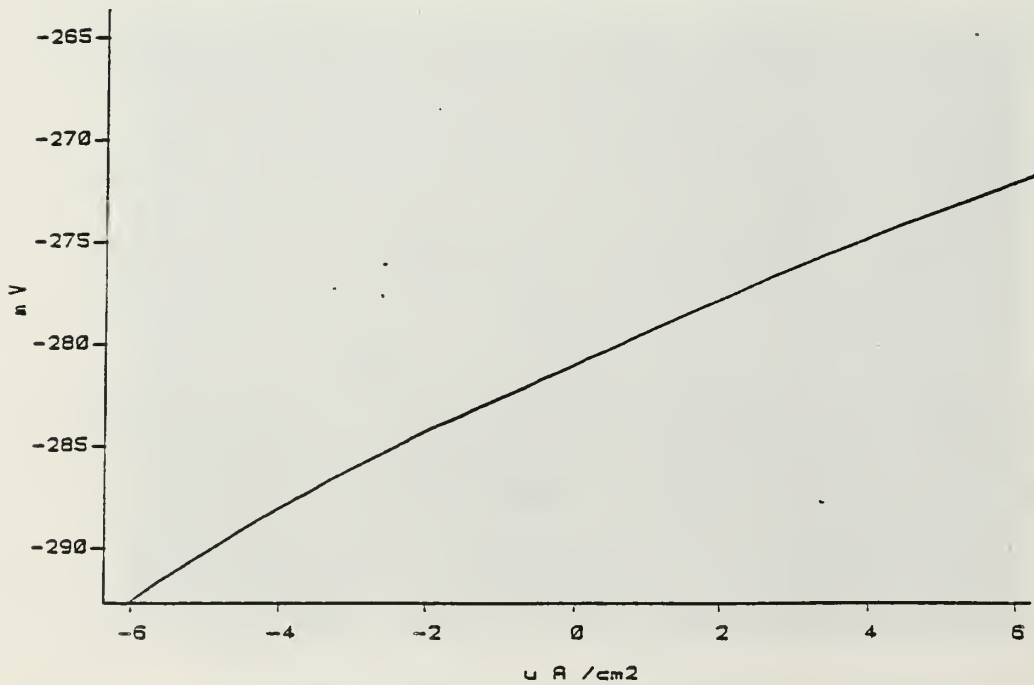


Figure 82. Polarization Resistance Plot for 630 Series Bronze in Synthetic Seawater

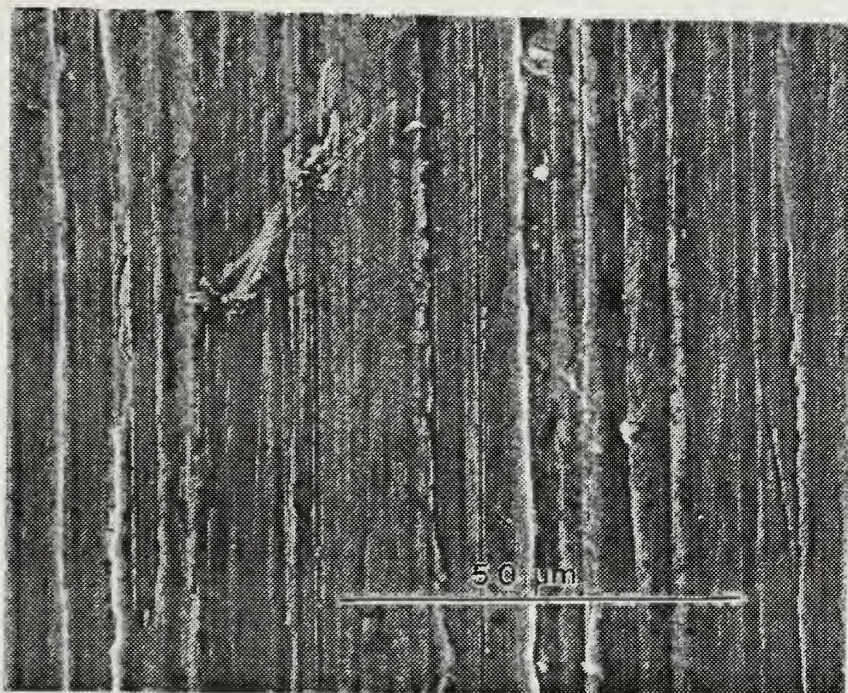


Figure 83. As-Machined Surface of 630 Series Bronze Prior to Corrosion Experimentation, 1000X

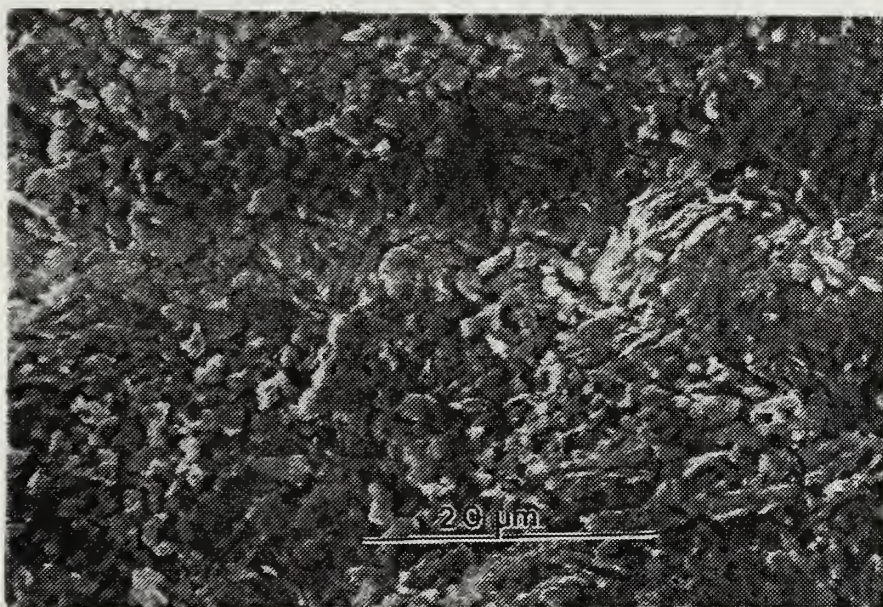


Figure 84. Corrosion Product on 630 Series Bronze after Polarization Experimentation, 2000X

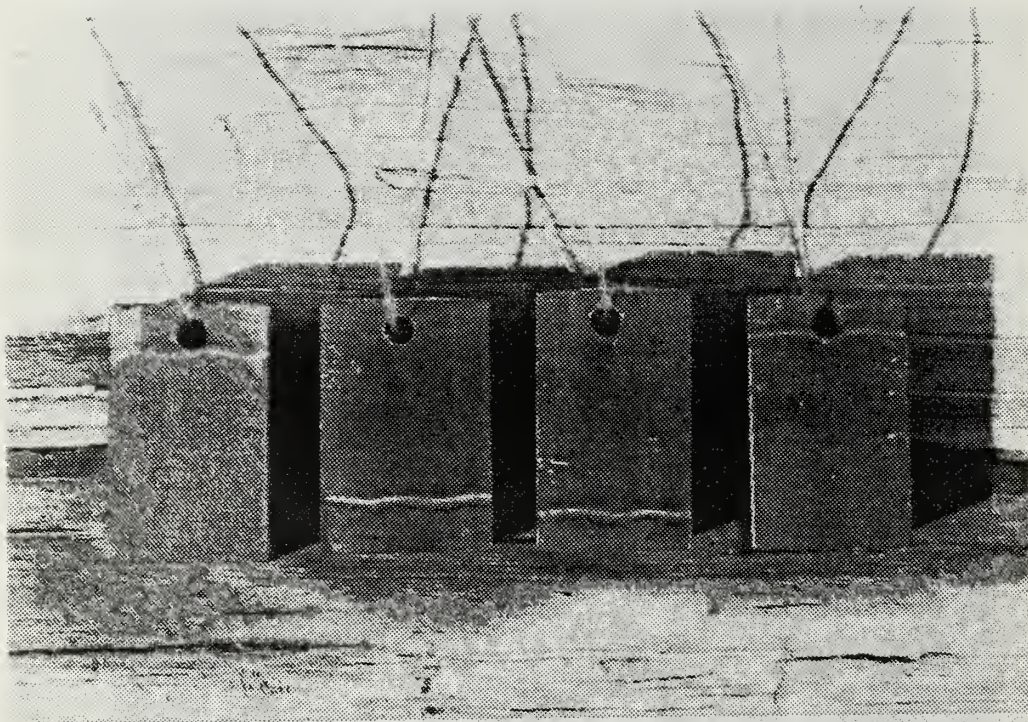


Figure 85. 630 Series Bronze Samples after Removal from Exposure Troughs at the LaQue Center Following an Exposure Period of 67 Days

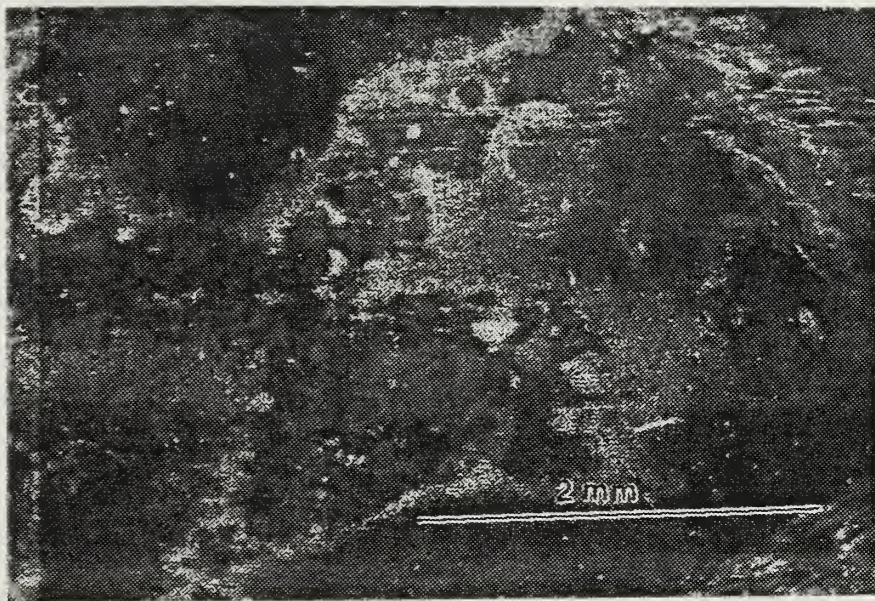


Figure 86. Corroded Surface of 630 Series Bronze after a 67 Day Exposure at the LaQue Center, 25X

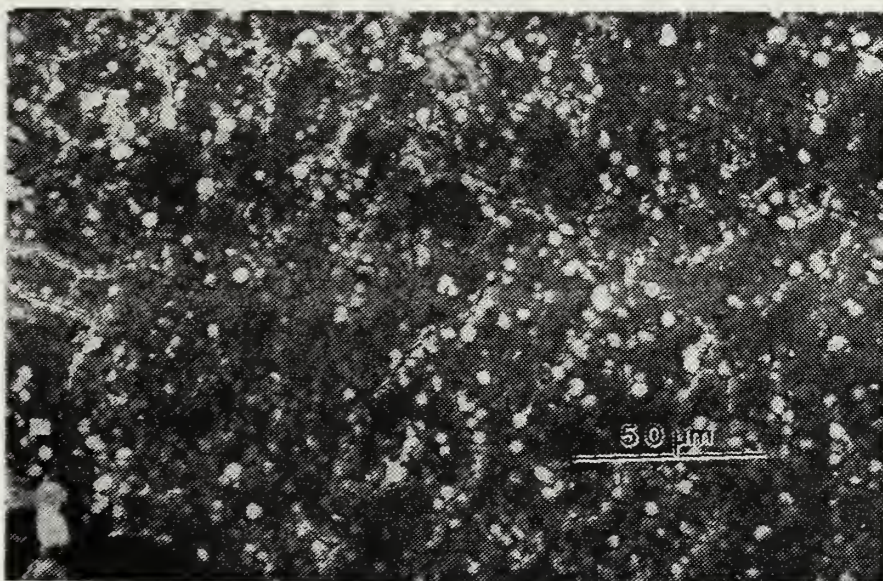


Figure 87. Corroded Surface of 630 Series Bronze after a 67 Day Exposure at the LaQue Center, 560X

Results from the polarization experimentation and sea exposures showed poor agreement. The uniformly distributed passive film shown in Figures 84 and 85 confirmed the potentiodynamic polarization results. Even though the 630 Series bronze alloy is also a Cu-Zn-Al-based alloy, general corrosion, vice pitting, was experienced by the samples exposed at the LaQue Center. However, visual inspection revealed that the film was very thin; machining patterns were still visible. Continued immersion of the 630 Series bronze specimens should show development of a significantly deeper film.

K. COMPARISON OF AVERAGE CORROSION RATE RESULTS FOR LABORATORY AND SEAWATER EXPOSURES

The data on page 107 gives a comparison between corrosion rates of samples polarized in synthetic seawater and exposed in a natural seawater environment:

When these data are scrutinized, it is obvious that in certain cases the agreement between laboratory and seawater is not that good. For example, a comparison of the average laboratory and sea exposure corrosion rates is extremely poor for the 7075 aluminum alloy (factor of 10 different). This can be rationalized, however, on the basis that the laboratory exposure does not allow sufficient time for the prevalent pitting mode of attack to fully manifest itself. Since, in the sea exposures, the 7075 aluminum was characterized by severe pitting and a buildup of corrosion

Alloy	Rmpy (Lab)	Rmpy (LaQue)	Maximum Attack in mils (LaQue)
Ti-Ni	1.348	< 0.10	0.0
1020 C Steel	5.226	3.47	1.57 (General)
7075 Aluminum	0.345	4.27	15.87 (Pitting)
304 Stainless Steel	0.387	< 0.10	0.00
Fe-Cr-Mo	0.633	2.50	55.70 (Pitting)
Fe-Cr-Al	0.422	2.83	37.00 (Pitting)
Cu-Mn-Al- Fe-Ni	5.296	2.97	< 0.50 (General)
Cu-Mn-Al	0.670	3.50	2.50 (Pitting)
Cu-Zn-Al	1.645	0.50	1.33 (Pitting)
630 Series Bronze	2.932	0.40	< 0.50 (General)

products, the direct weight loss calculations take the significant loss of metal in these corrosion products into account, whereas during the laboratory measurements, the pitting process has barely begun. Thus the laboratory results reflect, and the LaQue results do not reflect, a true general corrosion rate.

A similar argument can be applied for the Fe-Cr-based alloys and the Cu-Mn-Al (INCRAMUTE) alloy. The agreement between corrosion rates for the Fe-Cr-based alloys is fair. Again, the massive loss of corrosion products due to localized attack influences the direct weight loss calculations. The general corrosion rate calculated for

these samples based on laboratory data is significantly lower than that measured at the LaQue Center.

The Cu-Mn-Al alloy also showed fair agreement between laboratory and natural seawater corrosion rates, and once again, pitting attack of this alloy contributes to a higher seawater exposure corrosion rate than is realized in the shorter laboratory exposures.

Comparison of the corrosion rates for 630 Series bronze samples shows a significantly higher corrosion rate for the laboratory exposures than the seawater exposures. In this case, the laboratory experiments do not accurately reflect the effectiveness of the passivating film, which requires time to develop. Seawater exposures of 67 days show that the time of exposure is critical for allowing full development of the film.

L. GALVANIC SERIES OF SELECTED HIGH DAMPING AND BASELINE ALLOYS IN QUIESCENT SYNTHETIC SEAWATER

ALLOY	STEADY STATE ELECTRODE POTENTIAL VS SCE (V)
630 Series Bronze	-.297
Cu-Zn-Al	-.321
Titanium-Nickel	-.415
Fe-Cr-Mo	-.462
304 Stainless Steel	-.475
Fe-Cr-Al	-.476
Cu-Mn-Al	-.515
1020 Carbon Steel	-.713
Cu-Mn-Al-Fe-Ni	-.858
7075 Aluminum	-1.067

M. SELECTED GALVANIC COUPLES

The theoretical corrosion rate of the anodic member of a galvanic couple can be estimated using overlays of individual PDP plots. The intercept of the cathodic polarization curve of the more noble member with the anodic polarization curve for the active member will approximate i_{couple} and E_{couple} , the corrosion current density and potential of the galvanic couple.

When two corroding metals are galvanically coupled, the corrosion rate of the more active member will be accelerated, while the more noble member's corrosion rate will become retarded. The corrosion rate of the anodic member will be approximately the rate computed using the value of i_{couple} in Equation (3). However, the corrosion rate of the more noble member can be approximated by extrapolating its anodic polarization curve back to an intercept with E_{couple} . This significantly lower value for current density can again be used to solve for an approximate corrosion rate of the noble member using Equation (3). (Predicted corrosion rates for the anodic member of various galvanic couples are shown in Table I.)

Galvanic couples having active-passive metals can produce unusual results. Coupling of the metals may result in spontaneous passivation or pitting of the more active metal.

TABLE I

THEORETICAL CORROSION RATES EXPECTED FOR THE ANODIC
MEMBER OF SELECTED GALVANIC COUPLES

Anode	Cathode	i_{couple} (A/cm ²)	Rmpy
7075 Al	Cu-Zn-Al	22.39	9.256
7075 Al	Cu-Mn-Al	12.59	5.205
7075 Al	Cu-Mn-Al-Fe-Ni	5.02	2.075
7075 Al	Ti-Ni	95.50	39.480
7075 Al	Fe-Cr-Mo	25.12	10.385
7075 Al	Fe-Cr-Al	39.81	16.458
1020 C Steel	Cu-Zn-Al	14.13	6.611
1020 C Steel	Cu-Mn-Al	79.38	37.138
Cu-Mn-Al- Fe-Ni	1020 C Steel	17.78	8.895
1020 C Steel	Ti-Ni	28.18	13.184
1020 C Steel	Fe-Cr-Mo	11.75	5.497
1020 C Steel	Fe-Cr-Al	29.51	13.806
304 St Steel	Cu-Zn-Al	2.24	1.004
Cu-Mn-Al	304 St Steel	1.26	0.670
Cu-Mn-Al- Fe-Ni	304 St Steel	17.38	8.695
304 St Steel	Ti-Ni	1.17	0.524
304 St Steel	Fe-Cr-Mo	0.28	0.125
Fe-Cr-Al	304 St Steel	0.19	0.088

Overlays of the potentiodynamic polarization plots of 7075 aluminum alloy and selected high damping alloys are shown in Figures 88 to 93. By this method, "coupling" of the Cu-Zn-Al, Ti-Ni, Cu-Mn-Al, Fe-Cr-Mo, Fe-Cr-Al alloys with 7075 aluminum indicates that spontaneous pitting of the aluminum alloy would be expected (Figures 88-90, 92 and 93). On the other hand, graphical coupling of the Cu-Mn-Al-Fe-Ni (SONOSTON) alloy with 7075 aluminum suggests that enhanced general corrosion of the 7075 aluminum would be observed, as shown in Figure 91.

Polarization overlays for high damping alloys and 1020 low-carbon steel are shown in Figures 94 to 99. Except for the Cu-Mn-Al-Fe-Ni alloy, which has a lower potential than the steel, all the overlays indicate an enhanced general corrosion of the 1020 steel when coupled with any of the other high damping alloys. Coupling the Cu-Mn-Al-Fe-Ni (SONOSTON) alloy with 1020 steel would probably lead to enhanced general corrosion of the high damping alloy.

Overlays of the polarization plots of 304 stainless steel with the high damping alloys are shown in Figures 100 to 105. Couples between Cu-Zn-Al, Ti-Ni, Fe-Cr-Mo, and Fe-Cr-Al alloys with 304 stainless steel predict enhanced general corrosion of the stainless steel (Figures 100, 101, 104, and 105), while overlays for both Cu-Mn-based alloys with 304 stainless steel indicate accelerated general corrosion of the high damping alloys (Figures 102 and 103).

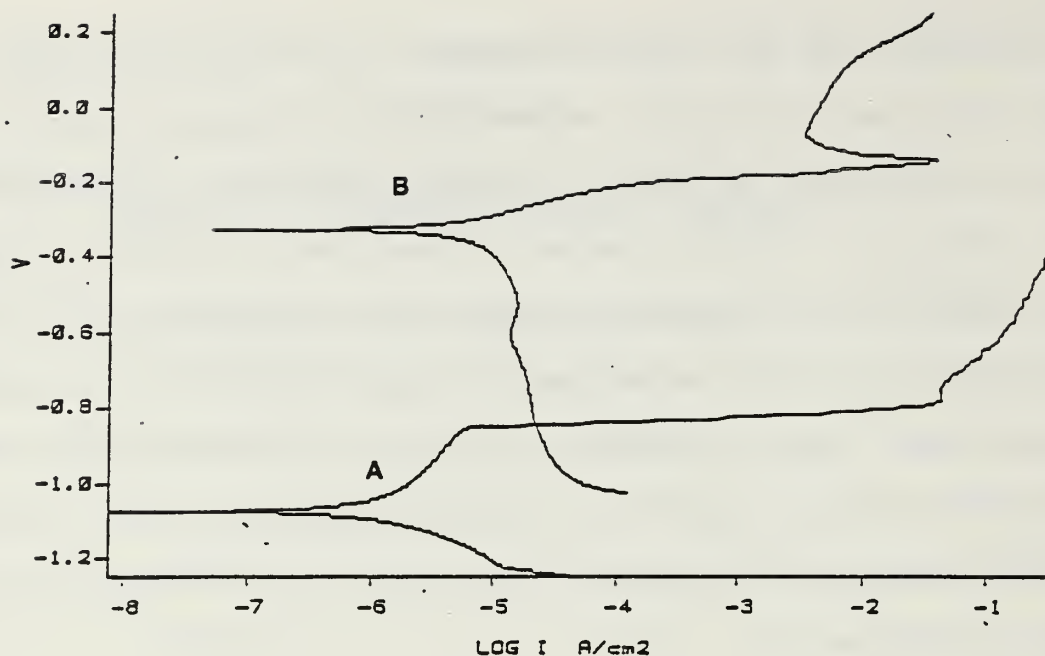


Figure 88. Overlay of Potentiodynamic Plots for 7075 Aluminum (A) and Cu-Zn-Al (B)

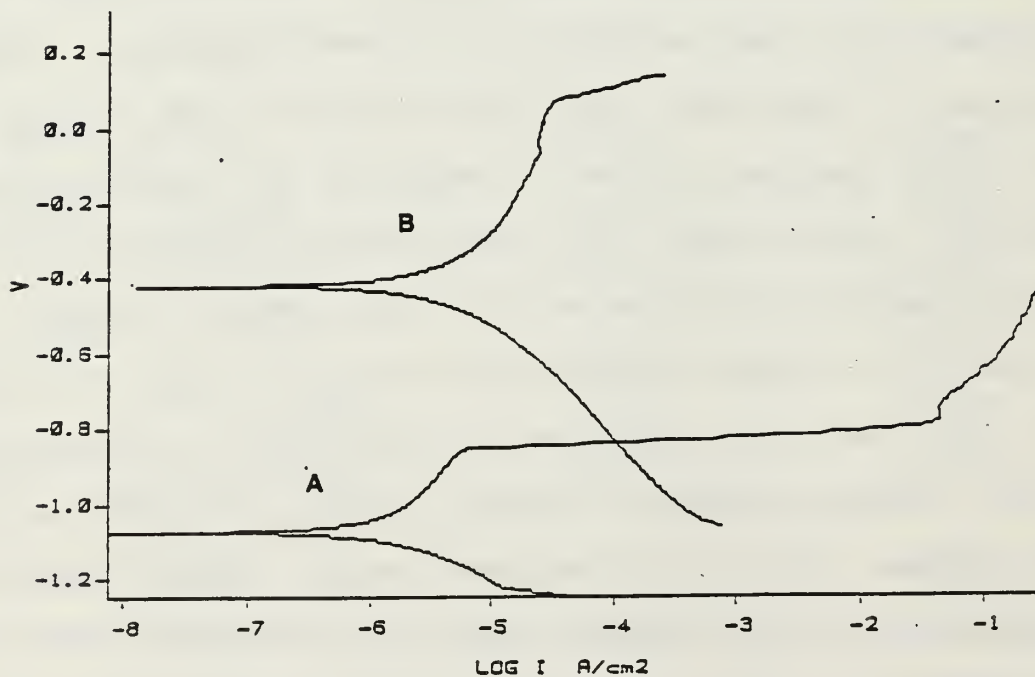


Figure 89. Overlay of Potentiodynamic Plots for 7075 Aluminum (A) and Ti-Ni (B)

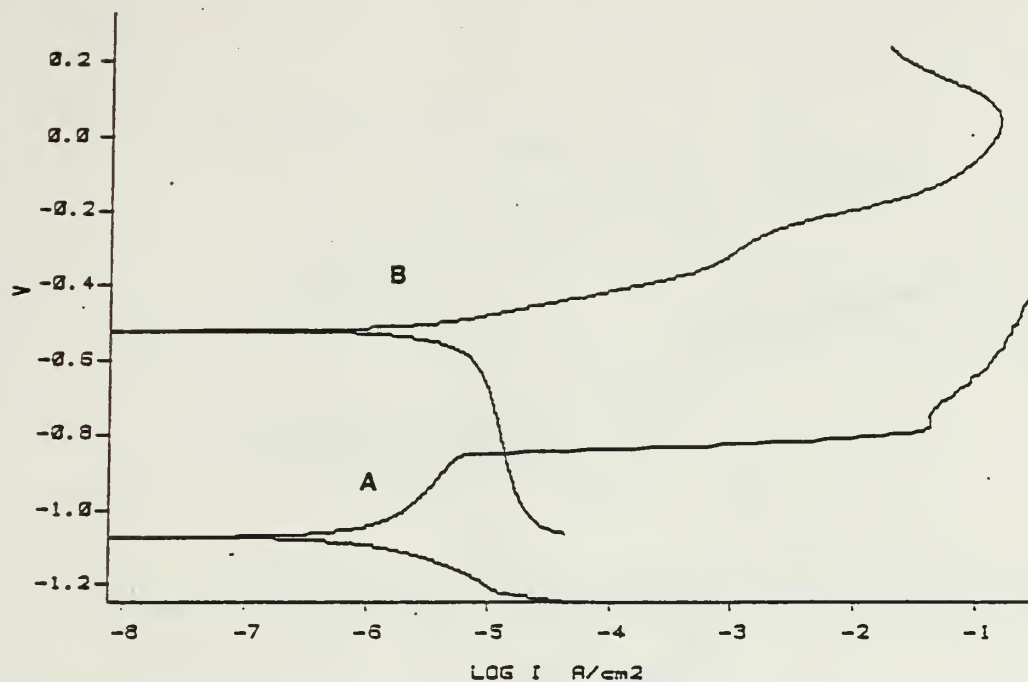


Figure 90. Overlay of Potentiodynamic Plots for 7075 Aluminum (A) and Cu-Mn-Al (B)

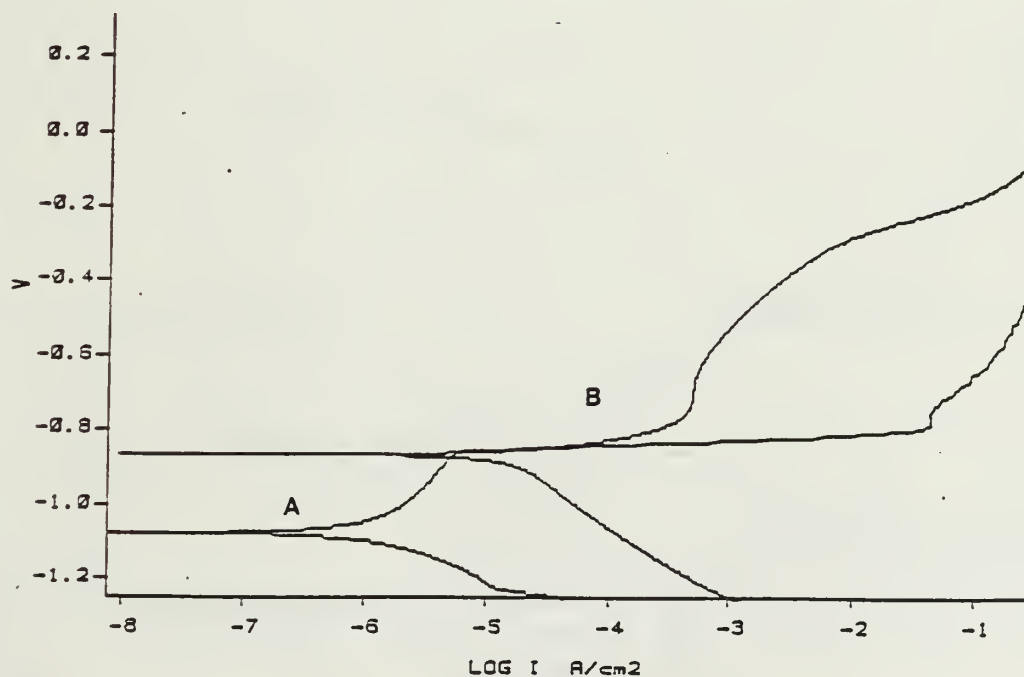


Figure 91. Overlay of Potentiodynamic Plots for 7075 Aluminum (A) and Cu-Mn-Al-Fe-Ni (B)

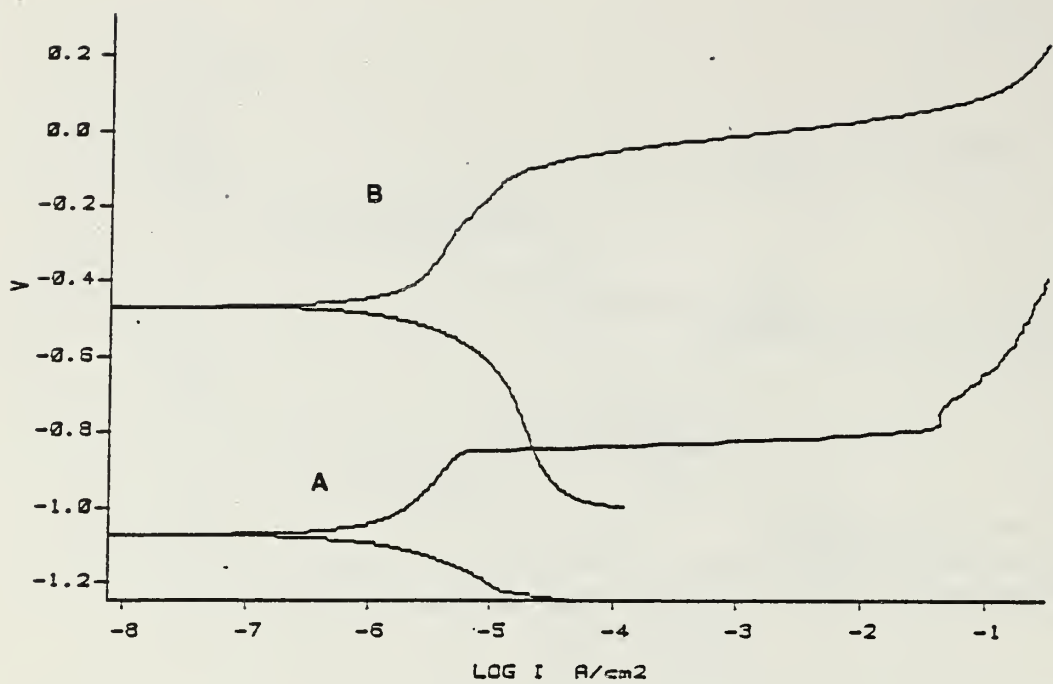


Figure 92. Overlay of Potentiodynamic Plots for 7075 Aluminum (A) and Fe-Cr-Mo (B)

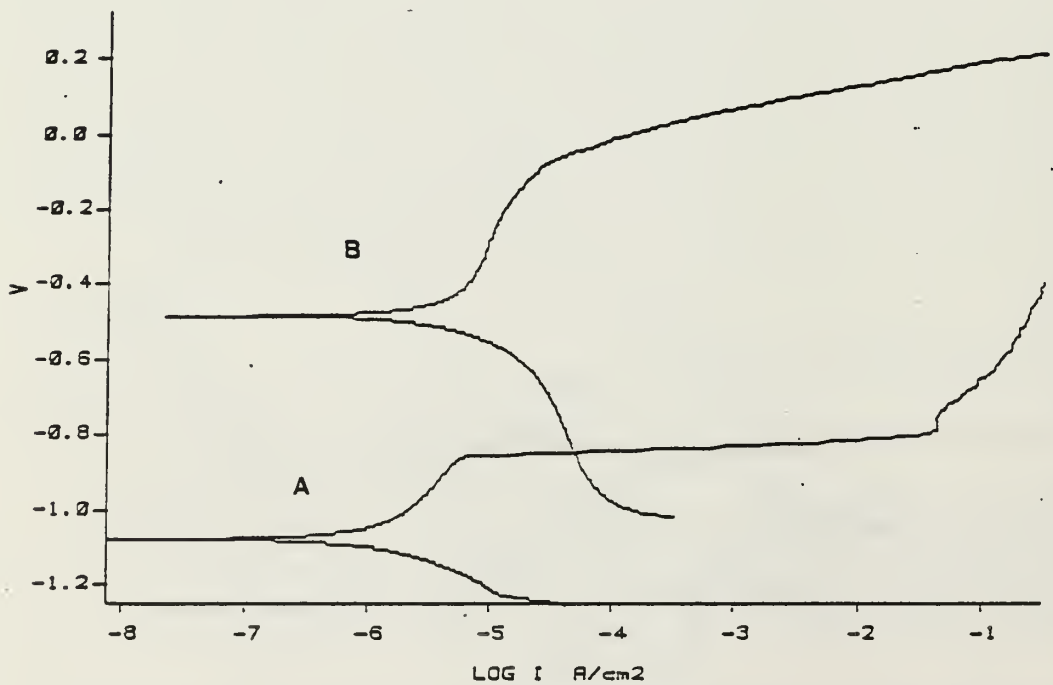


Figure 93. Overlay of Potentiodynamic Plots for 7075 Aluminum (A) and Fe-Cr-Al (B)

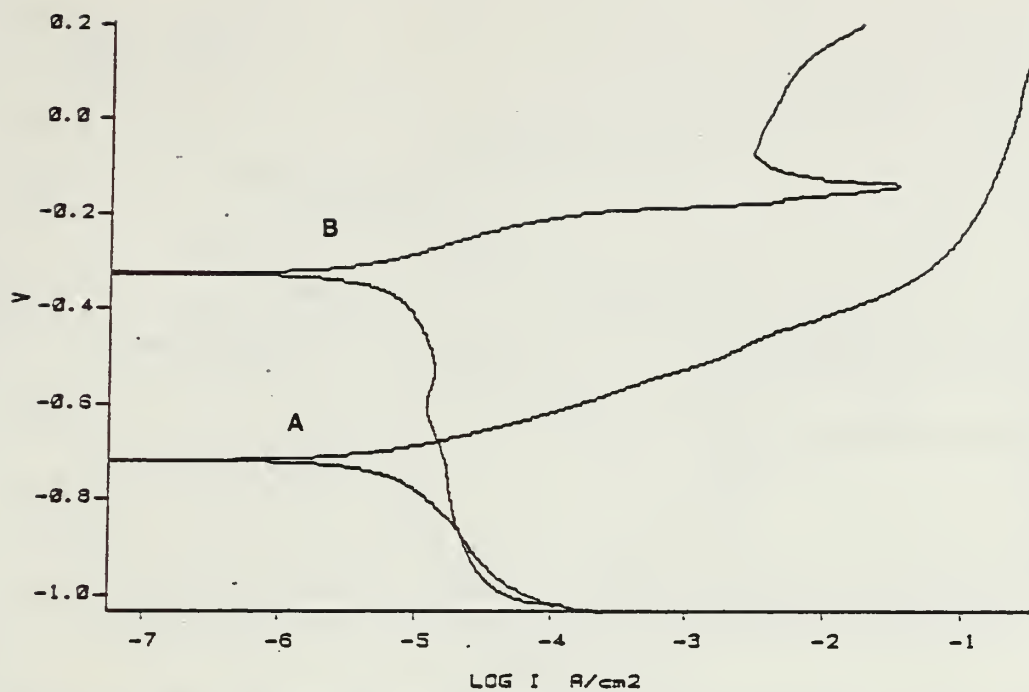


Figure 94. Overlay of Potentiodynamic Plots for 1020 C Steel (A) and Cu-Zn-Al (B)

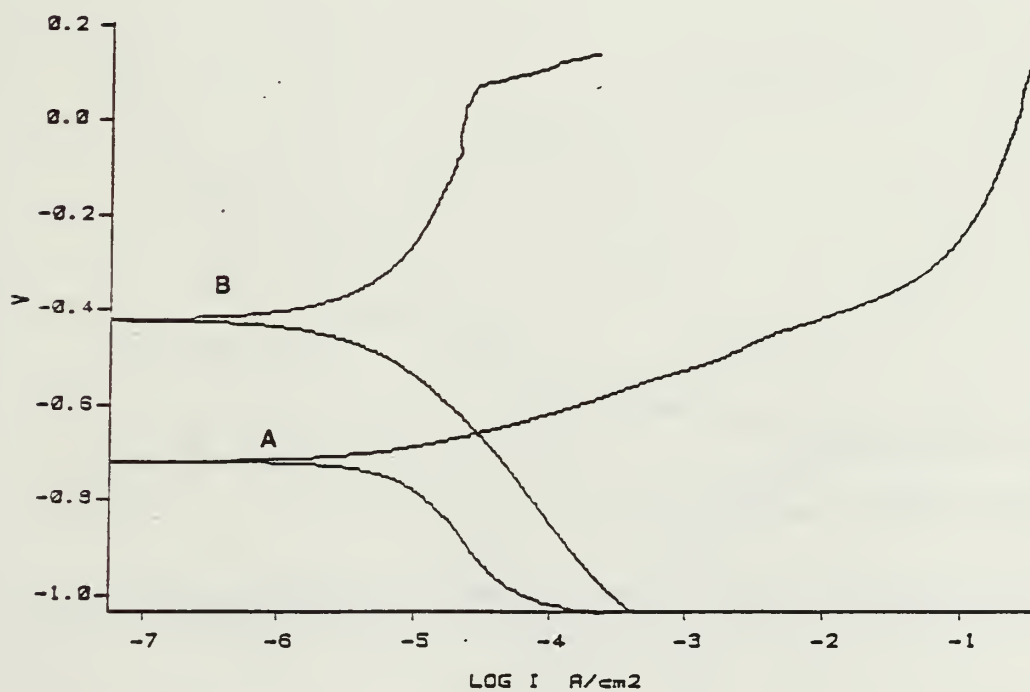


Figure 95. Overlay of Potentiodynamic Plots for 1020 C Steel (A) and Ti-Ni (B)

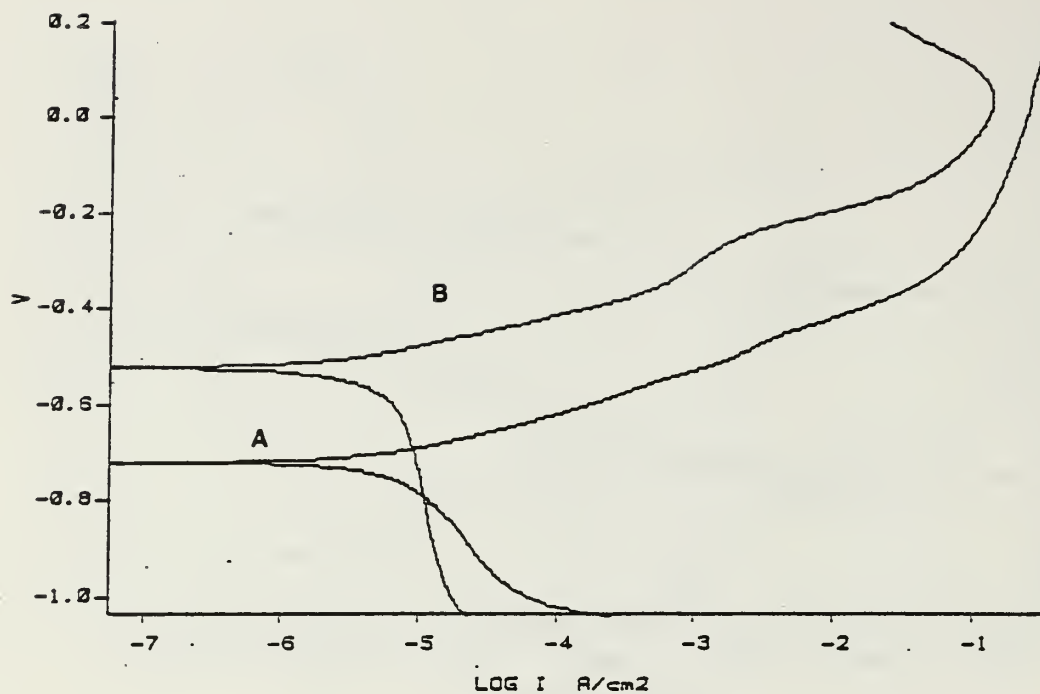


Figure 96. Overlay of Potentiodynamic Plots for 1020 C Steel (A) and Cu-Mn-Al (B)

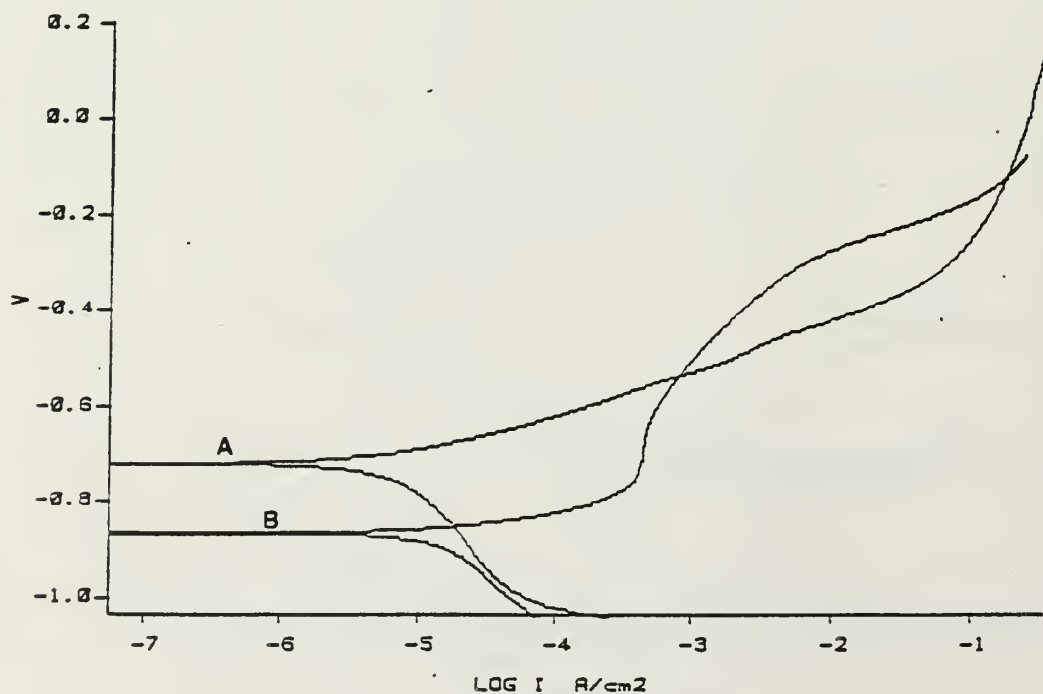


Figure 97. Overlay of Potentiodynamic Plots for 1020 C Steel (A) and Cu-Mn-Al-Fe-Ni (B)

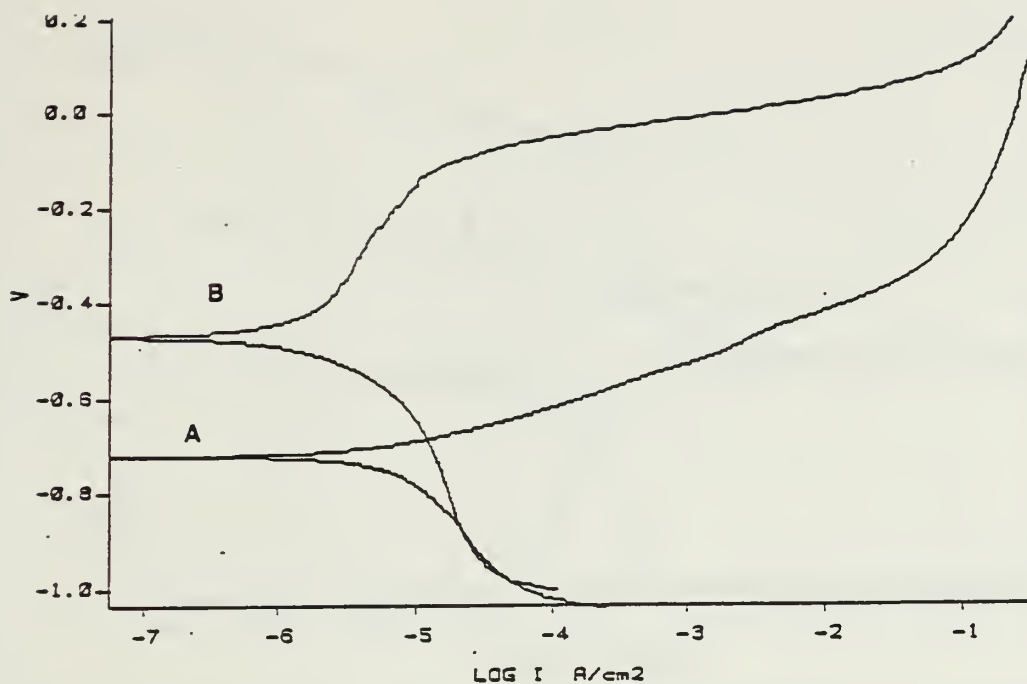


Figure 98. Overlay of Potentiodynamic Plots for 1020 C Steel (A) and Fe-Cr-Mo (B)

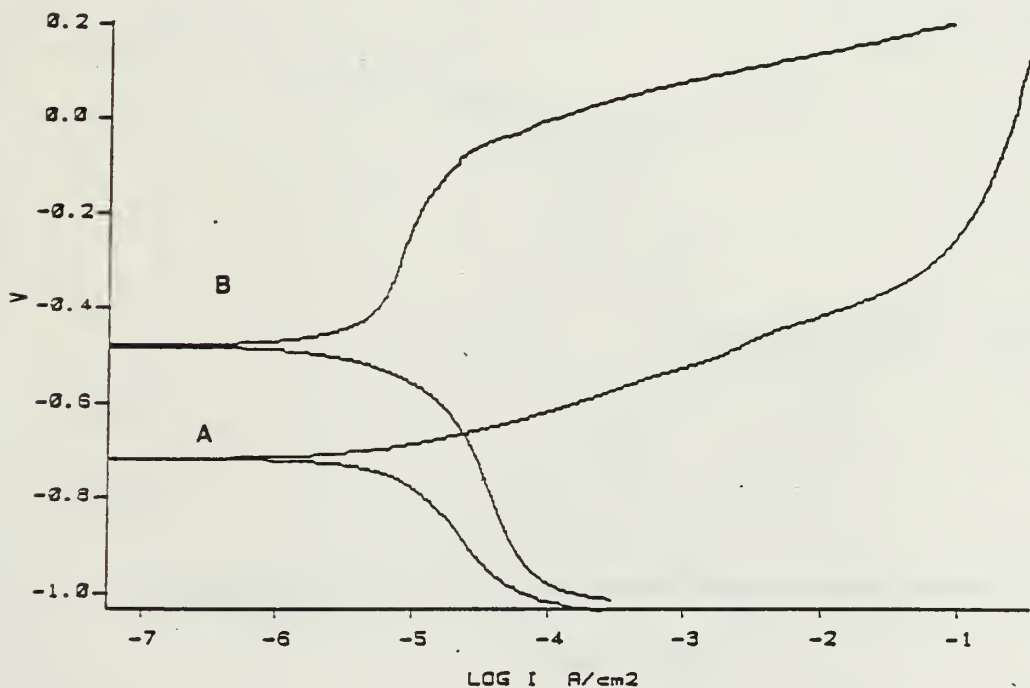


Figure 99. Overlay of Potentiodynamic Plots for 1020 C Steel (A) and Fe-Cr-Al (B)

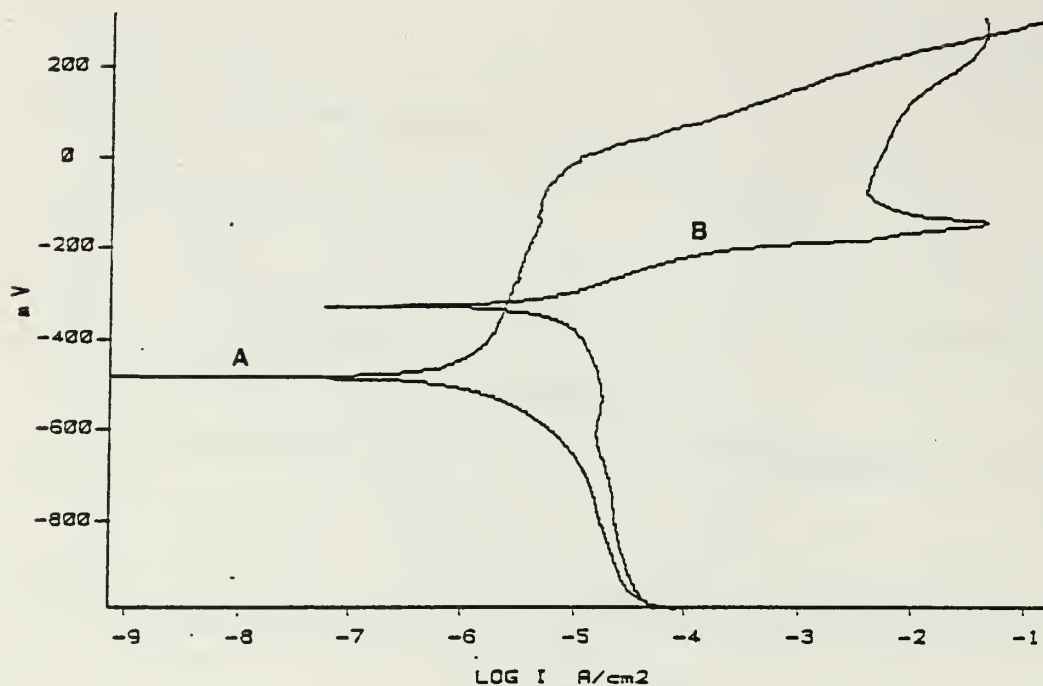


Figure 100. Overlay of Potentiodynamic Plots for 304 Stainless Steel (A) and Cu-Zn-Al (B)

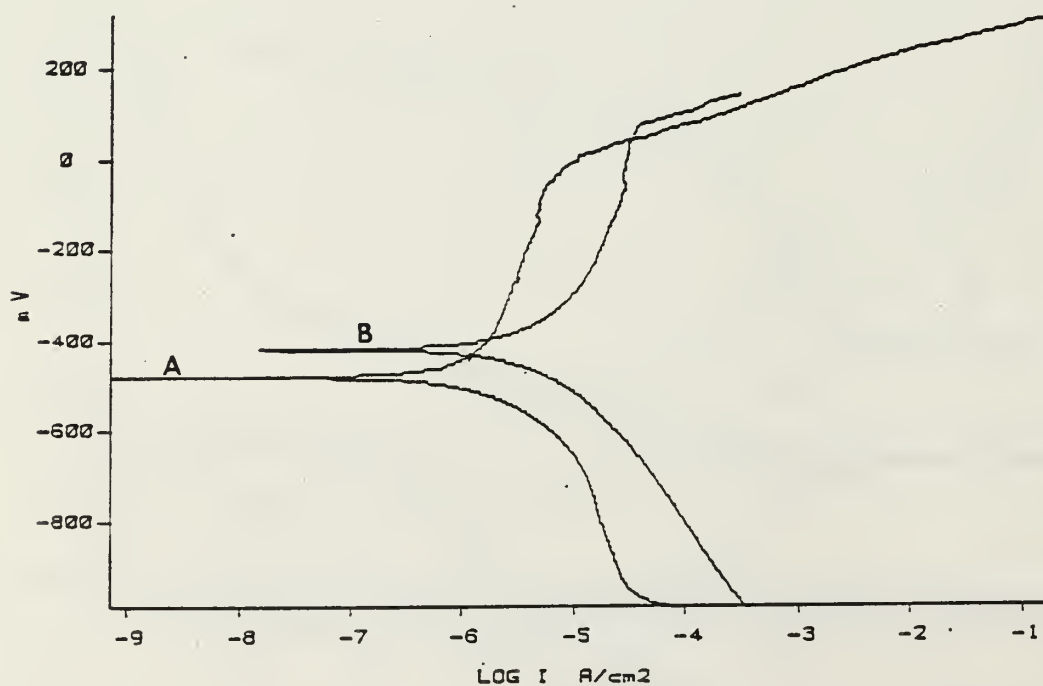


Figure 101. Overlay of Potentiodynamic Plots for 304 Stainless Steel (A) and Ti-Ni (B)

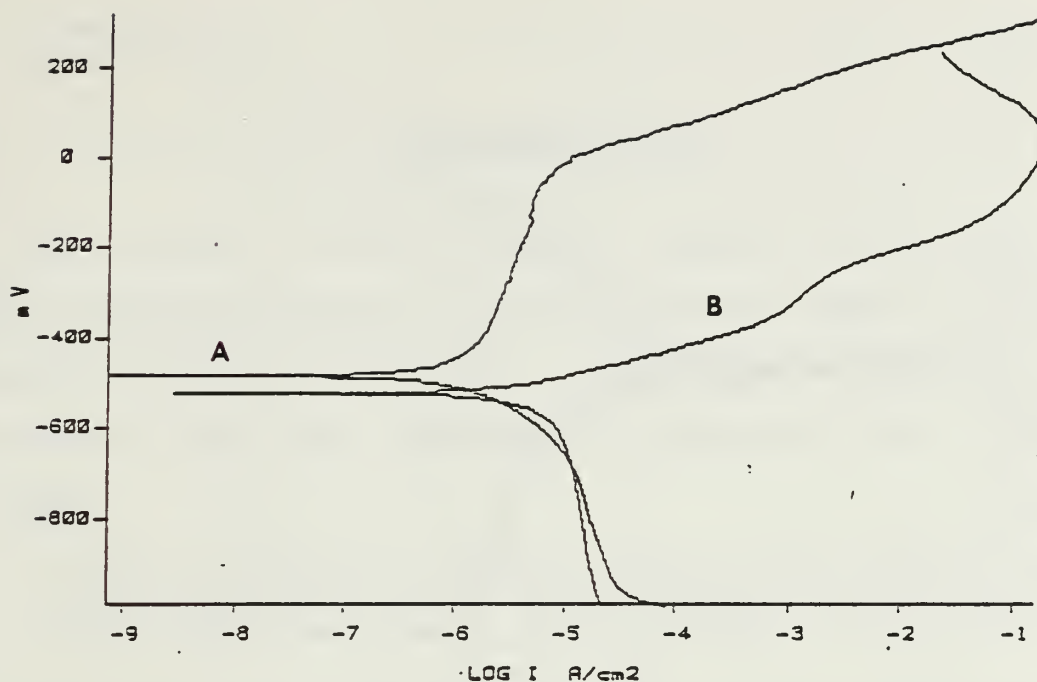


Figure 102. Overlay of Potentiodynamic Plots for 304 Stainless Steel (A) and Cu-Mn-Al (B)

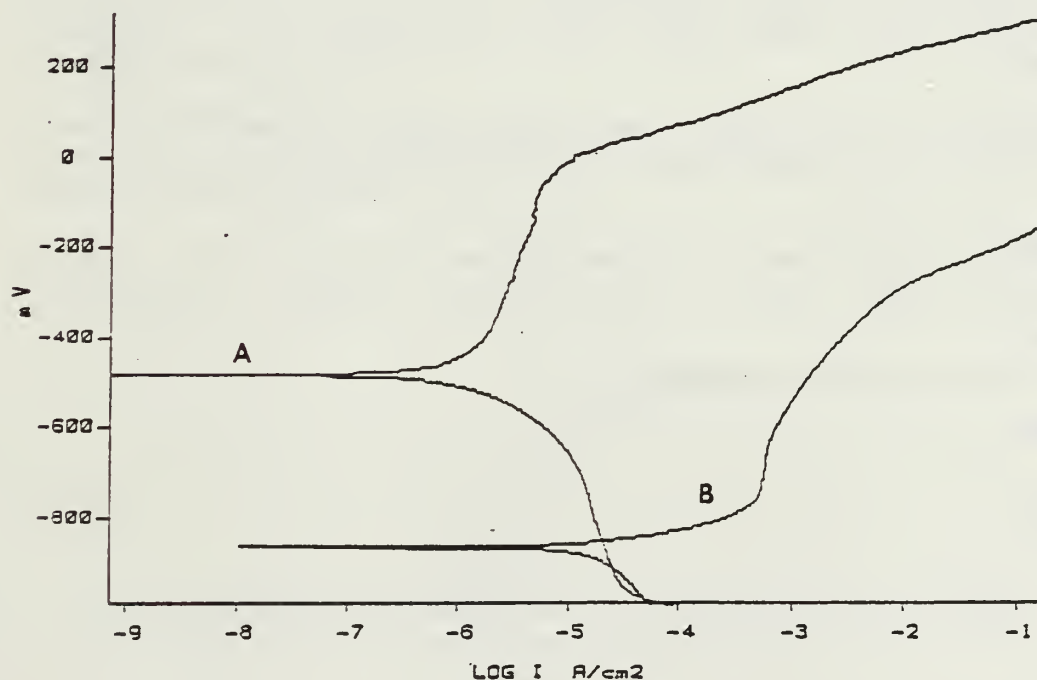


Figure 103. Overlay of Potentiodynamic Plots for 304 Stainless Steel (A) and Cu-Mn-Al-Fe-Ni (B)

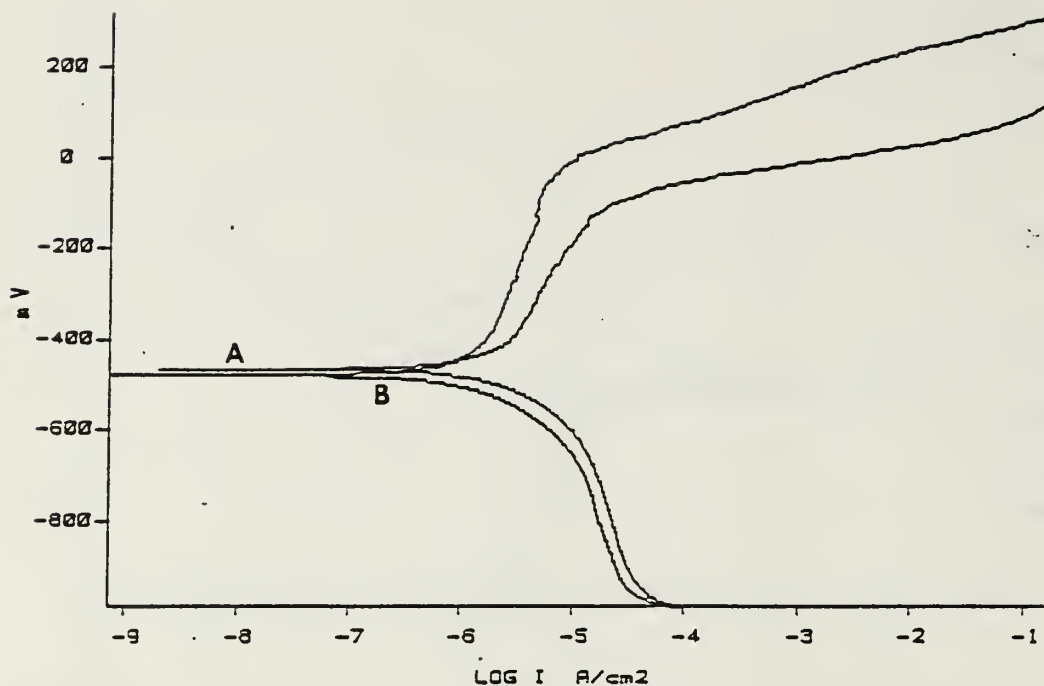


Figure 104. Overlay of Potentiodynamic Plots for 304 Stainless Steel (A) and Fe-Cr-Mo (B)

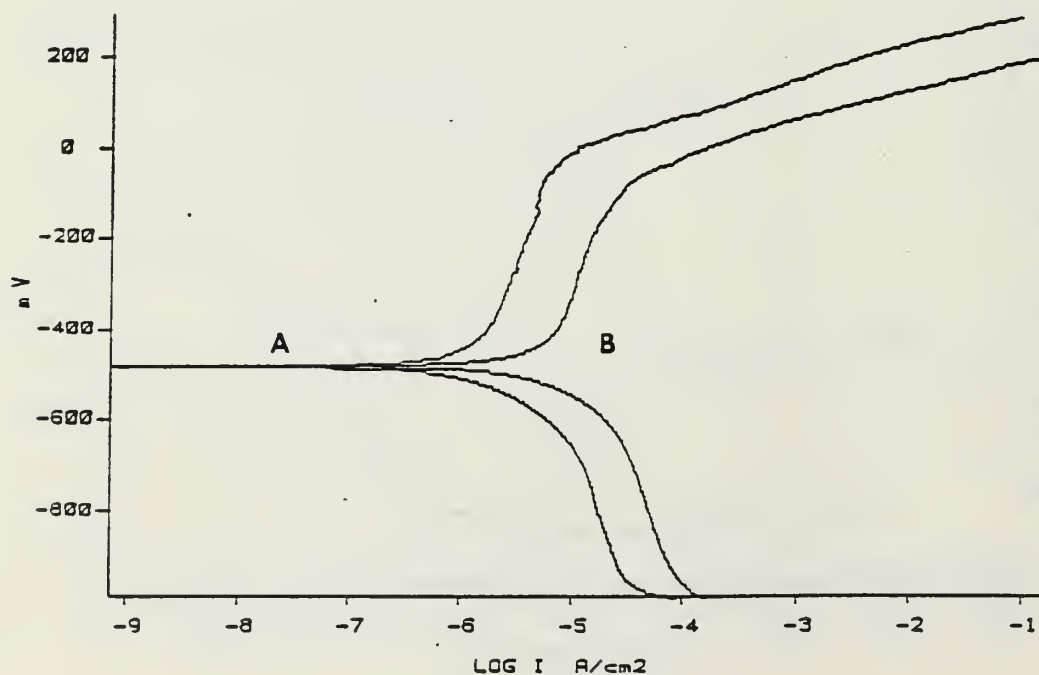


Figure 105. Overlay of Potentiodynamic Plots for 304 Stainless Steel (A) and Fe-Cr-Al (B)

V. RECOMMENDATIONS

The results of the present research constitute the initial characterization of the corrosion behavior of high damping alloys at the Naval Postgraduate School. The following items are considered appropriate for further research:

1. Continued exposure of high damping and baseline alloys the LaQue Center, with direct weight loss calculations after 150 days or more of immersion.
2. Further SEM surface analysis for alloys exposed to the natural marine environment, with particular emphasis on detailed determination of the modes of localized attack.
3. Development of a computer-assisted method for determining the Tafel constants, using a personal computer in conjunction with the Model 351 Corrosion Measurement System.
4. Verification of the predicted behavior of selected galvanic couples by testing such couples in an actual marine environment.
5. Cyclic Polarization experiments on selected alloys to determine pitting tendencies of the high damping alloys.

APPENDIX A

PREPARATION OF SYNTHETIC SEAWATER

Synthetic seawater was prepared in accordance with ASTM Standard D1141-52. Commercially available sea salt compound was used to yield the following mixture:

Constituent	g/L of Solution
Cl	19.509
Na	11.013
Mg	1.327
Ca	0.4163
K	0.3947
Sr	0.0131
B	0.0052
F	0.0013
HCO ₃	0.141
SO ₄	2.680

Natural seawater is a difficult mixture to define. Many variables affect the composition of natural seawater. Some of the more important factors are wind and wave conditions, solar radiation, rainfall in a given time period, biologics, pollutants, and geographical characteristics of a given body of water. The following is a comparison of the compositions of "typical" natural and synthetic seawater:

Ion	Natural S.W. (g/Kg)	Synthetic S.W. (g/Kg)	Pct Difference
Cl-	19.353	19.509	0.81
Na+	10.760	11.013	2.36
Mg++	1.294	1.327	2.55
Ca++	0.413	0.416	0.22
K+	0.387	0.394	0.73
HCO ₃ -	0.142	0.141	0.70
SO ₄ --	2.712	2.680	1.18

This synthetic seawater mixture represents a salinity of 35,250 parts per million dissolved solids per unit volume. Variations in open ocean salinity range from 32,000 to 37,500 parts per million. In this range, corrosion rates are not appreciably affected [Ref. 9].

APPENDIX B

STANDARD OPERATING PROCEDURES FOR THE MODEL 351 CORROSION MEASUREMENT SYSTEM

1. Prepare the specimen and the cell in accordance with ASTM Standard G 5-72 and Figure 8. Record dimensions and weight of the sample.
2. Energize the Plotter and Potentiostat.
3. Energize the Model 1000 Processor.
4. Insert the Corrosion Operating Procedure diskette to boot-up the system.
5. The program is menu driven. Enter appropriate experimental data including time, date, etc. Insert a diskette for data collection.
6. Return to the Main Menu and choose the desired experimental technique. At this stage, previously used experimental inputs or new operating parameters can be selected.
7. Once experimental parameters have been selected, assign the experiment to the corrosion cell.
8. Energize the Cell Enable switch (on the Potentiostat) and run the experiment.
9. After the data collection is complete, return to the Main Menu and store the experiment.
10. At this time, the experimental display can be plotted.
11. Following the experiment and prior to determining the corrosion rates, subtract $.2463 \text{ cm}^2$ and $.0196 \text{ cm}^3$ from the calculated surface area and volume respectively. These constants account for the loss in surface area due to the Teflon tip contact and the loss in volume due to the sample holder penetration into the specimen.
12. Corrosion rates can now be calculated from the experimental results.

LIST OF REFERENCES

1. Ailor, W.H., Handbook on Corrosion Testing and Evaluation, pp. 182-184, John Wiley and Sons, 1985.
2. Fontana, M.G., and Staehle, R.W., Advances in Corrosion Science and Technology, V. 6, pp. 185-189, Plenum Press, 1976.
3. Uhlig, H.H., and Revie, R.W., Corrosion and Corrosion Control, 3rd Ed., pp. 53-56, John Wiley and Sons, 1985.
4. Pourbaix, M., Lectures on Electrochemical Corrosion, p. 252, Plenum Press, 1973.
5. Wilde, B.E., "An Assembly for Electrochemical Corrosion Studies in Aqueous Environments," Corrosion, V. 23, pp. 331-333, November 1967.
6. National Association of Corrosion Engineers, NACE Basic Corrosion Course, p. 1-15, 1975.
7. LaQue, Francis L., Marine Corrosion Causes and Prevention, pp. 148-150, John Wiley and Sons, 1975.
8. Sedriks, A. John, Corrosion of Stainless Steels, pp. 99-108, John Wiley and Sons, 1979.
9. Schumacher, M., Editor, Seawater Corrosion Handbook, pp. 5-8, Noyes Data Corporation, 1979.

INITIAL DISTRIBUTION LIST

	No. Copies
1. Defense Technical Information Center Cameron Station Alexandria, Virginia 22304-6145	2
2. Library, Code 0142 Naval Postgraduate School Monterey, California 93943-5002	2
3. Department Chairman, Code 69Hy Department of Mechanical Engineering Naval Postgraduate School Monterey, California 93943-5000	1
4. Professor A.J. Perkins, Code 69Ps Department of Mechanical Engineering Naval Postgraduate School Monterey, California 93943-5000	8
5. LCDR William D. Escue, USN 1116 Leahy Road Monterey, California 93940	3
6. Mr. A.G.S. Morton, Code 2813 David W. Taylor Naval Ship R&D Center Annapolis, Maryland 21402	5

thesE666

Characterization of the corrosion behavi



3 2768 000 75058 2

DUDLEY KNOX LIBRARY